due
8/2 — 20-5-94pm.

4/4/95 16.55

2014-1655

SURFACE CORROSION STUDIES BY MÖSSBAUER SPECTROSCOPY

by

STEPHEN CHARLES THORPE BSc

A thesis submitted to the Council for National Academic Awards in partial fulfilment of the requirements for the Degree of Doctor of Philosophy.

Sponsoring Establishment : Department of Applied Physics and Department of Chemistry, Sheffield City Polytechnic

Collaborating Establishment : Material Quality Assurance Directorate, Ministry of Defence.

MARCH 1987

ABSTRACT

Transmission ^{57}Fe Mössbauer Spectroscopy has been used to investigate two standard iron oxides and two environmental corrosion products in the temperature range 10-300 Kelvin. This was achieved using a specially developed Air Products cryogenic refrigeration system using gaseous helium as the refrigerant - thereby removing the requirement of an expensive liquid helium facility normally required for low temperature work.

Characteristic spectra and transitions were observed for both the standard oxides. The environmental corrosion products demonstrated the differences in observed spectra between a sample which exhibits only bulk properties and one in which the particle size distribution within the sample is such that relaxation phenomena become important. The interpretations made from the variable temperature Mössbauer data were confirmed by the complementary technique of X-ray diffraction.

Conversion electron Mössbauer spectroscopy (C.E.M.S.) and conversion X-ray Mössbauer spectroscopy (C.X.M.S.) backscatter techniques have also been developed and are now routinely available in our laboratory.

The greater escape depth of the conversion X-ray allows the C.X.M.S. method to be used to record spectra from samples to which a protective layer such as a paint, varnish, grease or oil layer has been applied. To ensure a surface sensitive signal, the substrate surfaces had to be enriched in the Mössbauer isotope ^{57}Fe. This was achieved by vacuum evaporation of ^{57}Fe onto the substrate surface and subsequent diffusion of the ^{57}Fe into the near surface region - this diffusion had to be accomplished without oxidising the surface.

Samples thus prepared were subsequently exposed to aggressive atmospheres and their CXM spectra recorded. The limitation of the method is that only room temperature spectra can be recorded at present and difficulties are encountered in the assignment of spectra that contain only quadrupole doublets.

CONTENTS Page

CHAPTER 1 : LITERATURE REVIEW

1.1 Mössbauer Spectroscopy of Iron Oxides and Oxyhydroxides 1

1.2 Mössbauer Spectroscopy - A Tool for Corrosion Research 12

References 33

CHAPTER 2 : THE MÖSSBAUER EFFECT, HYPERFINE INTERACTIONS AND RELAXATION PHENOMENA

2.1 Recoilless Nuclear Resonance Absorption 43

2.2 Hyperfine Interactions 55

2.3 Particle Size Effects 73

References 80

CHAPTER 3 : EXPERIMENTAL TECHNIQUES

3.1 Characteristics of a Useful Mössbauer Isotope 82

3.2 The Mössbauer Source 84

Page

3.3 The Absorbers 86

3.4 Detectors 88

3.5 Instrumentation 93

3.6 Variable Temperature Facilities 97

3.7 Computer Fitting of Mössbauer Spectra 104

References 112

CHAPTER 4 : VARIABLE TEMPERATURE MÖSSBAUER SPECTROSCOPY

4.1 Vibration Isolation from the Displex Cryostat 114

4.2 Standard Oxide, Haematite, α-Fe_2O_3 116

4.3 Standard Oxide, Magnetite, Fe_3O_4 119

4.4 Environmental Corrosion Product 121

4.5 Aqueous Corrosion Product 128

4.6 Spectra 137

References 161

Appendix 164

Page

CHAPTER 5 : SURFACE CORROSION STUDIES

5.1 Conversion X-ray Mössbauer Spectroscopy 165

5.2 Surface Enrichment 166

5.3 Diffusion of ^{57}Fe 168

5.4 Laboratory Corrosion Tests 180

5.5 Surface Monitoring of some Mild Steel Substrates 184

5.6 Spectra 192

References

CHAPTER 6 : CONCLUSIONS AND SUGGESTIONS FOR FUTURE WORK

6.1 Conclusions 201

6.2 Future Work 203

ACKNOWLEDGEMENTS

COURSES AND CONFERENCES ATTENDED

CHAPTER 1 : LITERATURE REVIEW

1.1 Mössbauer Spectroscopy of Iron Oxides and Oxyhydroxides

1.2 Mössbauer Spectroscopy : A Tool for Corrosion Research

References

CHAPTER 1 : LITERATURE REVIEW

1.1 Mössbauer Spectroscopy of Iron Oxides and Oxyhydroxides

1.1.1 Haematite and Maghemite, Fe_2O_3

The most common iron oxide is the α phase of Fe_2O_3, haematite, and Kistner and Sunyar [1] first measured an isomer shift and quadrupole interaction from the spectrum of this compound. A detailed study of powder samples of α-Fe_2O_2 was made by Van der Woude [2]. The Néel point, T_N, was determined as 956 K, above which haematite is paramagnetic. Below the Néel temperature two antiferromagnetic regions exist. Above the Morin temperature, T_M = 260 K, the Mössbauer spectrum have ε negative. In the region of the Morin temperature, there is a 90° spin flip so that below T_M the spins are aligned along the V_{zz} axis and ε is positive.

The sign of the quadrupole interaction apparently changes in a continuous process between 200 and 280 K, reaching zero at 260 K, the Morin temperature [3].

Kundig et al [4,5] studied both bulk powders and small size ($\sim$ 10 nm diameter) haematite particles supported on a high surface area silica gel. The smallest particles showed no Morin transition with negative ε persisting to low temperatures. In addition, the small particles showed superparamagnetic (spm) behaviour with doublet spectra observed well below the Néel point. The superparamagnetic splitting increased with decreasing particle size. The decrease of the Morin transition with particle size was

also observed by Yamamoto [6]. In this case, different methods of preparation gave different size dependence with the range of sizes at which T_M approach zero varying between 20-60 nm diameter unsupported particles. Krupyanskii and Suzdalev [7] compared results from 15 nm diameter particles supported on silica gel. These had a lower value of T_M (215 K) than did the corresponding bulk sample and the conclusion was that the nature of the support affected the magnetic properties. Nininger and Schroeer [8] observed a Morin temperature of 175 K for 35 nm diameter particles. It was estimated that particles smaller than 20 nm diameter would not have a Morin transition, in agreement with the predictions of Kundig et al [4] and with Yamamoto [6].

Syzdalev [9] explained the collapse of the six line spectrum to a doublet for both α-Fe_2O_3 and α-FeOOH fine particles as a phase transition between antiferromagnetic ordering and the paramagnetic state at a certain critical volume. Van der Kraan [10] observed considerable line broadening in the spectra of fine particles of α-Fe_2O_3, and studied surface effects by enriching the surface of small particles with ^{57}Fe. For 12 nm diameter particles, the Morin transition was not observed even down to 4 K. Unenriched very small particles (5 nm diameter) exhibited what appeared to be two fields at low temperature, and the paramagnetic doublet had larger splitting ($\Delta \cong 0.9$ mms^{-1}) than the bulk material.

Shinjo et al [11] prepared α-Fe_2O_3 particles from pure ^{56}Fe, the surface of the particles being very thinly coated with ^{57}Fe. Spherical particles of α-Fe_2O_3 of 100-200 nm were produced. The Mössbauer results showed that the surface hyperfine field rapidly decreased with increasing temperature but the Morin transition took place at the same temperature as for bulk crystals.

The spinel γ-Fe_2O_3 (maghemite), is ferrimagnetic with octahedral and tetrahedral iron sites. Armstrong et al [12] used an external field to resolve the two sites, and concluded that vacancies existed in octahedral sites only. Coey and Khalafalla [13] studied superparamagnetism in small particles of γ-Fe_2O_3. Spectra at low temperatures and in applied fields showed no distinct difference between fields in bulk and fine particles except for a random spin canting angle for surface ferric ions and for the relaxation effects due to superparamagnetism. Haneda and Morrish [14,15] studied vacancy ordering in small particles of γ-Fe_2O_3 and used surface enriched ^{57}Fe to conclude that the variation of the hyperfine field with particle size was due to the particle size distribution rather than a different field for surface atoms. Maghemite has been found environmentally [16] and its magnetic properties find application in recording tape [17].

1.1.2 Magnetite, Fe_3O_4

Magnetite, Fe_3O_4, is an inverse spinel in which the iron atoms occupy interstitial sites between oxygen atoms which have a close-packed cubic structure. There are two types of iron sites, the tetrahedral (A) sites and the octahedral (B) sites, of which the former are occupied by Fe^{3+} ions and the latter by Fe^{2+} and Fe^{3+} ions. In the unit cell there are twice as many B sites as A sites. In a simple ionic model, the iron atoms at the B sites are antiferromagnetically coupled to those at the A sites so that the moment of the ferric ions cancel and the net ferromagnetic moment is due to the ferrous ions at the B sites, with the easy direction of magnetisation being normally along the [111] direction. On cooling to 119 K, the Verwey temperature, T_V, [18], the structure spontaneously transforms to orthorhombic symmetry and the electrical resistivity increases by two orders of magnitude. Verwey et al [19,20] explained the low resistivity above T_V as being due to rapid electron hopping between Fe^{2+} and Fe^{3+} ions at the octahedral sites. Such hopping is inhibited below T_V due to an ordering of the Fe^{2+} ions in alternate layers, which gives rise to the orthorhombic symmetry [21].

The interpretation of Mössbauer spectra above T_V has added weight to an alternative explanation of the increased conductivity in terms of a band model for the electrons. Below T_V, both Mössbauer spectroscopy and nuclear magnetic resonance techniques suggest that the

magnetic ordering is not as simple as originally envisaged by Verwey et al [19,20].

The Mössbauer spectrum for magnetite at room temperature consists of two sets of six line patterns with fields of 488 and 460 kG in the area ratio 1:2, associated with the A and B sites. The widths of the B site lines are typically 50% broader than those of the A site lines. This broadening was formerly associated with a relaxation mechanism involving electron hopping between the Fe^{2+} and Fe^{3+} sites. A value for the relaxation time at 295 K of 1.1 ns was obtained from the temperature variation of the B site line width [22], but this would imply a conductivity two orders of magnitude smaller than the measured one. Later work [23-25] has shown that relaxation effects are not responsible for the broadening. This was first clearly demonstrated by van Diepen [23,24] who showed that the B site line-width for a single crystal of magnetite depended upon the direction of application of a small applied magnetic field (8 kG). This showed that the broadening was due to the presence of several fields at the B sites rather than relaxation broadening. The variation of these field values with orientation of the iron spins strongly suggested that the changes were due to changes in the dipolar contributions to the hyperfine field.

Below the Verwey transition, the simple ordering model in which the ferrous and ferric B site ions are arranged on alternate [100] planes implies the presence

of two hyperfine fields at these sites. The Mössbauer spectrum is more complex, however, and Hargrove and Kündig [26] and Rubinstein and Forester [27] have fitted the B site spectrum with four and five fields respectively. Rubinstein and Forester [27] also measured the NMR spectra at 4.2 K for the same sample which showed four resonances for the A site and five resonances for the B site. Each of these resonances could be decomposed into several components and the result was consistent with eight inequivalent Fe_3O_4 molecular units in the unit cell below T_V which gives rise to eight inequivalent A sites and 16 inequivalent B sites. Mørup et al [28,29] have investigated the particle size dependence of magnetite spectra, studying 6 nm and 10 nm particles over a wide temperature range. The spectra of the 6 nm particles collapse to a broad singlet at $\sim$ 230 K whereas the 10 nm particles show magnetic splitting up to at least 350 K. 6 nm particles of Fe_3O_4 show the presence of a Verwey transition between 4.2 K and 80 K. The Verwey transition temperature decreases with decreasing particle size but appears to be less sensitive to particle size than the Morin transition in α-Fe_2O_3 [29].

1.1.3 The Iron Oxyhydroxides, x-FeOOH

Takada et al [30] published some of the first data on three crystalline forms of iron(III) oxyhydroxide, FeOOH. They identified α-, β-, and γ phases. Rossiter and Hodgson [31] recorded the Mössbauer spectra of these and

an additional crystalline form, δ-FeOOH, at room and liquid nitrogen temperatures.

α-FeOOH, goethite, has the same structure as α-AlOOH with the iron in a distorted octahedral environment of oxygen, and a three dimensional structure results from the sharing of edges and corners of the octahedra. Akaganite, β-FeOOH, differs in that it is non-stoichiometric containing various quantities of fluoride or chloride ions and water depending on the conditions under which it is prepared. It has the α-MnO_2 structure with a three dimensional oxygen lattice and an octahedral iron environment. Lepidocrotite, γ-FeOOH, is similar to α-FeOOH but has a complex layer structure. The fourth form, δ-FeOOH, is ferrimagnetic in contrast to the α-, β-, and γ-forms for which the low susceptibilities imply paramagnetism or antiferromagnetism. Little is known about its crystal structure other than it appears to be based on a hexagonally close-packed oxygen (hydroxyl) lattice.

Early work on α-FeOOH reported a magnetic hyperfine splitting at room temperature, showing it to be antiferromagnetic [30,31]. Other data showed evidence for two hyperfine patterns which, it was claimed, had a different temperature dependence, ordering at 340 K and 370 K respectively [32,33]. This imples four magnetic sublattices to preserve antiferromagnetism. Two reports of superparamagnetism in small particle goethite further

confused the picture [34,35], the broadening of the peaks resembling twin magnetic field data. Better quality data over the range 90-440 K showed only one hyperfine field below the Néel temperature of 393 K with a zero temperature extrapolated value of 510 kG for the hyperfine field [36].

These inconsistencies were explained by Dezsi and Fodor [37] who found that three out of five deposits of natural α-FeOOH, and also a synthetic sample, gave a unique hyperfine pattern, while the other two did show clear evidence of two fields. The latter result was found to be true of samples containing excess water; stoichiometric α-FeOOH does not show evidence for more than two magnetic sublattices. The Néel temperature was found to be only 367 K, and relaxation occurred at up to 30° below this. The defect structure and particle size are both important in determining the properties of a specific sample.

A definitive study of the magnetic structure using powdered synthetic α-FeOOH and a natural single crystal has been made by Mössbauer spectroscopic and neutron diffraction methods [38]. The spins are all parallel to the 'c' axis of the crystal (also shown by partial orientation of powder samples [39]) with the major axis of the electric field tensor in the 'ab' plane, making an angle of about 40° with the 'b' axis. The Mössbauer data give a Néel temperature of 403 K. Neutron diffraction data indicate both ferromagnetic and antiferromagnetic

coupling between iron atoms. The Néel temperature will correspond to the point at which the weaker of these breaks down. The extrapolated magnetic field value of H(O) = 504 kG is smaller than that of Fe_2O_3 (544 kO_e) or FeF_3 (622 kG) and reflects the effect on the Fermi term of increased covalency in this compound. In this sense, the magnetic field of ferric ions is a better indication of the degree of covalency than the chemical isomer shift.

Govaert et al [40,41,42] in a series of short papers have summarised the variety of natural goethites which give room temperature spectra varying from sharp six line, to broadened highly relaxed, to mostly para-magnetic doublets. The minerals are classified [40] in three classes: (i) Goethites of hydrothermal origin with large grain size and clear six line spectra. These materials also had narrow X-ray peaks and no excess water. (ii) Goethites with asymmetrically broadened Mössbauer spectra. These were formed by weathering of oxides sulphides or silicates. These samples contained about 13% excess water. (iii) Goethites formed by weathering of $FeCO_3$ producing very small particles and containing much excess water. The Mössbauer spectra were primarily doublet in nature.

The crystalline modification akaganeite, β-FeOOH, was investigaged by Takada et al [30]; it was shown that this phase had zero field at room temperature and a

hyperfine field smaller than that of goethite at 100 K. Dezsi et al [43] studied the spectra of β-FeOOH as a function of temperature. The Néel point was observed at approximately 295 K and above this the material remains paramagnetic until at about 670 K decomposition occurred to α-Fe_2O_3. Yamamoto et al [39] used oriented particles to determine that the spins were parallel to the long c axis and the field gradient perpendicular to the c axis. Another study of β-FeOOH has been made by Howe and Gallagher [44] who noted that some previous reports had been of unwashed, undried material, which probably contained some chloride ions. The stoichiometry of the reported material was not FeOOH but given as $FeO_{0.91}(OH)_{1.18}$. Hogg et al [45] studied the temperature dependence of the magnetic field for a synthetic sample of β-FeOOH and fitted the data to a Brillouin curve to obtain a Néel temperature of 296 K. Two reports have appeared dealing with naturally occurring akaganeite in soil. Logan et al [46] based their evidence on room temperature doublet spectra which have quadrupole splittings greater than the other forms of FeOOH. Johnston [47] found characteristic X-ray patterns for β-FeOOH in volcanic surface deposits as well as room temperature Mössbauer parameters similar to the above. He noted the presence of $\sim$ 10% chloride ion in the natural akageneite samples. He also noted that the spectrum of synthetic β-FeOOH, which gave an average Δ = 0.70 mms^{-1} at room temperature, could be

split into two doublets: one with $\Delta = 0.96$ mms^{-1} and the other 0.54 mms^{-1}. This latter splitting was in lower abundance and was ascribed to fine particles of goethite present in the seemingly pure material. In a series of more recent papers, Chambaere and De Grave [48,49,50,51, 52] have studied several aspects of β-FeOOH, and have shown that the value of T_N and the magnetic interactions are variable and depend upon conditions during synthesis. It is suggested that this is due to a spin reduction induced by a variable amount of interstitial water molecules in the compound. The low temperature antiferromagnetic state has also been characterised and three separate hyperfine fields have been identified. The phase transformation β-FeOOH to α-Fe_2O_3 has also been studied.

Lepidocrocite, γ-FeOOH, is paramagnetic down to at least 77 K with a small quadrupole splitting [30,31,33,53]. Below this temperature it becomes antiferromagnetic [53]. The Néel temperature is not clearly defined in either mineral or synthetic samples, and magnetic and paramagnetic spectra coexist over a range of at least 10 K even in large single crystals. This excludes small particle superparamagnetism as an explanation. Murad and Schwertmann [54] studied the influence of crystallinity on the Mössbauer spectrum of lepidocrocite, noting a decrease in the quadrupole splitting of poorly crystallised paramagnetic samples and lowering of the onset of magnetic ordering from the bulk Néel temperature

to about 50 K. At 4.2 K, distributions of magnetic hyperfine fields with a limiting upper field of 460 kG were observed. The contributions of lower fields to such distributions increase with decreasing crystallinity, producing asymmetrically broadened lines.

δ-FeOOH is ferrimagnetic [55]. It decomposes to intermediate products at 370 K, below its Curie temperature, and disintegrates to α-Fe_2O_3 at approximately 510 K. Early workers assigned the two internal fields of 525 and 505 kO_e at 80 K to ferric ions in octahedral and tetrahedral sites, respectively [43]. Okamoto [56] suggested a distribution of ferric ions in two octahedral sites which better described the magnetic features of the oxyhydroxide. The magnetic properties of δ-FeOOH are shown to be dependent on particle size and this in turn on the preparation conditions [57].

1.2 Mössbauer Spectroscopy, a Tool for Corrosion Research

In recent years, Mössbauer spectroscopy has become a very important tool in corrosion research. Advantages of the method include: (i) it is non-destructive, (ii) it can be applied for qualitative and quantitative phase analysis, (iii) surface layers of different thickness can be investigated, (iv) corrosion beneath overlayers can be observed, (v) it is a relatively inexpensive method. The initial steps of the corrosion process, which involve only one or two monolayers at the metal surface, are not observed using the Mössbauer

technique unless sophisticated surface techniques with enriched ^{57}Fe are used. All subsequent steps can be investigated by Mössbauer spectroscopy ie the thickness range 3-300 nm by conversion electron Mössbauer spectra and up to 100 μm by gamma scattering or transmission Mössbauer spectroscopy. This region is of great interest in the investigation of the corrosion process and is not easily monitored by methods such as photo-electron spectroscopy or X-ray diffraction. Typical results of phase analyses by X-ray diffraction and Mössbauer spectroscopy are compared by Meisel [58]. Loose rust from a steel sample formed after outdoor exposure for several months in an industrial region was used. A substantial amount of the corrosion product is amorphous with respect to X-rays and therefore cannot be identified by X-ray methods. The Mössbauer results indicate that this component consists mainly of α-FeOOH. The reportedly small Fe_3O_4 content found by X-ray diffraction is a misinterpretation because the spinel oxides Fe_3O_4 and γ-Fe_2O_3 are not distinguishable by their X-ray spectra. The Mössbauer spectra of the two spinels are very different.

The effect of sea water and other waters (distilled, bidistilled, mineral and drinking water) on α-Fe has been studied by Péev et al [59]. The major corrosion products in the case of sea water are β-, γ-FeOOH, and FeOCl. The same author [60] has also investigated the corrosion of iron in the anion exchanger of an industrial

water desalinising equipment. Goethite and magnetite were identified as the major corrosion products.
Bhat and co-workers [61,62] have studied the corrosion products of a cast iron and an electrolytic iron in aqueous ammonium nitrate solution. The initial products of room temperature corrosion of the cast iron were found to be a ferrihydrite $Fe_5HO_8.4H_2O$ and γ-FeOOH, but after longer periods magnetite was observed. Above 80°C, non-stoichiometric magnetite or ferrihydrite or haematite are the major products depending on the ratio of the reactants. The nature of the corrosion products on the electrolytic iron were shown to be pH dependent at room temperature. At temperatures above 80°C α-Fe_2O_3 was the major product. Leidheiser et al [63,64] have investigated the atmospheric corrosion of iron. The initial product of γ-FeOOH changes to a mixture of α-FeOOH and γ-Fe_2O_3. Steels exposed for many years were observed to be covered with a corrosion product consisting largely of γ-Fe_2O_3, the minor component being γ-FeOOH. Mössbauer spectroscopy has been used to study the corrosion products of mild steel exposed to several different environments [65] including outdoor natural and marine atmospheric, sulphur dioxide, sulphur dioxide plus hydrochloric acid, and synthetic sea waters. In most cases, large portions of γ-FeOOH and super-paramagnetic fractions of α-FeOOH were identified. Corrosion products from mild steel panels exposed at eight different atmospheric test sites in Sweden were

studied by Singh et al [66]. All samples exhibited small particle superparamagnetic relaxation effects in the room temperature Mössbauer spectra. The corrosion products were mainly identified by low temperature (10 K) Mössbauer spectra and X-ray diffraction - the diffraction lines are broad confirming the small particle size. In all samples, α-FeOOH and γ-FeOOH were the main constituents (> 70%). β-FeOOH and non-stoichiometric magnetite were found in samples exposed to marine atmospheres. The α-FeOOH/ γ-FeOOH ratio was found to increase with increasing sulphur dioxide concentration at the various test sites.

1.2.1 Backscatter Mössbauer Techniques

The majority of Mössbauer experiments are performed in a transmission geometry and involve the detection of gamma radiation transmitted through thin absorbers, this method yielding data relating to the bulk properties of the absorber. If information relating to surfaces is required, the use of transmission methods is restricted to a few special absorbers. These may be microcrystalline dispersed on high area inert substrates, materials with high internal surface areas such as zeolites or clay minerals, or simply stacks of very thin absorbers. To overcome these difficulties and to study surface and near surface regions of solids, backscatter techniques based on the detection of conversion electrons and conversion X-rays emitted from the surface following the resonant absorption step in the absorber have been developed [67]. An excited ^{57}Fe nucleus, $*^{57}Fe$, will

decay in approximately 80% of cases by the emission of a 7.3 keV conversion electron. The escape depth for such an electron is typically about 300 nm so that the Mössbauer spectrum obtained by detecting such electrons will be characteristic of iron atoms within that depth in the scatterer. Following the emission of these conversion electrons in about 70% of cases an L Auger electron is emitted which will also contribute to the Mössbauer emission signal. In the remaining 30% of cases, a 6.3 keV X-ray is emitted which has a typical escape depth of about 10 μm [68]. Several proportional counter designs have been described which may be used to count either electrons or X-rays by changes in the flow gas mixture from helium/methane to argon/methane [69,70]. Clearly, conversion electron Mössbauer spectroscopy (CEMS) will be of most value in the study of thin surface layers such as those produced by oxidation or corrosion or by deliberate chemical treatment of a surface. If the surface treatment is somewhat deeper, the use of conversion X-ray Mössbauer spectroscopy (CXMS) is required. This technique may also be used to record spectra from substrates protected by oil, paint or varnish layers without first removing such a layer from the surface [71].

There have been many CEM studies of oxidised iron foils ranging from simple demonstrations of oxide-oxyhydroxide components in the spectra to systematic attmepts to determine the oxide thickness as a function of oxidising

temperature, time, and oxygen pressure. The problem of determining the oxide thickness from the relative spectral areas due to oxide and substrate is complex because of uncertainties in the values of electron attenuation coefficients.

In one of the earliest systematic investigations, Simmons et al [72] identified the oxides present when high purity iron wafers, on which had been electro-deposited about 500 nm of ^{57}Fe, were oxidised in either oxygen or dry air at 1 atm pressure at temperatures of either 225, 350 or 450°C. After oxidation at 225°C for longer than 5 minutes, a component due to nonstoichiometric magnetite was observed, while at 350°C (5 minutes) a duplex layer of α-Fe_2O_3 and Fe_3O_4 was formed. After oxidation for 10 minutes at 450°C, the oxide was mainly stoichiometric magnetite. The oxidation rate is thought to be dependent upon the ion and electron conductivities through the oxide, and the absence of α-Fe_2O_3 at the highest temperature was attributed to the resulting higher cation flux. Nucleation of α-Fe_2O_3 is not favoured until a sufficient thickness of Fe_3O_4 is produced to reduce the cation flux.

The absence of α-Fe_2O_3 was also noted by Sette, Camara, and Keune [73] who oxidised a sample of unenriched carbon steel (0.31% Mn, 0.04% C) for 30 minutes at 490°C and a partial pressure of 10 Torr O_2. However, oxidation of a pure iron sample at 500°C for a few minutes

at 10 Torr O_2 produced comparable amounts of Fe_3O_4 and α-Fe_2O_3. These authors noted that the relative intensities of the lines in the haematite spectrum were 3:3.1:1.2:1.2:3.1:3. This suggested that the haematite grew with its c axis preferentially oriented perpendicular to the oxide-metal interface. Using a relationship between relative spectral area and oxide thickness derived from Swanson and Spijkermann [69], it was shown that the total oxide thickness for iron samples oxidised at 500°C was approximately proportional to the square root of the oxidation time. If the oxide thickness can be determined independently, for example, from the measured oxygen uptake, than a relationship between this thickness and relative spectral area due to the oxide may be established. Graham and co-workers [74] achieved this by investigating magnetite films in the range 26-450 nm grown on natural iron substrates. In a different study, Berry [75,76,77] investigated the phosphating process used to prevent atmospheric attack on iron foils. Several "light" and "heavy" phosphate coatings were characterised and their stability against oxidation and hydration investigated.

1.2.2 Aqueous Corrosion Studies

Ensling and co-workers [78] have studied the formation of protective oxide coatings on steam generator tubes in the presence of water at high temperatures and pressures. In the case of the alloys with a low nickel concentration, the only oxide phase detected in the CEM spectra besides

the substrate phases was a non-stoichiometric magnetite. The composition of the protective magnetite layers varied slightly with increasing oxidation time. In contrast, a nickel ferrite, $Ni_{0.8}Fe_{2.2}O_4$, was formed as a protective layer on the nickel rich alloy; its composition being nearly independent of the oxide layer thickness. The aqueous corrosion of iron may lead to a variety of products that include β-FeOOH, γ-FeOOH, α-FeOOH, γ-Fe_2O_3, α-Fe_2O_3 and Fe_3O_4. If only room temperature CEM spectra are recorded, difficulties may be encountered in the assignment of spectra that contain only quadrupole doublets since these may arise from either β- or γ-FeOOH or even superparamagnetic particles of either α-FeOOH, γ-Fe_2O_3, α-Fe_2O_3 or Fe_3O_4. However, by making a variable temperature study, the occurrence of superparamagnetic behaviour or the onset of magnetic ordering may be detected, thus providing a further insight into the nature and composition of the corrosion product. The nature of corrosion and abrasion resistant surface phases formed by the chemical treatment of an iron containing solid has been investigated by Berry et al [79]. Conversion electron and transmission Mössbauer techniques were used. Corrosion resistant films produced by oxidising alkaline solutions were shown to contain ferric oxyhydroxides. Nitriding processes which harden the surface by reaction of the metal with cyanide ions give superficial phases which include two iron nitrides, Fe_2N and Fe_4N. Sulphiding processes

produce abrasion resistant surfaces by reaction of the metal with thiocyanate ions and give a surface phase containing the iron sulphide "Gregite" Fe_3S_4. No evidence was found for the presence of iron carbides in materials treated with cyanate or thiocyanate. Nitrided steel surfaces were also investigated by Inaba et al [80]. The CEM spectrum obtained at room temperature indicated that two phases of iron nitrides existed at the surface and the nitrogen content was shown to decrease gradually as successive layers were removed. CEM spectra were recorded at 507 K, 363 K and room temperature.

Huffman and Podgurski [81] used the CEM technique to determine the thickness of haematite and magnetite layers on iron foils oxidised in pure oxygen at elevated temperatures. The oxide thickness values were found to be in good agreement with the volumetrically measured oxygen uptake. Electron attenuation coefficients determined from experimental work by Graham, Mitchell and Channing were used [82].

Meisel and co-workers [83] used the CEM technique to study the oxide layer formed on a steel substrate in water containing chromate and chloride ions. CEM spectra were recorded at room temperature using a helium methane flow counter. For low temperature measurements, the sample was mounted in a helium cryostat and the electrons were detected using a channeltron [84]. X-ray photo-

electron spectroscopy (ESCA) was used as a complementary technique. In the presence of chloride ions, the oxide layers formed were found to be thicker by an order of magnitude than those formed in the absence of chloride ions. These oxide layers were thought to consist of ferric and chromic oxides of the corundum type $(Fe_{1-x}Cr_x)_2O_3$ with the Cr:Fe ratio being depth dependent. Passive films formed in pure chromate solutions are known to exhibit a spinel type structure. In a subsequent paper the same group reported the influence of phosphoric acid on a standard steel and on its corrosion products [85]. Many industrial steel coatings require a pretreatment of the surface with phosphoric acid and, although any treatment is preceded by a rigorous cleaning of the surface, residual (or subsequently formed) oxides and corrosion products can never be completely excluded. Reactions of phosphoric acid with these oxides and corrosion products as well as the metal surface must therefore also be considered. Most commercial "rust transformers" consist mainly of concentrated phosphoric acid. A previous Mössbauer spectroscopy study showed that they fail to form a protective oxide layer on the steel surface [86]. This work showed that two types of process have to be considered: (i) the influence of concentrated phosphoric acid on metallic iron, Fe_3O_4 and FeO, results in the formation of a mixture of $FePO_4.4H_2O$ and $Fe_3(PO_4)_2.8H_2O$. (ii) The influence of concentrated phosphoric acid on

α-, γ-Fe_2O_3, α-, β- or γ-FeOOH results in the acid ferric phosphate $FeH_3(PO_4)_2 . 2.5\ H_2O$. It was also found that in no case had either the pure phosphoric acid or any of the applied commercial rust transformers converted rust or some rust components into species which are able to form a closed protective layer inhibiting further corrosion.

Fujinami and Ujihara [87] investigated the corrosion product on a steel exposed to a sulphur dioxide atmosphere. The formation of $FeSO_4.H_2O$ as the initial product, $FeSO_4.4H_2O$ as the intermediate product and γ-FeOOH as the final corrosion product was confirmed by analysis of the CEM spectra. The atmosphere was composed of moist air (relative humidity 95%) with 0.16 vol % of SO_2. The corrosion temperature was kept constant at 25°C throughout the experiment. It was found that the ferric compound located at the uppermost surface was substituted by the ferrous compound at greater depth. The same authors [88] also investigated the corrosion product on a steel in H_2S-N_2 and H_2S-O_2-N_2 environments. The initial corrosion product in the H_2S environment was identified as FeS_{1-x} (mackinawite). The next stage of the corrosion process is fairly complex and various processes have been suggested. The results of the CEMS study indicated the presence of an intermediate compound, which was thought to be ferrimagnetic mackinawite. Finally mackinawite transformed to gregite (Fe_3S_4). Further, it was confirmed that the presence of oxygen

in a H_2S environment promoted the production of iron sulphide which is subsequently easily oxidised to γ-FeOOH.

In another paper by Meisel [89], some examples of phase analysis of surface layers by Mössbauer spectroscopy were demonstrated. The inner surface of steel tubes of a hot water heating system were characterised. Fe_3O_4 was the main component. $FeCO_3$, iron carbonate, was also observed. A similar sample to which some phosphate was continuously added was also investigated. The inhibiting effect of the phosphate led to a thinner layer of the corrosion products, demonstrated by the higher intensity of the substrate lines (α-Fe) in the spectrum. Other samples were exposed to phosphated water for 4 and 8 month periods. The progress of corrosion is evident from the relative intensities of the relevant subspectra.

Sawicki [90] has recently reviewed the conversion electron Mössbauer technique in ion implantation studies. He concludes that much routine ^{57}Fe work in applied material science is required, and suggests the following areas: phase analysis; identification of impurity states; studies of thermal effects. ^{57}Fe CEMS analysis will become a routine method for the characterisation of iron-containing materials. Experiments will be combined with other techniques such as electron microscopy, X-ray methods, Auger electron spectroscopy, low energy electron

diffraction, proton-induced X-ray emission, Rutherford backscattering and ion channelling. Specialised ultrahigh vacuum equipment for combined measurements with these methods and CEMS will become available. Applied work will call for more precise data for impurity states in various materials. More studies of non-equilibrium alloy rules and statistical modelling of implanted impurities will be needed. Finally, it is suggested that the development of experimental techniques for CEMS will continue and the range of useful Mössbauer resonances will be extended beyond the ^{57}Fe, ^{119}Sn, ^{151}Eu and ^{197}Au resonances which are used at present.

Salvat and Parellada [91] have dealt with some of the theoretical aspects of the CEMS technique.

1.2.3 Depth Resolved Mössbauer Studies

In an extension of CEMS, in which the electrons are energy-analysed, known as depth selective conversion electron Mössbauer spectroscopy (DSCEMS), spectra are accumulated with selected electron energies. Each DSCEM spectrum will be weighted towards a particular depth in the sample, thus providing the possibility of depth profiling the immediate surface regions. A degree of depth profiling may be achieved with He/CH_4 detectors [92] or by evaporating overlayers onto the sample [93], but more accurate work requires the use of more sophisticated equipment.

In a pioneering paper, Bonchev et al [94] have described the design and use of a magnetic iron-free beta-ray spectrometer with intermediate image focussing for use in ^{119}Sn experiments. These workers were able to demonstrate that the ^{119}Sn CEM spectra of a brominated tin metal foil consisted of superpositions of peaks arising from α-Sn, SnO_2, $SnBr_2$ and $SnBr_4$. More significantly, the area ratios of the spectra components changed with changing electron energies in a manner which suggested that $SnBr_4$ at the surface overlayed a layer of $SnBr_2$. Other groups, notably Bäverstam and co-workers [95-98] constructed similar spectrometers and demonstrated the feasibility of making depth-resolved measurements with ^{57}Fe. Because the electron spectrum is now energy resolved, the count rates are lower than those obtained with integral detectors and the use of enriched samples is unavoidable if acquisition times are to be realistic. As an example, Bäverstam et al [97] have presented spectra of a stainless steel foil covered with 36 nm of iron recorded at various electron energies. The change in surface to substrate signal was clearly shown to be a function of the electron energy.

A high resolution electrostatic electron spectrometer was combined with a Mössbauer spectrometer and used to obtain depth selective ^{57}Fe Mössbauer spectra by Shigematsu et al [99]. Conversion electrons in the energy range between 6.6 and 7.3 keV were detected. A 25 nm iron film (95% enriched) was vacuum deposited onto a 91% enriched

stainless steel foil substrate. Depth selectivity was clearly demonstrated from the spectra obtained. A typical six line α-Fe signal from the 25 nm iron film was shown to be clearly enhanced relative to the central stainless peak of the substrate if electrons of 7.3 keV are detected. Detecting electrons of progressively lower energies reduces the α-Fe overlayer signal and enhances the stainless steel peak intensity. At a 6.6 keV electron energy setting, the stainless steel line dominates and the α-Fe pattern is hardly detectable.

Belozerskii et al [100] applied DSCEMS to the study of very thin surface layers. A very thin oxide layer was confirmed by electron spectroscopy for chemical analysis (ESCA). The Mössbauer spectrum did not reveal this thin oxide layer, and it was concluded that the recoil free fraction in this layer was practically zero at room temperature. Further work following the installation of a cryogenic system was suggested. Staniek et al [101] disagreed with this interpretation and showed that when detecting conversion electrons of 7.3 keV energy, the CEMS spectrum revealed the six α-Fe lines plus some additional absorption in the central area. This was assigned as a broad single line with an isomer shift, relative to α-Fe, of + 0.24 mms^{-1}, typical of Fe^{3+} ions. The recoil free fraction in this thin surface layer is thus not zero at room temperature but remains reasonably high. A similar study was undertaken by Shinjo et al [102]. An enriched ^{56}Fe layer of 21 nm thickness was

deposited on a mylar substrate, followed by various thicknesses of an ^{57}Fe layer. The samples were exposed to the atmosphere and then examined at 300 K and at 4.2 K. An oxide similar to γ-Fe_2O_3 with a non-collinear spin arrangement was identified at liquid helium temperature. Superparamagnetic relaxation at 300 K gave rise to broadened lines and the authors suggested this as a probable reason why the observation of thin oxide absorption is difficult at 300 K when the oxide fraction is a minor part of the sample. They concluded that surface enriched samples are very useful for the study of surface oxidation especially in the early stages, and that measurements at low temperatures are essential.

Similarly prepared samples were subsequently coated with various thicknesses of antimony. These samples were used to investigate oxidation at the interface between iron and antimony. Liljequist et al [103] investigated the depth and surface selectivity of DSCEMS using a high resolution electron energy analyser combined with a Mössbauer spectrometer. DSCEM spectra were recorded in ultrahigh vacuum at electron energies ranging from 6.5 to 7.3 keV, with an energy resolution of 2.7%, and at different electron emission angles, θ, relative to the absorber surface normal. A test absorber consisting of a thin α-Fe layer on a thick stainless steel substrate was employed. The α-Fe and stainless steel Mössbauer spectra areas were found to be in very good agreement with theoretically calculated values. The predicted angular

effects were verified and it was confirmed that the surface signal is enhanced by measuring at glancing angles relative to the absorber surface. The angles θ = 10°, 46°, 60° and 72° were used, and measuring time per spectrum ranged from 14 to 58 hours.

In a similar study, Frost et al [104] used the phenomenon of the total external reflection (TER) of gamma rays incident at grazing angles to the surface in conjunction with CEMS. A multilayer sample of two ^{57}Fe layers separated by a gold layer on a silicon wafer support was prepared. After confirming by CEMS that all the ^{57}Fe was present as iron metal, the top layer of iron was gently oxidised, the gold layer providing an unambiguous break between the iron and iron oxide. It was then demonstrated that the surface oxide layer could be selectively detected by controlling the angle of the incident gamma ray beam. It is also suggested that below a critical angle, the gamma rays do not penetrate the bulk of the sample and the photoelectron background is therefore greatly reduced.

Several papers have been concerned with theoretical aspects of DSCEMS. Software and interactive methods for DSCEMS data interpretation and quantitative analysis are described by Liljequist and co-workers [105]. The same author [106] determined the simultaneous energy loss and angular distribution of internal conversion electrons as a function of their starting depth in an iron sample.

It was suggested that, at extreme glancing angles, the selective observation of a surface layer with a mean depth of less than 1 nm may be possible. The method of applying these results to DSCEMS analysis using different types of electron spectrometers was also described. In a subsequent paper [107], the influence of surface roughness on conversion electron scattering and its effect in CEMS and DSCEMS analysis were considered. The results obtained suggested that it may be possible to estimate surface roughness from the energy loss profiles measured at different angles. The energy distributions of the 7.3 keV conversion electron through several thicknesses of iron film and its application to DSCEMS has been investigated by Itoh et al [108]. The method of analysis is described in detail. The energy distributions obtained are in fair agreement with those of the Monte Carlo calculations of Liljequist et al [109]. The weight coefficients for depth selective conversion electron Mössbauer spectroscopy are presented for energy resolution of 1, 2 and 3%.

1.2.4 Variable Temperature Backscatter Techniques

Several authors have detailed methods for recording CEM and DSCEM spectra at low temperatures. Sawicki et al [110] mounted a scattering sample and channeltron detector close to each other inside a small vacuum chamber. The Mössbauer source is located above the chamber and gammarays enter the chamber through an indium sealed beryllium window. The chamber can be

quickly and easily cooled by immersing in liquid nitrogen or liquid helium in ordinary storage vessels. In a later paper [111], the same authors modified their experimental arrangement such that the Mössbauer source is moved much closer to the absorber-detector. The close source-absorber-detector separation increases the efficiency of the spectrometer. Low temperature CEM spectra of ^{57}Fe, ^{119}Sn, ^{151}Eu and ^{182}W are presented as examples. In the ^{57}Fe CEMS experiments at low temperatures, the choice of a suitable source presents some problems. Source matrices of Cr, Pd and Pt show hyperfine broadening or splitting of lines at 4 K and even at 78 K. The previously described arrangement with the source at room temperature was therefore used for ^{57}Fe experiments. The modified experimental arrangement is shown to work well for the determination of the valence of implanted europium ions in europium-silicon alloys [112].

Atkinson and Cranshaw [113] describe a backscatter electron counter which detects low energy electrons of a few eV which are released when a conversion electron leaves the surface [114]. These electrons can be regarded as secondary electrons produced by the collision of the conversion electrons with the surface. The sample is held in good thermal contact with a cold finger maintained at liquid nitrogen temperature. The major advantages of this system are that the secondary electrons are accelerated away from the sample surface such that they enter the channeltron at an energy for which the

channeltron detection efficiency is at a maximum, and that the sample may be held at a low temperature without cooling the detector appreciably.

Sato et al [115] were able to measure depth selective CEM spectra in the temperature range 77-293 K using a cylindrical mirror type electrostatic electron spectrometer. A comparison was made between electron spectra of a ^{57}Co source obtained by the electron spectrometer and by a He-CH_4 gas flow proportional counter. CEM spectra of an ^{57}Fe enriched stainless steel foil were also obtained, at 293 K and 195 K. In a later publication, the same group [116] obtained CEM spectra with an electron spectrometer for 6.6 - 7.3 keV ^{57}Fe electrons scattered from solid surfaces. Depth resolved conversion electron spectra of corrosion products in the surface layer of an iron foil were measured and the thickness of the layer was estimated to be 15 nm. One of the corrosion products was identified as β-FeOOH. The technique was also used to characterise an iron complex, potassium tris(oxalato)-ferrate(III), $K_3[Fe(C_2O_4)_3].3H_2O$, which had been photoirradiated. Several reaction products were postulated.

A channeltron detector system for CEM spectroscopy at high temperatures has been developed by Kowalski et al [117]. CEM spectra of a metallic iron foil enriched to 90% in ^{57}Fe at several temperatures below and above

the Curie point of iron (1033 K) are presented. The reduction in hyperfine field with increasing temperature and final collapse of the magnetic detail are clearly visible in the spectra. A similar series of spectra of a lithium fluoride single crystal doped with ^{57}Fe and annealed in vacuo at 873 K are also presented.

REFERENCES

1. D.C. Kistner, A.W. Sunyar, Phys. Rev. Lett., 4, p 412, 1960.

2. F. Van der Woude, Phys. Stat. Sol., 17, p 417, 1966.

3. K. Ono, A. Ito, J. Phys. Soc. Japan, 17, p 1012, 1962.

4. W. Kündig, H. Bömmel, G. Constabaris, R.H. Lindquist, Phys. Rev., 142, p 327, 1966.

5. W. Kündig, K.J.Ando, R.H. Linquist, G. Constabaris, Czech. J. Phys., B17, p 467, 1967.

6. N. Yamamoto, J. Phys. Soc. Japan, 24, p 23, 1968.

7. Yu F. Krupyanskii, I.P. Suzdalev, Sov. Phys. - Sol. St., 17, p 375, 1975.

8. R.C. Nininger Jnr, D. Schroeer, J. Phys. Chem. Soc., 39, p 137, 1978.

9. I.P. Syzdalev, Sov. Phys. Sol. St., 12, p 775, 1970.

10. A.M. Van der Kraan, Phys. Stat. Sol., 18A, p 215, 1973.

11. T. Shinjo, M. Kiyama, N. Sugita, K. Watanabe, T. Takada, J. Magn. Magn. Mats., 35, p 133, 1983.

12. R.J. Armstrong, A.H. Morrish, G.A. Sawatzky, Phys. Letts., 23, p 414, 1966.

13. J.M.D. Coey, D. Khalafalla, Phys. Stat. Sol (a), 11, p 229, 1972.

14. K. Haneda, A.H. Morrish, Sol. St. Comm., 22, p 779, 1977.

15. K. Haneda, A. H. Morrish, Phys. Letts., 64A, p 259, 1977.

16. G. Longworth, M.S. Tite, Archaeometry, 19, p 3, 1977.

17. S. Kitahata, M. Kishimoto, M. Amemiya, J. Appl. Phys., 57, 1, p 3931, 1985.

18. E.J.W. Verwey, Nature, 144, p 327, 1939.

19. E.J.W. Verwey, P.W. Haayman, Physica, 8, p 979, 1941.

20. E.J.W. Verwey, J. Chem. Phys., 15, p 181, 1947.

21. W.C. Hamilton, Phys. Rev., 110, p 1050, 1958.

22. W. Kündig, R.S. Hargrove, Solid State Comm., 7, p 223, 1961.

23. A.M. van Diepen, Phys. Lett., 57A, p 354, 1976.

24. A.M. van Diepen, Physica, 86-88B, p 955, 1977.

25. L. Häggström, Hyperfine Interactions, 5, p 201, 1978.

26. R.S. Hargrove, W. Kündig, Solid State Commun., 8, p 303, 1970.

27. M. Rubinstein, D.W. Forester, Solid State Commun., 9, p 1675, 1971.

28. S. Mørup, H. Topsøe, J. Lipka, J. Phys. Colloq., 37, C6-287, 1976.

29. S. Mørup, H. Topsøe, J. Magn. Magn. Mats, 31-34, p 953-4, 1983.

30. T. Takada, M. Kiyama, Y. Bando, T. Nakamura, M. Shiga, T. Shinjo, N. Yamamoto, Y. Endoh, H. Takaki, J. Phys. Soc. Jpn., 19, p 1744-5, 1964.

31. M.J. Rossiter, A.E.M. Hodgson, J. Inorg. Nucl. Chem., 27, p 63-71, 1965.

32. A.Z. Krynkiewicz, Phys. Letts., 17, p 93, 1965.

33. A.Z. Hrynkiewicz, D.S. Kulgawczuk, Acta Phys. Polon., 24, p 689, 1963.

34. T. Shinjo, J. Phys. Soc. Japan, 21, p 917, 1966.

35. A.M. van der Kraan, J.J. van Loef, Phys. Letts., 20, p 614, 1966.

36. F. van der Weude, A.J. Dekker, Phys. Stat. Sol., 13,p181, 1966.

37. I. Dezsi, M. Fodor, Phys. Stat. Sol., 15, 247, 1966.

38. J.B. Forsyth, I.G. Hedley, C.E. Johnson, J. Phys. C Ser. 2, 1, p 179, 1968.

39. N. Yamamoto, J. Phys. Soc. Japan, 25, p 1267, 1968.

40. A. Govaert, J. de Phys., 37, C6, p 825, 1976.

41. A. Govaert, Sol. State Commun., 18,p389, 1976.

42. A. Govaert, J. de Phys., 37, C6, p 291, 1976.

43. I. Dezsi, L. Keszthelyi, D. Kulgawczuk, B. Molnar, N.A. Eissa, Phys. Stat. Sol., 22, p 617, 1967.

44. A.T. Howe, K.J. Gallagher, J. Chem. Soc. Faraday Proc., p 22, 1975.

45. C.S. Hogg, Min. Mag., 40, p 89, 1975.

46. N.E. Logan, Aust. J. Soil Res., 14, p 217, 1976.

47. J.H. Johnston, Geochim and Cosmochim Acta, 41, p 539, 1977.

48. D. Chambaere, E. De Grave, J. Magn. Magn. Mats., 42, p 263, 1984.

49. D. Chambaere, E. De Grave, Phys, Stat. Sol. (a), 53, p 93, 1984.

50. D. Chambaere, E. De Grave, J. Magn. Magn. Mats., 44, p 349, 1984.

51. D. Chambaere, E. De Grave, Hyperfine Int., 20, p 249, 1984.

52. D. Chambaere, E. De Grave, Phys. Chem. Miner., 12, p 176, 1985.

53. C.E. Johnson, J. Phys. C Ser. 2, 2, p 1996, 1969.

54. E. Murad, U. Schwertmann, Mineralogical Mag., 48, p 507, 1984.

55. K.M. Creer, J. Geomag. and Geoelec., 13, p 86, 1962.

56. S. Okamoto, J. Am. Ceramic Soc., 51, 10, p 594, 1968.

57. M. Pernet, X. Obradors, J. Fontcuberta, J.C. Joubert, J. Tejada, IEEE Trans. Mag. Mag 20, 5, p 1524, 1984.

58. W. Meisel, Spectrochim. Acta, 39B, 12, p 1505, 1984.

59. T. Péev, M.K. Georgieva, S. Nagy, A. Vertes, Radiochem. Radioanal. Letts., 33 (4), p 265, 1978.

60. T. Péev, S. Nagy, A. Vertes, I. Dobrevskii, Radiochem. Radioanal. Letts., 39 (1), p 47, 1979.

61. P.C. Bhat, N.G. Puttaswamy, R.M. Mallya, Radiochem. Radioanal. Letts., 52 (5), p 299, 1982.

62. P.C. Bhat, M.P. Sathyavathiamma, N.G. Puttaswamy, Corr. Sci., 23, 7, p 733, 1983.

63. H. Leidheiser, S. Music, Corr. Sci., 22, 12, p 1089, 1982.

64. H. Leidheiser, I. Czako-Naky, Corr. Sci., 24, 7, p. 569, 1984.

65. R.K. Nigam, U.S. Mehrotra, S. Varma, S.N. Pandley, Jaipur Conf., p 299, 1982.

66. A.K. Singh, T. Ericsson, L. Häggström, Corrosion Science, 25, 10, p 931, 1985.

67. M.J. Tricker, Conversion Electron Mössbauer Spectroscopy and its Recent Develcpment in: Mössbauer Spectroscopy and its Chemical Applications, American Chemical Society, 1981.

68. G. Longworth, X-ray and Conversion Electron Mössbauer Scattering for Chemists in: Mössbauer Spectroscopy Applied to Inorganic Chemistry, Vol 1, Edited by G.J. Long, 1984.

69. K.R. Swanson, J. Spijkermann, J. Appl. Phys., 41, p 3155, 1970.

70. G. Longworth, R. Atkinson, in Mössbauer Spectroscopy and its Chemical Applications, Adv. Chem. Ser., 194, 103, 1981.

71. S.C. Thorpe, Report No 4, Department of Applied Physics, Sheffield City Polytechnic, 1984.

72. G.W. Simmons, Corrosion, 29, p 227, 1973.

73. A. Sette Camara, W. Keune, Corrosion Sci., 15, p 441, 1975.

74. M.J. Graham, Oxidation of Metals, 12, 3, p 247, 1978.

75. F.J. Berry, Trans. Met. Chem., 4, p 209, 1979.

76. F.J. Berry, A.G. Maddock, J. C. S. Chem. Comm. No 7, p 308, 1978.

77. F.J. Berry, J. C. S. Dalton Trans., No 11, p 1736, 1979.

78. J. Ensling, Corr. Sci., 18, p 797, 1978.

79. F.J. Berry, M.E. Brett, P. Bowen, W. Jones, J. C. S. Dalton Trans. No 7, p 1450, 1981.

80. M. Inaba, H. Nakagawa, Y. Ujihara, J. Mater. Sci. Letts., 16, p 1712, 1981.

81. G.P. Huffman, H.H. Podgurski, Oxidation of Metals, 15, 3/4, p 323, 1981.

82. M.J. Graham, D.F. Mitchell, D.A. Channing, Oxid. Met., 12, p 247, 1978.

83. W. Meisel, E. Mohs, H.J. Guttman, P. Gütlich, Corrosion Science, 23, No 5, p 465, 1983.

84. T. Shigematsu, H-D. Pfannes, W. Keune, Electron Spectrometer for ^{57}Fe Mössbauer Spectroscopy in: Mössbauer Spectroscopy and its Chemical Applications, American Chemical Society, 1981.

85. W. Meisel, H.J. Guttmann, P. Gütlich, Corrosion Science, 23, No 12, p 1373, 1983.

86. W. Meisel, P. Gütlich, Werkstoffe Korros., 32, p 296, 1981.

87. M. Fujinami, Y. Ujihara, Applications of Surface Science, 17, p 265, 1984.

88. M. Fujinami, Y. Ujihara, Applications of Surface Science, 17, p 276, 1984.

89. W. Meisel, Spectrochimica Acta, 39B, No 12, p 1505, 1984.

90. J.A. Sawicki, Materials Science and Engineering, 69, p 501, 1985.

91. F. Salvat, J. Parallada, Nuc. Instrms. Methods in Phys. Res., B1, p 70, 1984.

92. M.J. Tricker, A.G. Freeman, A.P. Winterbottom, J.M. Thomas, Nucl. Instr. Methods, 135, p 117, 1976.

93. M.J. Tricker, L.A. Ash, W. Jones, Surf. Sci., 79, L333, 1979.

94. Z.W. Bonchev, A. Jordanov, A. Minkova, Nucl. Instrm. Methods, 70, p 36, 1969.

95. U. Bäverstam, C. Bohm, T. Ekdahl, D. Liljequist, B. Ringström, in "Mössbauer Effect Methodology", Plenum, New York, 9, p 259, 1974.

96. U. Bäverstam, T. Ekdahl, C. Bohm, B. Ringström, V. Stefansson, D. Liljequist, Nucl. Instrm. Methods, 115, p 373, 1974.

97. U. Bäverstam, T. Ekdahl, C. Bohm, D. Liljequist, B. Ringström, Nucl. Instrm. Methods, 118, p 313, 1974.

98. U. Bäverstam, C. Bohm, B. Ringström, T. Ekdahl, Nucl. Instrm. Methods, 108, p 439, 1973.

99. T. Shigematsu, H.-D. Pfannes, W. Keune, Phys. Rev. Letts., 45, No 14, p 1206, 1980.

100. G. N. Belozerskii, C. Bohm, T. Ekdahl, D. Liljequist, Nucl. Instrm. Methods, 192, - 539, 1982.

101. S. Staniek, T. Shigematsu, W. Keune, H.-D. Pfannes, J. Magn. Magn. Mats., 35, p 347, 1983.

102. T. Shinjo, T. Iwasaki, T. Shigematsu, T. Takada, Japan. J. App. Phys., 23, No3, p 283, 1984.

103. D. Liljequist, M. Ismail, K. Saneyoshi, K. Debusmann, W. Keune, R.A. Brand, W. Kiauka, Physical Review B, 31, No 7, p 4137, 1985.

104. J.C. Frost, B.C.C. Cowie, S.N. Chapman, J.F. Marshall, App. Phys. Letts., 47, 6, p 581, 1985.

105. D. Liljequist, C. Bohm, T. Ekdahl, Nucl. Instms. Methods, 177, p 495, 1980.

106. D. Liljequist, M. Ismail, Physical Review B, 31, 7, p 4131, 1985.

107. D. Liljequist, M. Ismail, Nucl. Instrms. Methods in Phys. Res. A, 239, p 273, 1985.

108. J. Itoh, T. Toriyama, K. Saneyoshi, K. Hisatabe, Nucl. Instrms. Methods, 205, p 279, 1983.

109. D. Liljequist, T. Ekdahl, U. Bäverstam, Nucl. Instrms. Methods, 155, p 529, 1978.

110. J.A. Sawicki, T. Tyliszczak, O. Gzewski, Nucl. Instrms. Methods, 190, p 433, 1981.

111. J.A. Sawicki, T. Tyliszczak in Jaipur Conf. Jaipur India, p 800, 1982.

112. J.A. Sawicki, T. Tyliszczak, B.D. Sawicki, J. Kowalski, Physics Letters, 91A, No 8, p 414, 1982.

113. R. Atkinson, T.E. Cranshaw, Nucl. Instrms. Methods, 204, p 577, 1983.

114. J.C. Riviére, Contemp. Phys., 14, p 513, 1973.

115. H. Sato, M. Matsuo, M. Takeda, N. Morikawa, T. Tominaga, Int. J. Appl. Radiat. Isot., 34, No 4, p 709, 1983.

116. M. Matsuo, H. Sato, T. Tominaga, Radiochimica Acta, 35, p 227, 1984.

117. J. Kowalski, J. Stanek, T. Tyliszczak, J. A. Sawicki, Nucl. Instrums. Methods, 216, p 299, 1983.

CHAPTER 2 : THE MÖSSBAUER EFFECT, HYPERFINE INTERACTIONS AND RELAXATION PHENOMENA

2.1 Recoilless Nuclear Resonance Absorption

2.2 Hyperfine Interactions

2.3 Particle Size Effects

References

CHAPTER 2 : THE MÖSSBAUER EFFECT, HYPERFINE INTERACTIONS AND RELAXATION PHENOMENA

Recoilless Resonance Fluorescence was first observed in a nuclear system during R.L. Mössbauer's graduate work in 1957 [1]. The subsequent development of the application of Mössbauer Spectroscopy has primarily been concerned with the isotopes ^{57}Fe and ^{119}Sn; nevertheless over 50 isotopes have been shown to exhibit this effect and more than 20 can give useful information without extreme experimental difficulty.

2.1 Recoilless Nuclear Resonance Absorption

Radioactive ^{57}Fe is produced by the electron capture decay of ^{57}Co ($t_{\frac{1}{2}}$ = 270 days), which is produced by a nuclear reaction. ^{56}Fe is bombarded with deuterons ($^{2}_{1}H$) and ^{57}Co is formed along with neutrons. The reaction may be represented as follows:

$$^{56}_{26}Fe + ^{2}_{1}H \rightarrow ^{57}_{27}Co + ^{1}_{0}n$$

$$^{57}_{27}Co + ^{0}_{-1}\beta \rightarrow ^{57}_{26}Fe^{*}$$

^{57}Fe is produced in a nuclear excited state represented by $^{57}Fe^{*}$, which may decay to the ground state with the emission of 3 γ rays (14.4, 122, 136.4 keV)

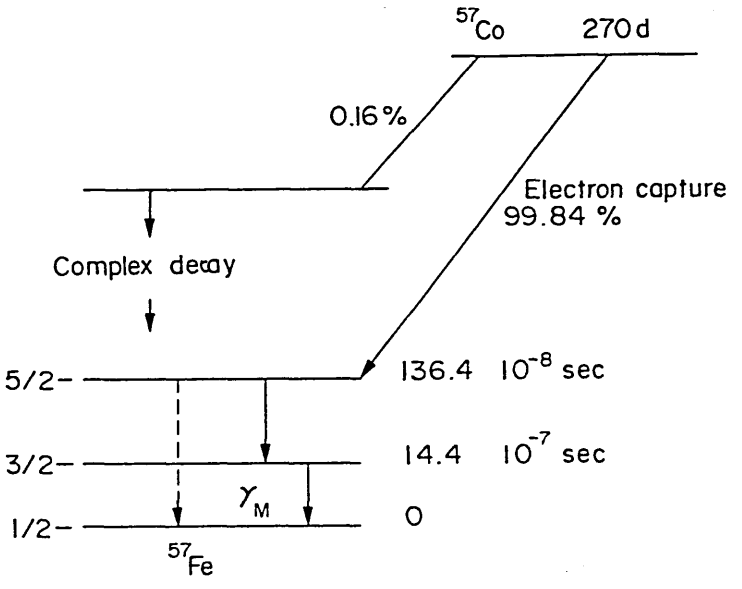

Figure 2.1 : Decay Scheme for ^{57}Co

The 14.4 keV transition results in the common Mössbauer photon. If a second ^{57}Fe nucleus initially in the ground state, absorbs the photon to produce ^{57}Fe*, then this process is described as nuclear resonance absorption.

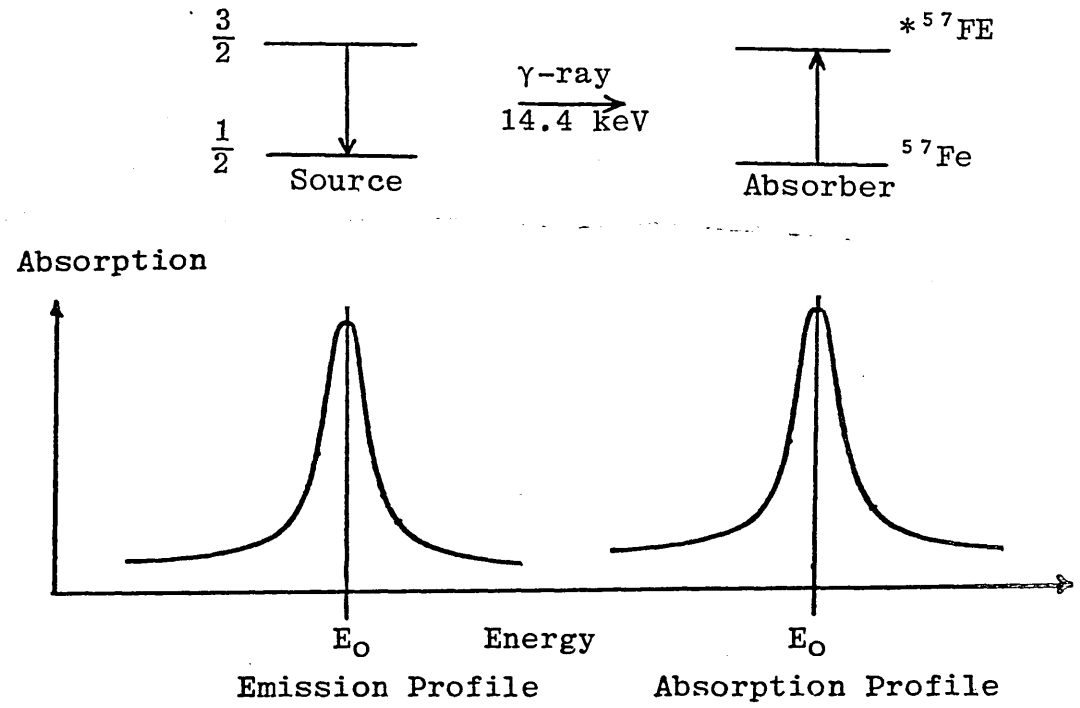

Superposition of the emission and absorption profiles give resonant absorption

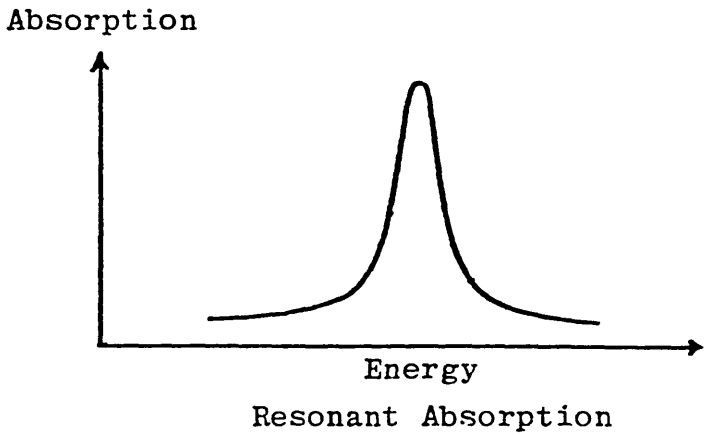

Figure 2.2 : The Process of Recoilless Nuclear Resonance Fluoresence in ^{57}Fe

2.1.2 Line Width of the Emitted Gamma Ray

The emitted γ-rays from the source have a Lorentzian energy distribution about a mean energy E_o and have a natural line width, Γ, shown in Figure 2.3.

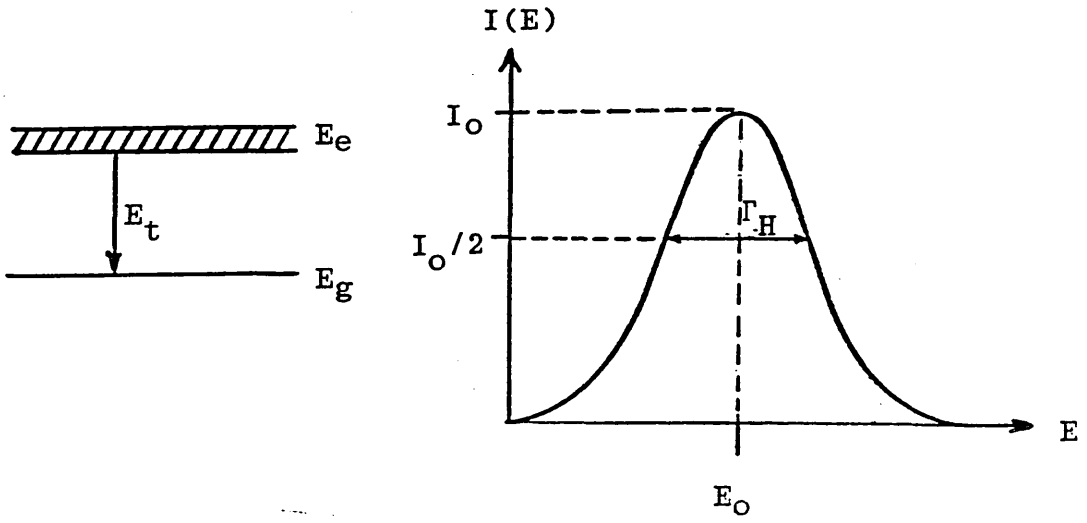

Figure 2.3 : The Lorentzian Distribution of Emitted γ-rays

The energy distribution of the γ-rays is defined by the Breit-Wigner equation [2]:

$$I(E) = \frac{f_s \Gamma}{2\pi} \frac{1}{(E - E_o)^2 + (\Gamma/2)^2} \qquad (2.1)$$

where $I(E)$ = Intensity of the distribution at energy E.

f_s = Probability of emission from the source.

Γ = Natural line width - determined from the Heisenberg Uncertainty Principle

i.e. $\Gamma = h/\tau$

E_o = Transition energy.

τ = Mean lifetime of the excited state.

One of the most important influences on the γ-ray energy distribution is the mean lifetime of the excited state (τ). The ground state nuclear energy level has an infinite lifetime and therefore zero uncertainty in energy whereas the excited state has a mean lifetime of typically $10^{-10} - 10^{-6}$ s. There will be a spread of γ-ray energies of width Γ_H at half height.

The full width at half height determines the limit of resolution of the technique. For example, for ^{57}Fe which has an excited state of mean lifetime 1.4114×10^{-7} s, then $\Gamma_H = 9.3272 \times 10^{-9}$ eV. Where Γ_H is the Mössbauer linewidth = 2Γ.

The transition energy is 14.41 keV, thus:

$$\frac{\Gamma_H}{E} = \frac{9.3272 \times 10^{-9}}{14.41 \times 10^{3}} = 6.4727 \times 10^{-13}$$

i.e. a resolution of better than 1 part in 10^{12} is theoretically possible.

2.1.3 Recoil Energy Loss and Doppler Broadening

It has been assumed that, as a result of the transition from the excited state to the ground state, the emitted photon has an energy, E_γ, equal to the transition energy, E_t, i.e. $E_\gamma = E_e - E_g$. In general, this is not the case. If the photon is emitted from a nucleus of mass M moving with an initial velocity V_x (due to random thermal motion) in the chosen x direction at the moment of emission, then

its total energy above the ground state nucleus at rest is $(E + \frac{1}{2}MV_x^2)$. After emission, the γ-ray will have an energy E_γ and the nucleus a new velocity $(V_x + v)$ due to recoil (Figure 2.4).

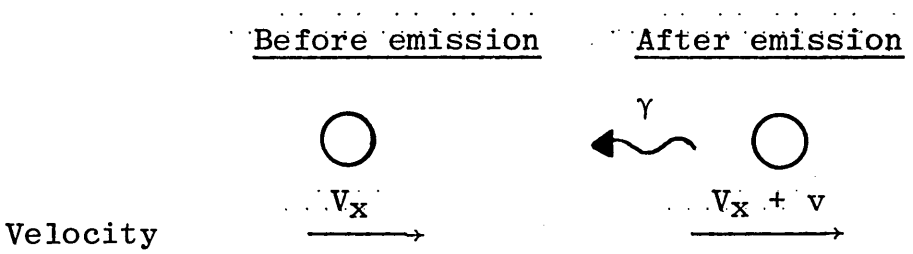

Energy	$E + \frac{1}{2}MV^2$	=	$E_\gamma + \frac{1}{2}M(V_x + v)^2$
Momentum	MV_x	=	$M(V_x + v) + E_\gamma/c$

Figure 2.4 : The Energy and Momentum are Conserved in the γ Emission Process

By conservation of energy

$$E_e + \tfrac{1}{2}MV_x^2 = E_g + E_\gamma + \tfrac{1}{2}M(V_x + v)^2 \qquad (2.2)$$

Since $E_t = E_e - E_g$, then (2.3)

$$\delta E = E_t - E_\gamma = \tfrac{1}{2}MV_x^2 + MvV_x \qquad (2.4)$$

$$\therefore \quad \delta E = E_R + E_D \qquad (2.5)$$

The γ-ray energy is thus seen to differ from the nuclear energy level separation by an amount which depends on the recoil kinetic energy, $E_R + \frac{1}{2}MV^2$, independent of the velocity V_x, and by $E_D = MvV_x$ which is proportional to the atom velocity V_x and is a Doppler effect energy. Thus, emission of the γ-ray from the source results in a

shift in energy of the emission energy profile of the order $E_\gamma = E_t - E_R$. For resonant absorption to occur, a γ-ray energy of $E_\gamma = E_t + E_R$ is required, hence there is an energy difference of $2E_R$. The effect of E_R on the emission and absorption energy distributions is shown in Figure 2.5.

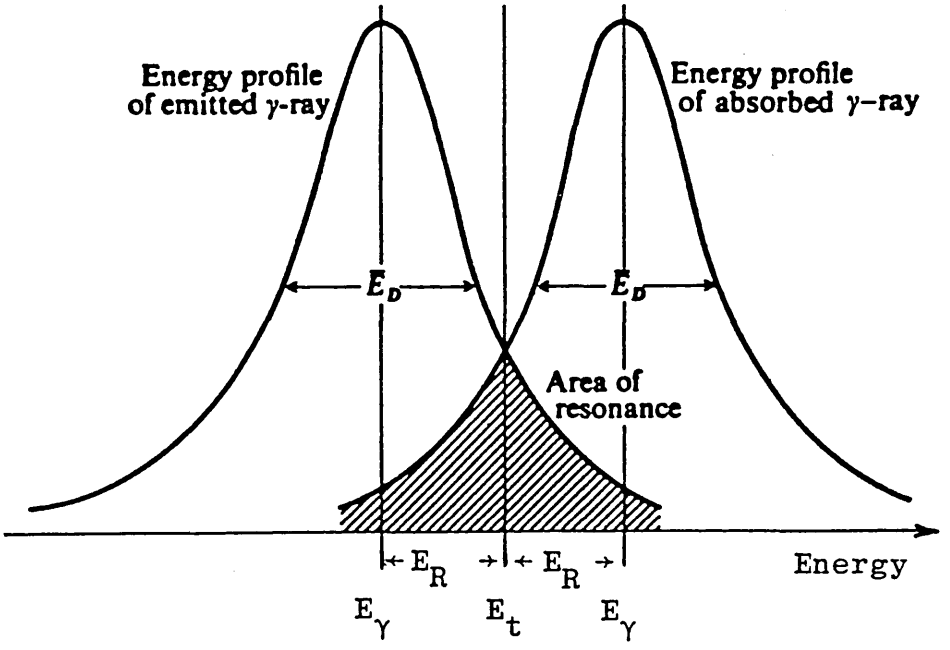

Figure 2.5 : The Effect of Thermal Doppler Broadening and Recoil on the Energy Profiles of Emitting and Absorbing Nuclei

In addition, the emission and absorption energy profiles experience Doppler broadening, E_D, arising from random thermal velocities of the source and absorber.

The kinetic energy of a nucleus in the x direction from recoil is given by:

$$E_K = \tfrac{1}{2}MV_x^2 \approx \tfrac{1}{2}KT \qquad (2.6)$$

and $$(V_x^2)^{\frac{1}{2}} = \sqrt{\frac{2E_K}{M}} \qquad (2.7)$$

Substituting for $(V_x^2)^{\frac{1}{2}}$ in (2.4) gives:

$$E_D = 2\sqrt{E_R.K.T} \qquad (2.8)$$

Thus the γ-ray distribution is shifted by E_R and broadened by twice the mean of the recoil energy and the average thermal energy. The probability that resonance will occur depends on the magnitude of E_R. For transition energies of the order of 10^4 eV, E_R is significant and overlap of the energy profiles is poor. In order to observe resonance fluoresence, it is necessary to eliminate the effects of recoil and of Doppler broadening.

2.1.4 Energy and Momentum Transfer to the Lattice

In 1958, Mössbauer discovered that, under certain conditions, nuclei embedded in lattices at 'low' temperatures were effectively frozen in the lattice, and hence unable to recoil and experience Doppler broadening of their emission and absorption lines. This "freezing" arises due to the quantised nature of the lattice vibrations.

Classically, the atoms of a solid vibrate about their equilibrium positions with an energy that varies continuously with temperature. However, Einstein realised that a solid is a quantum mechanical system and therefore

its energy should be quantised and transitions could only occur through phonon interactions. The Einstein energy, E_e, is the minimum energy required to excite the lattice and corresponds to a single phonon transition. The vibrational energy of the lattice can only change by discrete amounts 0, $\pm\hbar\omega$, $\pm 2\hbar\omega$ etc., ($\hbar\omega = E_e$, the Einstein energy) and depending on its magnitude, the recoil energy of a single nucleus can be taken up either by the whole crystal or it can be transferred to the lattice through phonon interactions, thereby increasing the vibrational energy of the crystal. If the recoil energy is less than E_e, then a zero phonon interaction occurs, no energy is transferred to the lattice and the recoil is taken up by the whole crystal. If the recoil energy is greater than E_e, many phonon interactions may be involved and the energy is transferred to the vibrational energy of the lattice. Consequently, the emitted γ-ray suffers energy recoil and is Doppler broadened.

For many low energy transitions in solids at low temperatures, there is a finite probability of emission of γ-rays without recoil energy loss. This probability is termed the recoilless fraction "f" and is expressed as:

$$f = \exp\left[\frac{-4\pi^2 \langle x\rangle^2}{\lambda^2}\right] \qquad (2.9)$$

where $\langle x^2\rangle$ is the mean square vibrational amplitude of the emitting (or absorbing) nucleus in the solid, λ is

the wavelength of the photon.

This expression is obtained by reducing the Hamiltonian operator for the atom to one term which represents the transition from the initial vibrational state L_i to the final vibrational state L_f. [3]

$$\text{i.e.} \quad f = \text{constant} \quad | < L_f | e^{ik.x} | L_i > |^2 \qquad (2.10)$$

where k is the wave vector for the emitted γ photon (the number of units of momentum it carries = $E_\gamma/\hbar c$), x is the co-ordinate vector of the centre of mass of the decaying nucleus.

Since $<x^2>$ depends upon the binding energy and temperature, the displacement must be kept to a minimum to observe the Mössbauer effect. (Since f increases as $<x^2>$ decreases) In the Debye model, the solid is assumed to be composed of a continuum of oscillator frequencies [3], which allows the recoilless fraction to be evaluated as:

$$f = \exp\left[\frac{-6E_R}{k\Theta_D}\left\{\frac{1}{4} + \left(\frac{T}{\Theta_D}\right)^2 \int_0^{\Theta_D/T} \frac{x\,dx}{e^x - 1}\right\}\right] \qquad (2.11)$$

The integral can only be solved under certain conditions [3], i.e. at absolute zero and at high temperatures where the expression reduces to

$$(1) \quad \text{At Absolute zero} : f = \exp\left[-\frac{3E_R}{2k\Theta_D}\right] \qquad (2.12)$$

(2) At the high temperature limit (where $T > \Theta_D$)

$$f = \exp\left[-\frac{3E_R}{2k\Theta_D} - \frac{6E_R \cdot T}{k\Theta_D^2} \right] \qquad (2.13)$$

2.1.5 Observation of the Mössbauer Effect

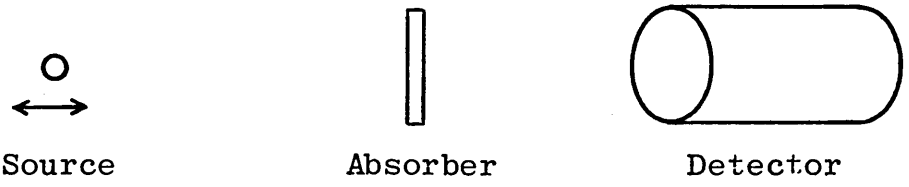

Figure 2.6 : Schematic Representation of a Mössbauer Spectrometer

Consider the 14.4 keV γ photon emitted by a ^{57}Co source and an absorber containing ^{57}Fe in an identical lattice. The radiation which passes through the absorber will be less than expected due to resonant absorption and subsequent re-emission over a 4π solid angle. If a Doppler velocity is applied to the source with respect to the absorber, then a shift in the energy of the source spectral line will be observed according to the Doppler relationship $E_\gamma = E_o \pm \frac{E_\gamma V}{c}$. If a range of velocities are scanned, then at a particular velocity when the emission and absorption profiles are exactly coincident, resonance absorption will be at a maximum (Figure 2.7). At higher or lower velocities, the resonance will decrease until it is effectively zero. A Mössbauer spectrum is thus a plot of absorption against a series of Doppler velocities between the source and absorber.

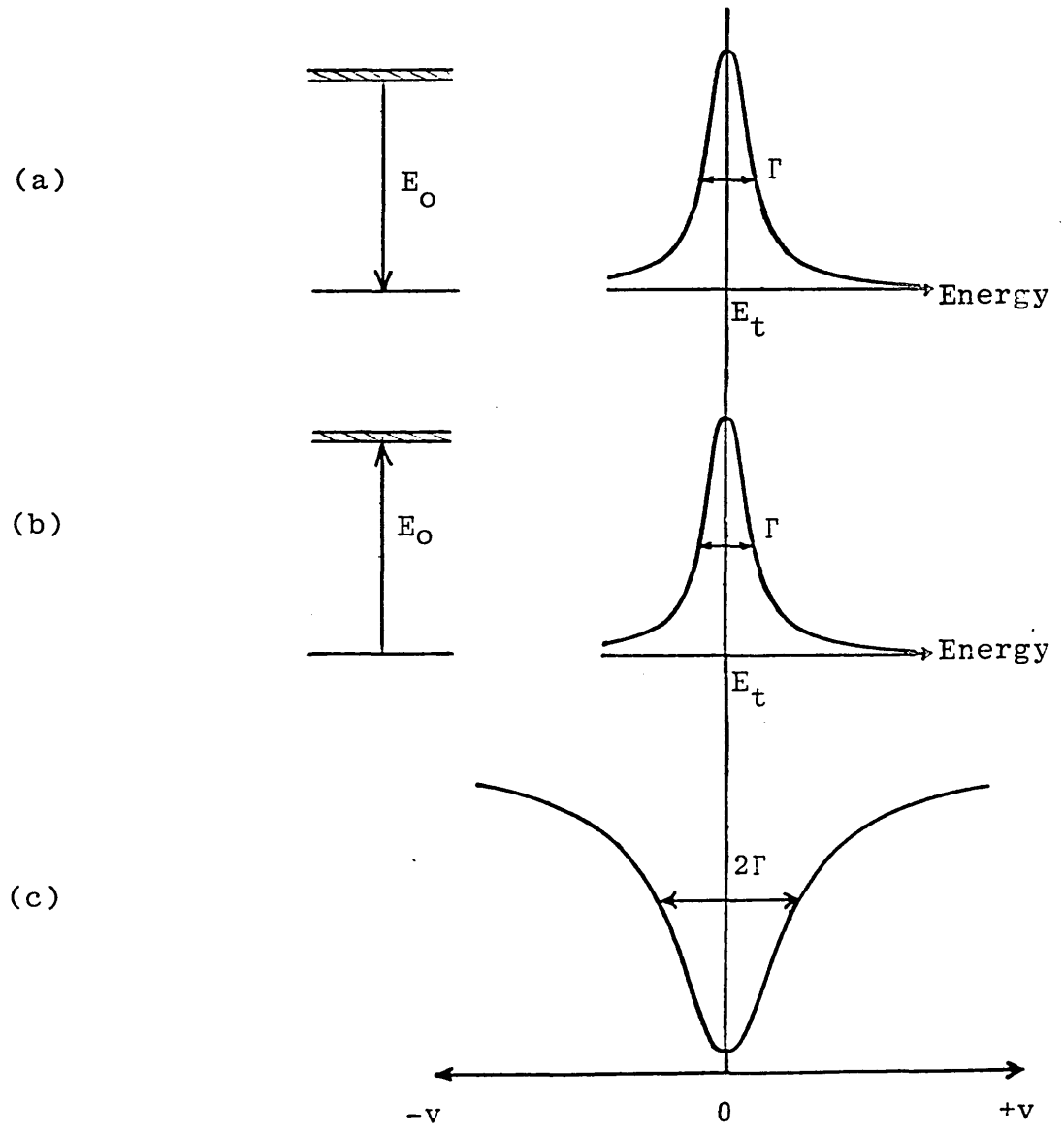

Figure 2.7 : (a) Emission Energy Spectrum, (b) Absorption Energy Spectrum, (c) Resultant Mössbauer Spectrum

Similarly, a Doppler velocity can be used to achieve resonance when the transition energies of the source and absorber are different. These differences in the nuclear energy levels are directly related to the electronic and magnetic environment of the absorbing

nuclei. The Mössbauer technique thereby provides a powerful method of investigating the chemical environment of the nucleus.

2.2 Hyperfine Interactions

Application of the Mössbauer effect exploits its precise energy resolution. The natural line width of the Mössbauer radiation expressed as a fraction of the transition energy Γ/E_o, may be as low as 5×10^{-16}. The line widths are comparable with or less than the interaction energies between the nuclei and their extranuclear electric and magnetic fields. These interactions between the nucleus and its environment are called hyperfine interactions.

It is normal to study the hyperfine interactions in absorbers containing the stable Mössbauer isotope using a single line source. The source matrix is chosen to have a line width as near to Γ as possible, and to have a large recoil free fraction. The radioactive source is mounted on a velocity transducer and the absorber fixed in a suitable manner. If the nuclear levels in the absorber are split by the hyperfine interactions, then there will be a number of different energies at which absorption can take place. A change in count-rate will be detected when the Doppler velocity applied to the source brings the emitted γ-ray into coincidence with the absorption energy.

These hyperfine interactions give rise to the Isomer shift, δ, Quadrupole splitting, ΔE_Q, and the Magnetic Zeeman Splitting, H. All three interactions can be expressed as the product of a nuclear term, which is a constant for a given Mossbauer γ-ray transition, and an electronic term (Table 2.1) which is related to the electronic structure of the resonant absorber being studied.

2.2.1 The Isomer Shift

For many purposes, it is adequate to consider the nucleus as a point charge which influences the extra-nuclear electrons via the coulombic potential. However, the nucleus has a finite volume, and this must be taken into account when considering nucleus-electron interactions because an s-electron wavefunction implies a non-zero electron charge density within the nuclear volume. During the course of a nuclear γ transition, it is usual for the effective nuclear size to change, thereby changing the nucleus-electron interaction energy. This change is only a minute fraction of the total coulombic interaction but is dependent upon the chemical environment of the nucleus. It is not possible to measure this energy change directly, but it is possible to compare values by means of a suitable reference, i.e. the γ-ray source used in recording the Mössbauer spectrum. The observed change in chemical isomer shifts for a given nuclide is frequently within an order of magnitude of the Heisenberg natural line width of the transition. The

Table 2.1 : Schematic Representation of Hyperfine Interactions

Solid State Factor	Magnetic Field	Electronic Field Gradient	Electron Density at Nuclear Site
Interaction	$\Delta E = \mu H$	$+ Q\nabla E$	$+ \text{const} \langle R^2 \rangle \rho(o)$
Nuclear Factor	Nuclear Magnetic Moment	Nuclear Quadrupole Moment	Mean Square Nuclear Charge Radius
	Magnetic Hyperfine Interaction	+ Electric Quadrupole Interaction	+ Isomeric Shift

Mössbauer resonance line recorded by velocity scanning may thus be measurably displaced from zero velocity if the chemical environment of the nuclide in the source and absorber differ.

The isomer shift can be computed classically by considering the effect of the overlap of s-electron density with the nuclear charge density.

Only s-electrons have a finite probability of overlapping with the nuclear charge density, and thus of interacting with it. However, the s-electron density at the nucleus is often sensitive to changes in p- or d-electron density because of shielding effects.

The nucleus is assumed to be a uniformly charged sphere of radius, R, and the s-electron density at the nucleus, $[\psi(O)_s]^2$, is assumed to be constant over the nuclear dimensions. By computing the difference between the electrostatic interaction of a point nucleus and the interaction of a nucleus having a radius R the interaction energies can be estimated. [3,4,5] The difference in energy is given by

$$\delta E = K[\psi(O)_s]^2 R^2 \qquad (2.14)$$

where K is a nuclear constant. Since R is generally different for ground and excited nuclear states, δE will be different for both (Figure 2.8) and:

$$\delta E_e - \delta E_g = K[\psi(O)_s]^2 (R^2_e - R^2_g) \qquad (2.15)$$

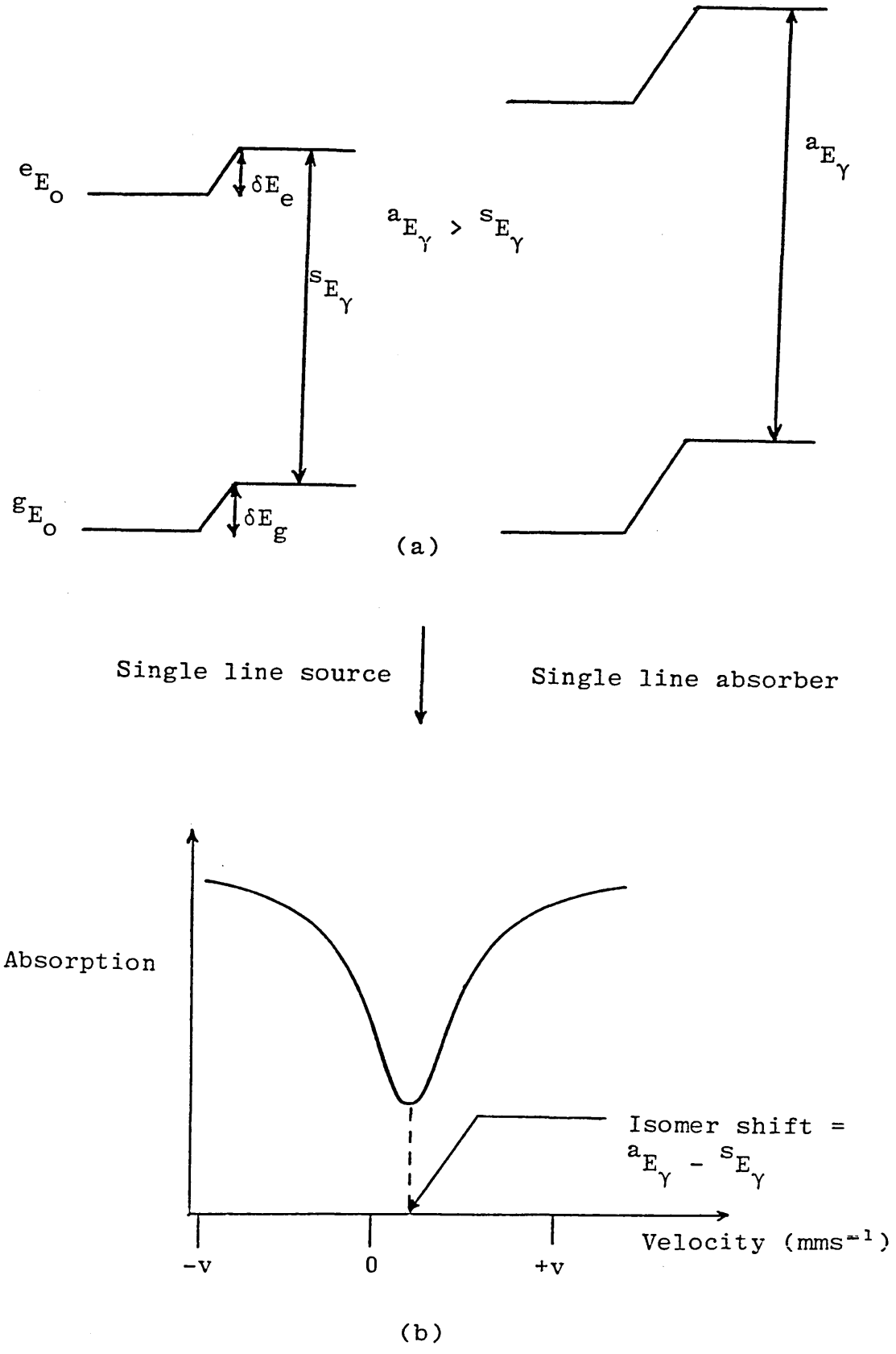

Figure 2.8 : Nuclear Energy Levels and the Isomer Shift
(a) source and absorber nuclear energy levels, (b) resultant Mössbauer spectrum

where subscripts e and g refer to the excited and ground nuclear states respectively. The R values are nuclear constants, but the $[\psi(O)_s]^2$ terms will vary from compound to compound. The above energy difference becomes measurable in the Mössbauer experiment by comparing the nuclear transition energy in the source, ${}^{s}E\gamma$, with that in the absorber, ${}^{a}E\gamma$. The isomer shift is given by the difference in transition energies for source and absorber.

$$I.S. = K(R^2_e - R^2_g)\{[\psi(O)_s]^2_a - [\psi(O)_s]^2_s\} \quad (2.16)$$

Standard sources are usually employed e.g. ^{57}Co-Rh for ^{57}Fe Mössbauer spectroscopy. Since the change in radius $R_e - R_g$ is very small, the isomer shift can then be written in a more familiar form

$$I.S. = 2KR^2 \frac{\delta R}{R} \{[\psi(O)_s]^2_a - c\} \quad (2.17)$$

where: $\delta R = R_e - R_g$ and c is a constant characteristic of the source used. Thus the isomer shift depends on a nuclear factor δR and an extranuclear factor $[\psi(O)_s]^2_a$.

For a given nucleus, δR is a constant, so that the isomer shift is directly proportional to the s-electron density at the nucleus of the absorber. When δR is negative - as for ^{57}Fe - an increase in s-electron density at the absorber nucleus results in a more negative isomer shift. [3]

Although changes in isomer shift are due to variations in s-electron density, differences in isomer shifts are observed on addition or removal of p- or d-electrons which do not themselves interact directly with the nuclear charge density. Shielding by other electrons effectively increases the s-radial functions and decreases the s-electron density at the nucleus i.e. a $3d^6 4s^1$ outer electronic configuration will have a higher s-electron density than $3d^7 4s^1$ because of the penetration of the 3s orbital by the 3d.

2.2.2 The Quadrupole Splitting

The quadrupole splitting arises from the interaction of the nuclear quadrupole moment with the local electric field gradient. Until now it has been assumed that the nucleus is spherical and has uniform charge density. Nuclei with spin 0 or $\frac{1}{2}$ are spherically symmetrical and thus the ground state of ^{57}Fe ($I = \frac{1}{2}$) cannot exhibit a quadrupole interaction. For nuclei with a spin angular momentum greater than $\frac{1}{2}$, the charge density is no longer uniform and the nucleus assumes either a prolate or an oblate shape, resulting in a quadrupole moment. The quadrupole interaction results in a splitting of the nuclear energy levels. For ^{57}Fe, $I_e = {}^3/_2$ and $I_g = {}^1/_2$, the $I_e = {}^3/_2$ level splits into two ($m_I = \pm {}^3/_2 , \pm {}^1/_2$), the $I_g = {}^1/_2$ level remains degenerate. Both the possible transitions are allowed with equal probability and a characteristic two line spectrum is observed. In general, there will be a

combined isomer shift and quadrupole interaction (Figure 2.9). The separation of the peaks is the quadrupole splitting and the centre of the two peaks relative to zero velocity is the isomer shift. For half integral nuclear spins, the quadrupole interaction results in I + ½ levels for spin I.

The quadrupole interaction [3] results in an energy change given by

$$E_Q = \frac{e^2qQ}{4I(2I - 1)} [3m_I^2 - I(I + 1)] (1 + \eta^2/3)^{\frac{1}{2}} \qquad (2.18)$$

where Q = nuclear quadrupole moment

η = asymmetry factor

m_I = magnetic quantum number

eq = maximum value of the field gradient

e = electronic charge

In each case where the degeneracy is removed, the magnitude of the splitting is determined by the interaction of the quadrupole moment with the z component of the electric field gradient (E.F.G.) which is related to the symmetry properties of the crystal. The E.F.G. is found by applying the gradient operator to the three components of the electric field which is itself a vector. The result is a 3 x 3 tensor which can be reduced to three components

$$\frac{\partial^2 V}{\partial x^2}, \frac{\partial^2 V}{\partial y^2}, \frac{\partial^2 V}{\partial z^2} \quad \text{written } V_{xx}, V_{yy}, V_{zz}$$

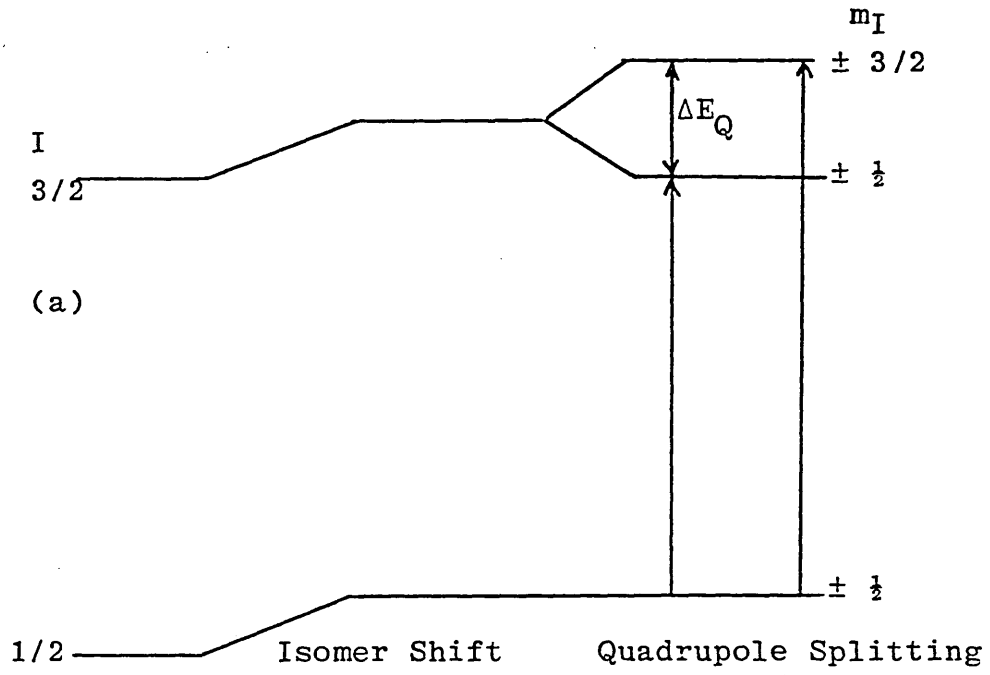

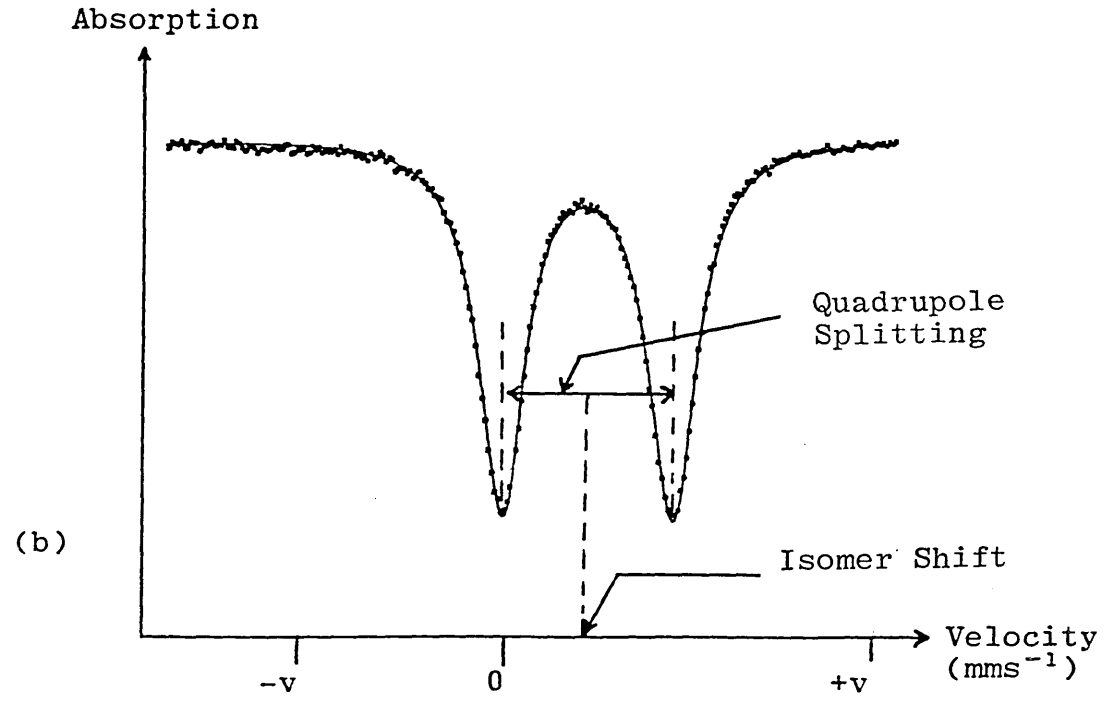

Figure 2.9 : Nuclear Energy Levels and the Quadrupole Splitting - (a) Absorber energy levels : excited level ($I = \frac{3}{2}$) split into two by quadrupole interaction, (b) resultant Mössbauer spectrum

These are not independent and are related by the Laplace equation in a region where the charge density vanishes: $V_{xx} + V_{yy} + V_{zz} = 0$. By convention, the z co-ordinate of the E.F.G. is chosen to coincide with the highest symmetry axis of the molecule or crystal and η is defined as:

$$\eta = \frac{V_{xx} - V_{yy}}{V_{zz}} \qquad (2.19)$$

Thus V_{zz} and η are the only two independent components in equation (2.18). The components are chosen so that $V_{zz} \geq V_{yy} \geq V_{xx}$, thereby $0 \leq \eta \leq 1$. For an axially symmetric field gradient $V_{xx} = V_{yy}$ and so $\eta = 0$, and for cubic or spherical symmetry each $V_{ii} = 0$ and the quadrupole interaction is zero.

The E.F.G. has two sources: firstly, each electron in the atom makes a contribution to a component of the E.F.G. tensor, and if the orbital population is not spherical, the total value of V_{zz} will be non-zero. This is termed the valence contribution (q_{val}). Secondly, there is a contribution from distant ionic charges from associated ligands. This is termed the lattice contribution (q_{lat}). These two contributions are not independent due to shielding,antishielding effects. It is normally assumed, on account of the inverse cubic dependence on distance that q_{val} will be much larger than q_{lat}. [6] To correlate the magnitude of the quadrupole splitting with the geometry and

electronic structure of the compound, a means of computing the relative magnitude of the E.F.G. is needed. The simplest approach to this is the point charge model which has been described by other workers. [7,8,9]

2.2.3 Magnetic Hyperfine Interaction

The magnetic hyperfine splittings arise from the interaction of the nuclear dipole magnetic moment, μ, with the hyperfine field, B, existing at the nucleus. The Hamiltonian representing the interaction is given by:

$$\mathcal{H} = -\mu.B = -g_N\mu_N\ I.B \qquad (2.20)$$

where g_N = nuclear gyromagnetic ratio

μ_N = nuclear magneton

I = nuclear spin angular momentum

The interaction completely removes the degeneracy of the nuclear spin, I, to split each level into (2I + 1) sub-levels. The shifts in the nuclear energy associated with the loss of degeneracy are given by:

$$E_{m_I} = -\mu_N.B_{m_I} \quad (\text{for } m_I = I, I-1, I-2, \ldots -I) \qquad (2.21)$$

$$E_{m_I} = -g_N\mu_N\ B.m_I \qquad (2.22)$$

For the ^{57}Fe nucleus g_N differs in sign for the ground and excited states and the selection rule describing the allowed Mössbauer transitions, $\Delta m = 0, \pm 1$, gives rise to a symmetric six line spectrum (Figure 2.10).

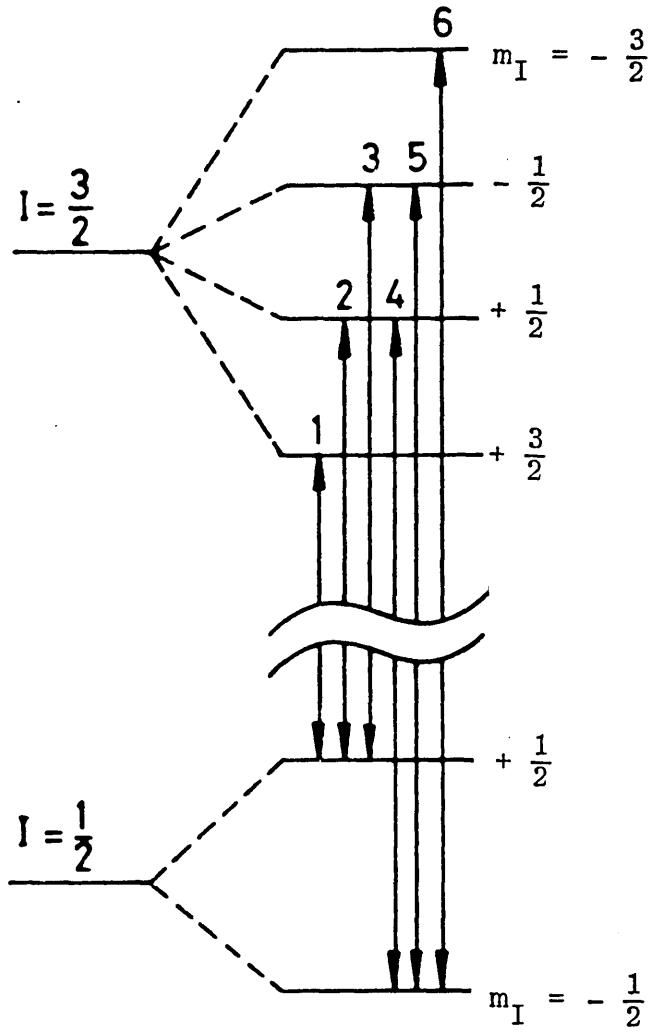

Figure 2.10 : The Nuclear Energy Levels in ^{57}Fe. The magnetic hyperfine interactions occurring in the ^{57}Fe nucleus and the resulting Mössbauer spectrum

The spacings between the line pairs (1,2), (2,3), (4,5), and (5,6) are equal since

for $I = {}^{3}/_{2}$, $E = -g_N\mu_N B.{}^{3}/_{2}$

and for $I = {}^{1}/_{2}$, $E = -g_N\mu_N B.{}^{1}/_{2}$

$\therefore \quad m = I_{3/2} - I_{1/2} = -g_N\mu_N B$

Hence the peaks are equally spaced and this is useful in determining the velocity linearity of the Mössbauer spectrometer using the known splitting of natural iron. The absolute line energies and corresponding Doppler shift velocities have been determined independently by several groups of workers using a number of absolute calibration standards. The determined values of the line positions are used as secondary standards to routinely calibrate the spectrometer.

The line widths of the six peaks are in general equal, but the intensities are different. The line intensities are given by:

$$I_1 = I_6 = 3(1 + \cos^2\theta) \qquad (2.23)$$

$$I_2 = I_5 = 4 \sin^2\theta \qquad (2.24)$$

$$I_3 = I_4 = 1 + \cos^2\theta \qquad (2.25)$$

Where θ is the angle relative to the principal axis of the magnetic field. The above data is taken from the Mössbauer Effect and Data Index, 1975.

In a similar way to the isomer shift and quadrupole splitting, the magnetic hyperfine effect is the product

of a nuclear term which is a constant for a given Mössbauer transition and a magnetic term which can be produced by the electronic structure. The magnetic field at the nucleus can originate in several ways. [10,11,12] A general expression is:

$$H = H_O - DM + {}^4/_3\pi M + H_S + H_L + H_D \qquad (2.26)$$

H_O is the value of the magnetic field at the nucleus generated by an external magnet and is effectively zero away from a large magnet. The next term, -DM, is the demagnetising field and ${}^4/_3\pi M$ is the Lorentz field (the coefficient being strictly applicable to cubic symmetry only) but both are small. H_S, usually referred to as the Fermi contact term, arises as a result of the interaction of the nucleus with an imbalance in the s-electron spin density at the nucleus.

$$H_S = \frac{-16\pi}{3} \mu_B \left\{\Sigma(s\uparrow - s\downarrow)\right\} \qquad (2.27)$$

where $s\uparrow$ and $s\downarrow$ are the s-electron densities at the nucleus with spin up and spin down respectively. Its actual origin may be from intrinsic unpairing of the actual s-electrons, or indirectly as a result of polarisation effects on filled s-orbitals. These may occur if the atom has unpaired electrons in d- or f-orbitals, or if it is chemically bonded to such an atom. The interaction of an unpaired d-electron with the s-electrons of parallel spin will be different to that with the s-electrons of opposite spin. The result is

a slight imbalance of spin density at the nucleus.

If the orbital magnetic moment of the parent atom is non-zero, the term H_L is given by

$$H_L = -2\mu_B \langle r^{-3} \rangle \langle L \rangle$$

or $$H_L = -2\mu_B \langle r^{-3} \rangle (g - 2) \langle S \rangle \qquad (2.28)$$

<L> and <S> are the appropriate expectation values of the orbital and spin angular moments and g is the Landé splitting factor.

The final term in equation 2.26 arises from the dipolar interaction of the nucleus with the spin moment. The terms H_S, H_L and H_D can all be of the order of 10^4 - 10^5 gauss and their sum is usually referred to as the internal magnetic field.

The sign of the internal magnetic field H can be readily determined. Equation 2.26 shows that the application of an external magnetic field H_o alters the effective field at the nucleus tc the sum $H + H_o$. Application of an external field to a magnetically split Mössbauer resonance will result in an observed increase or decrease in the hyperfine field according to whether the applied field is parallel or antiparallel to H. This method was described by Hanna et al. [13] The fields required are large, typically 30-50 kG, and superconducting magnets are used. If there are two or more field directions present, as in antiferromagnetic materials, it may be possible to distinguish the

sublattice resonance lines by the opposite effects of the applied field.

From the above description, it might be assumed that all compounds containing unpaired valence electrons would show a magnetic splitting. However, the Hamiltonian in equation 2.20 contains I and B as a vector product and the observation time scale is of the order of 10^{-8} s. The electronic spins which generate B are subject to changes of direction, known as electronic spin relaxation. In paramagnetic compounds, the spin relaxation is rapid and results in B having a time average of zero and no magnetic splitting is seen. When phenomena such as ferromagnetism or antiferromagnetism are present, the relaxation rates are slower and splitting is observed. There are, however, intermediate conditions where the electronic spins are relaxing on a time scale comparable with that of the Lamor frequency, and these conditions result in complex spectra [14]. For this study the influence of particle size effects on relaxation and hence on the observed Mössbauer spectrum is of importance (Section 2.3).

Because the internal magnetic field of a magnetically ordered material is generally proportional to the magnetisation, its temperature dependence will reflect the latter and follow a Brillouin function approaching zero at the Curie or Néel temperature. In cases where two or more distinct magnetic lattices are present, the

Mössbauer spectrum will reveal the internal field at each individual site, whereas the bulk magnetisation is an average effect. This differentiation is particularly significant for antiferromagnetic compounds where the Mössbauer spectrum can confirm that magnetic ordering is present.

2.2.4 Combined Magnetic and Quadrupole Interactions

In some magnetic materials, there will also exist a non-zero quadrupole interaction. This complicates the interpretation of the spectrum considerably. In general, it is not possible to solve this problem for a general relationship between the magnetic field and the electric field gradient. Only under certain conditions can the system be solved. The special cases are identified from the symmetry of the crystal, the site symmetry and the magnetic properties. The simplest case can be used to illustrate the type of spectrum that will be observed. If we consider an axially symmetric electric field gradient tensor with a symmetry axis parallel to $\underline{H}$, a small quadrupole interaction can be treated as a perturbation to the magnetic interaction. The energies are given by:

$$E = -g\mu_N H m_I + (-1)^{|m_I| + \frac{1}{2}} \text{ eq } Q/4 \qquad (2.29)$$

and the level splitting is illustrated for a $^3/_2 \rightarrow {}^1/_2$ decay in Figure 2.11. In this simple example, the two energy contributions are added, the magnitude of the quadrupole interaction is equal for each magnetic level, ε, but some levels are shifted up and others are

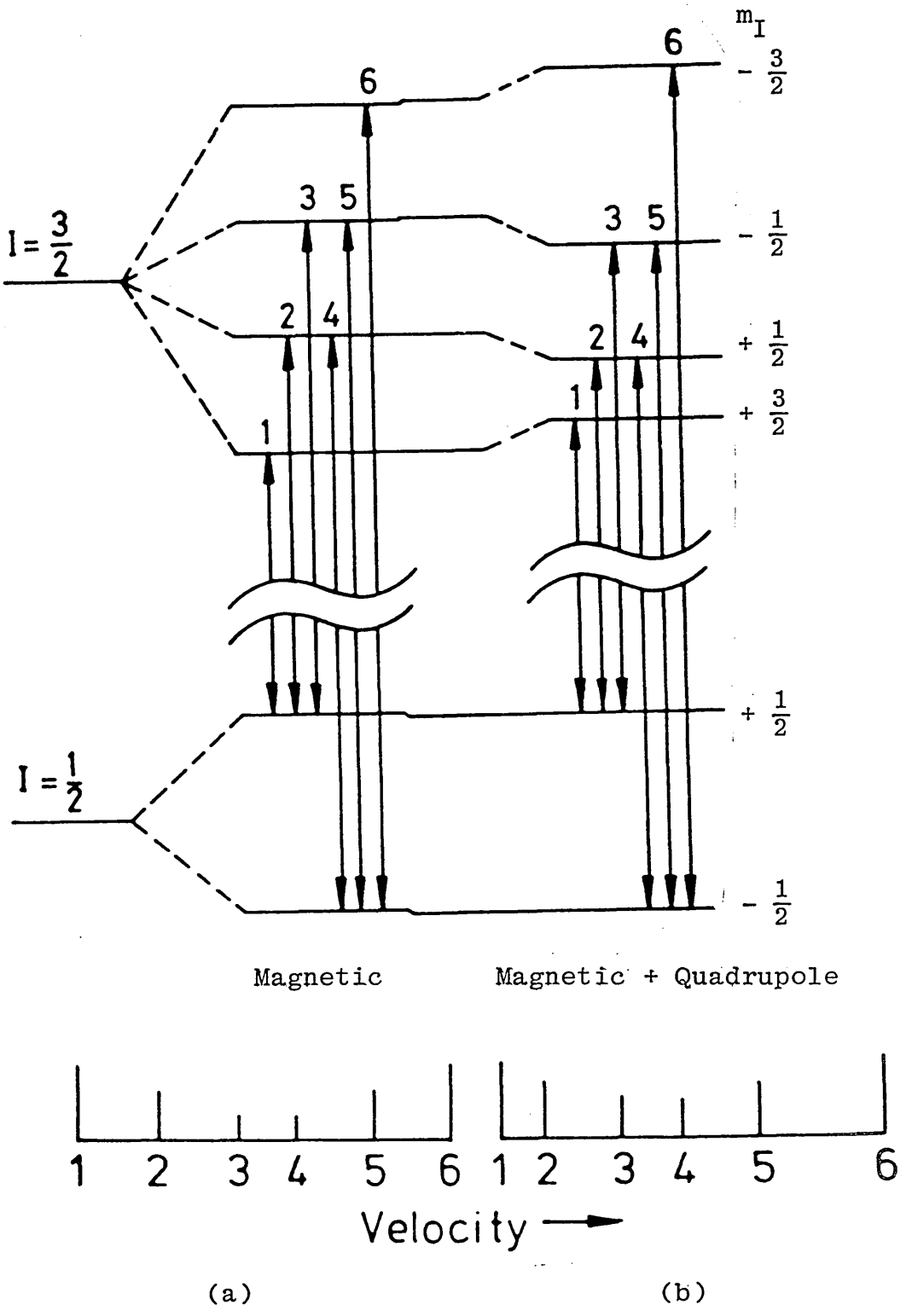

Figure 2.11 (a) and (b) The Nuclear Energy Levels in ^{57}Fe. (a) The pure magnetic interaction. (b) The magnetic interaction combined with a small quadrupole perturbation

shifted down.

2.3 Particle Size Effects

Microcrystals are present in many technologically important materials eg catalysts, magnetic tape, ceramics, corrosion products, pigments in paints, building materials. An understanding of particle size effects is therefore important in studies of many different types of materials. Several reviews of Mössbauer studies of magnetic microcrystals have recently been published. [15,16,17]

Figure 2.12 is a schematic illustration of the dependence of the observed hyperfine field on the crystal dimensions of magnetic microcrystals.

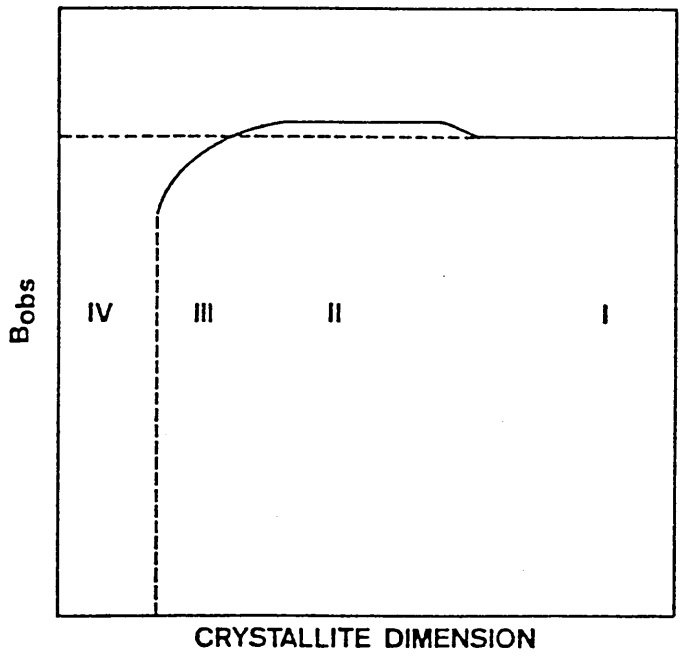

Figure 2.12 : Schematic Illustration of the Dependence of the Observed Magnetic Hyperfine Field on the Crystal Dimension of Magnetic Microcrystals

Particles with dimensions larger than 50-100 nm (Region 1) essentially exhibit the bulk magnetic behaviour.

For small particles of a magnetically ordered material, a critical size exists below which a particle consists of a single domain in a zero applied field. This is because the decrease in magnetic energy obtained by splitting the single domain into smaller domains is less than the energy increase created by the formation of domain walls. When the crystal dimensions are below 20-50 nm, the particles are single domain particles. The demagnetising field will then contribute to the total magnetic field at the nucleus which is given by:

$$\vec{B}_{obs} = \vec{B}_h + \vec{B}_L + \vec{B}_D$$

where $\vec{B}_h$ is the field due to the electrons surrounding the nucleus, $\vec{B}_L$ is the Lorentz field due to the neighbouring atoms, and $\vec{B}_D$ is the demagnetising field. As an example, we consider a spherical particle of metallic iron at room temperature. In this case $\vec{B}_h$ = - 337 kG and $\vec{B}_L$ = +7 kG. These two terms give the hyperfine field $\vec{B}_{obs}$ = -330 kG in multi-domain particles. (The domains are arranged such that the demagnetising field is negligible.) In spherical single domain particles, $\vec{B}_D$ = -7 kG. The total magnetic hyperfine splitting is therefore $\vec{B}_{obs}$ = -337 kG, i.e. the magnetic hyperfine splitting in a single domain particle is increased relative to that of a

multi-domain particle [15,16]. This is represented by region 2 of Figure 2.12.

In the absence of an applied magnetic field, the magnetisation direction of a large magnetically ordered crystal is along an easy direction. However, the anisotropy energy decreases when the particle size decreases, the thermal energy may become comparable to the anisotropy energy of a small particle ($\lesssim$ 10 nm), even at temperatures below room temperature. The magnetisation is then no longer fixed to an easy direction but fluctuates in a random way. Essentially these fluctuations can be divided into two categories.

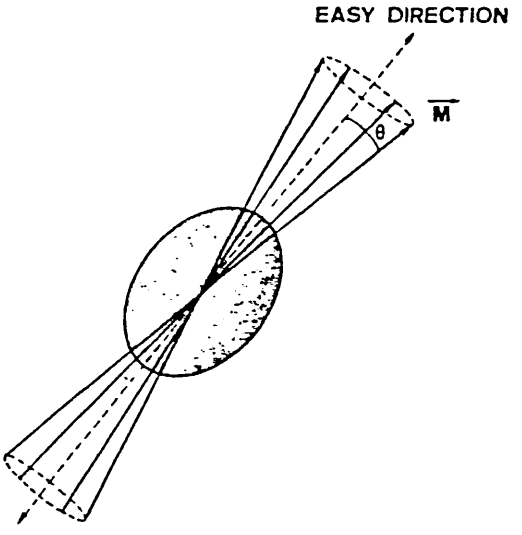

Figure 2.13 : Schematic Illustration of Collective Magnetic Excitations in a Microcrystal

(i) Small fluctuations around an easy direction (Figure 2.13) are called collective magnetic excitations and are responsible for the broad non-Lorentzian line shapes often observed. (Region 3 of Figure 2.12)

(ii) Superparamagnetic relaxation when the magnetisation direction fluctuates among the various easy directions. When the super-paramagnetic relaxation time is short compared with the time scale of the experimental method being used to study the magnetic properties, the sample resembles a paramagnet.

These large fluctuations among the various easy directions lead to the collapse of the magnetic spectrum. (Region 4 of Figure 2.12)

The different behaviour of a bulk sample and a microcrystalline sample are summarised by Figure 2.14.

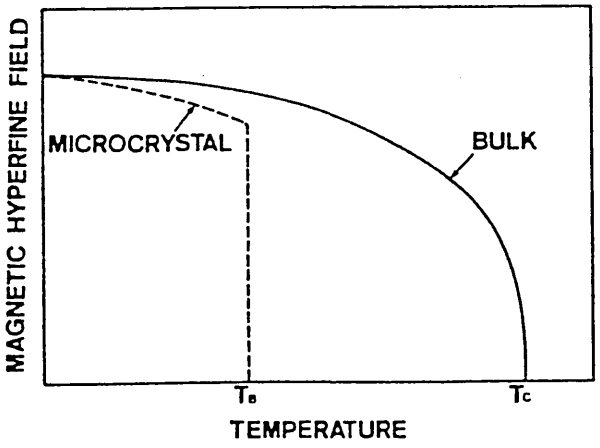

Figure 2.14 : Magnetic Behaviour of Bulk and Micro-crystalline samples

The blocking temperature, T_B, is defined as the temperature below which the particles behave as magnctically ordered crystals. Above the blocking temperature, the magnetic hyperfine splitting collapses.

In practice, a sample of microcrystals will exhibit a particle size distribution. Experimental spectra therefore may vary from completely ordered magnetic spectrum, to one typical of a paramagnetic material, and very often consist of a superposition of a six line component due to the larger particles and a single line or doublet due to smaller particles. The particles with intermediate relaxation times yield very broad components of low intensity which are often very difficult to interpret. Figures 2.15 and 2.16 illustrate some of the complexities of typical Mössbauer spectra of microcrystals.

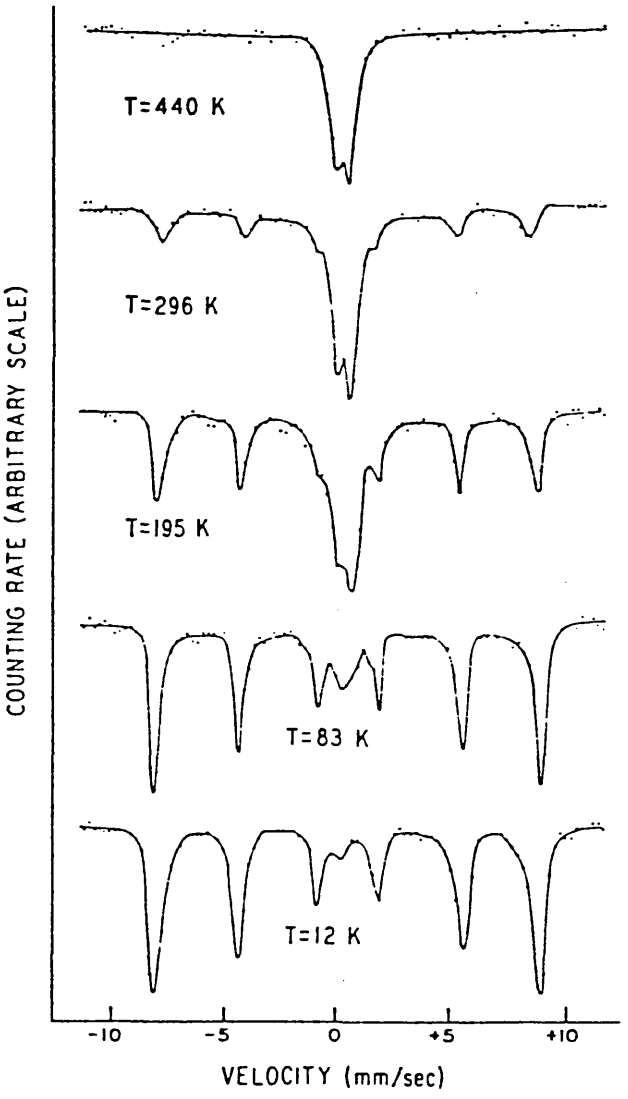

Figure 2.15 : Mössbauer Spectra of Microcrystals of Fe_2O_3 with an Average Diameter of 13.5 nm at Various Temperatures

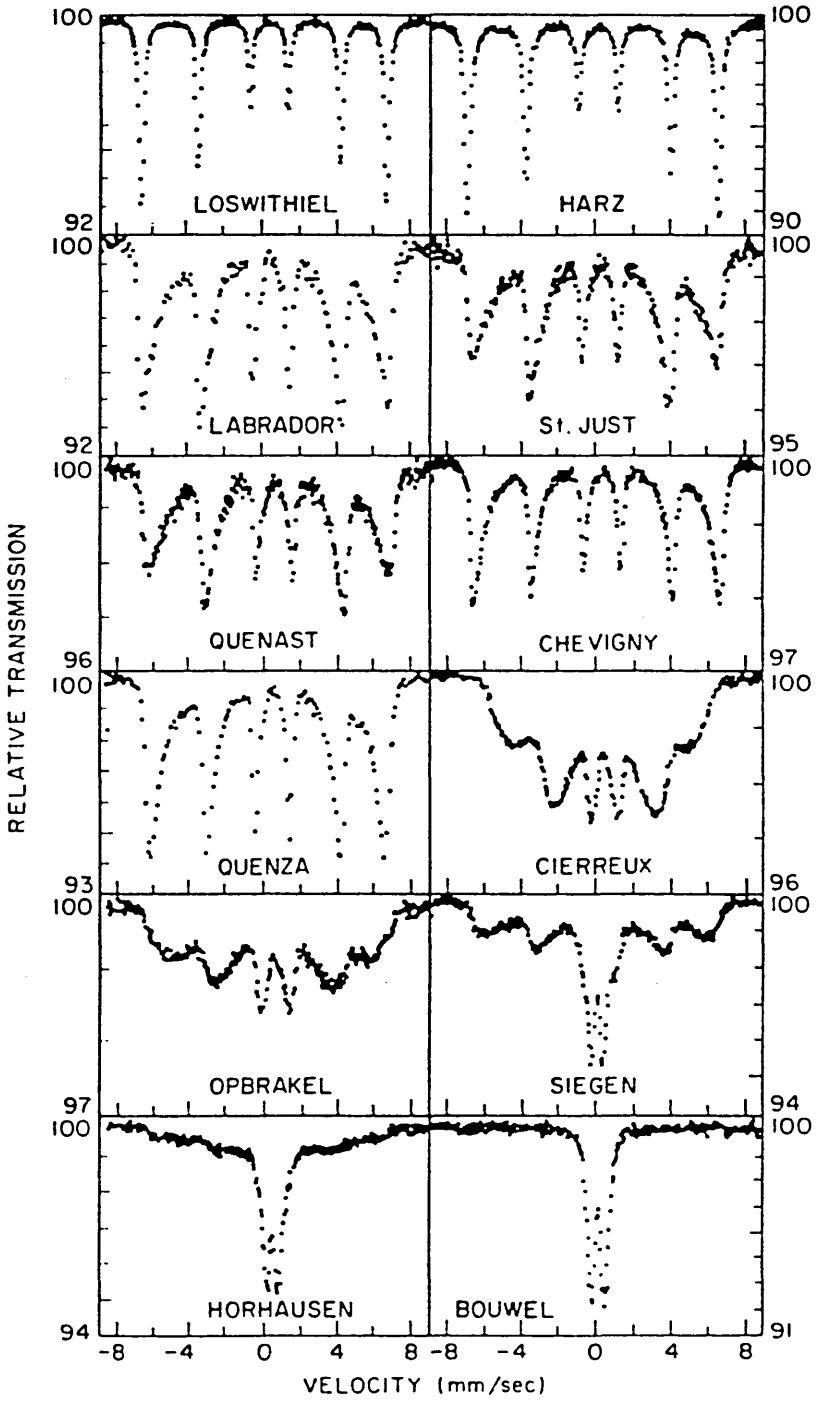

Figure 2.16 : Mössbauer Spectra Obtained at Room Temperature of some Naturally Occurring Geothite (α-Fe-OOH) Samples. The different spectra shapes are due to different particle size distributions

REFERENCES

1. R.L. Mössbauer, Z. Physik, 151, p 124, 1958.

2. G. Breit, E. Wigner, Phys. Rev., 49, p 519, 1936.

3. N.N. Greenwood, T.C. Gibb, "Mössbauer Spectroscopy", Chapman and Hall, London, 1971.

4. H. Frauenfilder, "The Mössbauer Effect", W.A. Benjamin Inc., New York, 1962.

5. W.E. Lamb, Phys. Rev., 55, p 190, 1939.

6. M. Cordey Hays, "Chemical Applications of Mössbauer Spectroscopy", Edited by V.I. Goldanskii and R.H. Herber, Academic Press, New York and London, 1968.

7. B.W. Fitzsimmons, N.J. Seeley, A.W. Smith, J. Chem. Soc., A, p 143, 1969.

8. R.L. Collins, J.C. Travis, "Mössbauer Effect Methodology", Edited by I.J. Gruverman, Plenum Press, New York, 1967.

9. R.V. Parish, R.H. Platt, Inorg. Chim. Acta, 4, p 65, 1970.

10. W. Marshall, C.E. Johnson, J. Phys. Radium, 23, p 733, 1962.

11. C.E. Johnson, M.S. Ridout, T.E. Cranshaw, Proc. Phys. Soc., 81, p 1079, 1963.

12. R.E. Watson, A.J. Freeman, Phys. Rev., 123, p 2027, 1961.

13. S.S. Hanna, J. Heberle, G.J. Perlow, R.S. Preston, D.H. Vincent, Phys. Rev. Letts., 4, p 513, 1960.

14. Mössbauer Spectroscopy Applied to Inorganic Chemistry, Volume 1, p 195, Edited by Gary J. Long, Plenum Press, New York, 1984.

15. S. Mørup, J.A. Dumensic, H. Topsøe, in: Applications of Mössbauer Spectroscopy, Vol II, Edited by R.L. Cohen, Academic Press, New York, 1980.

16. S. Mørup, H. Topsøe, B.S. Clausen, Phys. Scripta., 25, p 713, 1982.

17. A.H. Morrish, K. Haneda, J. Magn. Magn. Mats, 35, p 105, 1983.

CHAPTER 3 : EXPERIMENTAL TECHNIQUES

3.1 Characteristics of a Useful Mössbauer Isotope

3.2 The Mössbauer Source

3.3 The Absorbers

3.4 Detectors

3.5 Instrumentation

3.6 Variable Temperature Facilities

3.7 Computer Fitting of Mössbauer Spectra

References

A Mössbauer experiment essentially measures the resonant absorption in a sample as a function of Doppler energy which is equivalent to measuring the count rate as a function of velocity as previously demonstrated.

3.1 Characteristics of a Useful Mössbauer Isotope

The vast majority of Mössbauer work has involved the isotopes ^{57}Fe and ^{119}Sn but there are more than forty elements which show the effect. (Figure 3.1)

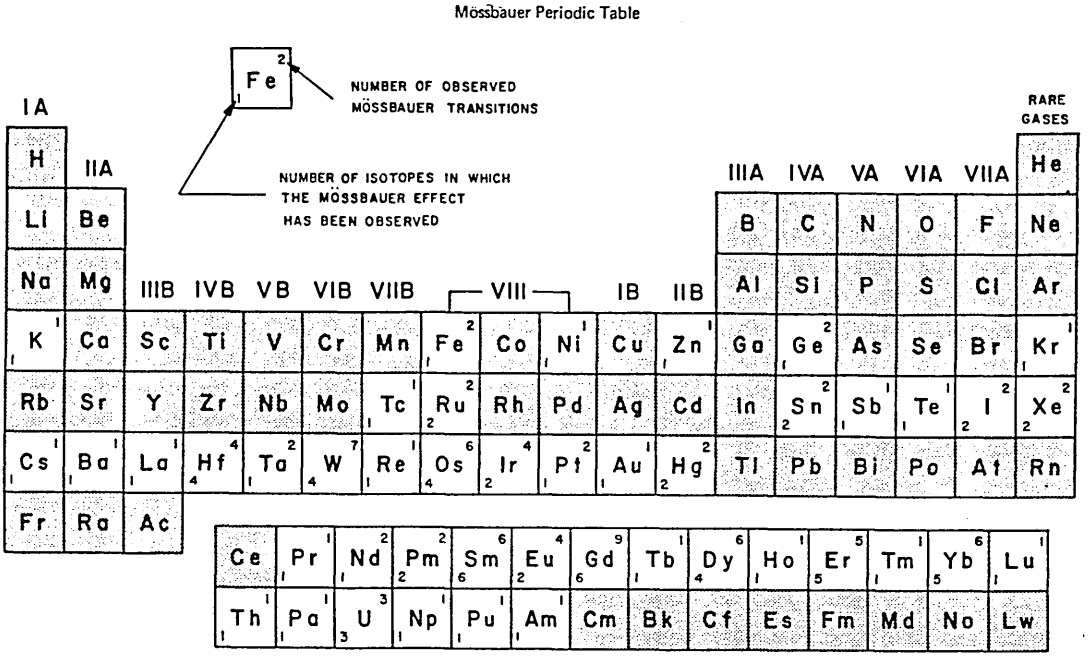

Figure 3.1 : The Mössbauer Periodic Table

The important criteria which make a particular isotope useful for investigation using the Mössbauer technique are listed below:

(i) The source must emit a suitable low energy γ-ray, typically less than 150 keV, which ensures an acceptable recoil free fraction.

(ii) The Mössbauer γ-ray must be sufficiently well resolved from associated radiation, this enables background levels to be minimised.

(iii) The half life of the parent isotope must be convenient for practical experiments. ^{57}Co has an ideal half life of 270 days. In comparison, the parent nuclei for Nickel Mössbauer spectroscopy are ^{61}Co and ^{61}Cu which have half lives of 1.65 hours and 3.41 hours respectively which are far too short for routine experiments.

(iv) The magnitude of the Mössbauer effect which is proportional to the area under the absorption curve. In general, for a 'thin' Lorentzian absorption line, the area is given by

$$A = \tfrac{1}{2}\pi . f_a . f_S . \sigma_0 . n . X . \beta \qquad (3.1)$$

where f_a = absorber recoilless fraction

f_S = source recoilless fraction

σ_0 = isotope cross-section

n = isotope natural abundance

X = absorber thickness

β = 1/no. of absorption lines.

Only isotopes which have a significant natural abundance, cross-section and recoil-free fraction will give a useful Mössbauer effect.

(v) The experimental line widths must be close to the natural line widths, and the line positions must be sufficiently sensitive to allow the hyperfine interactions to be resolved.

3.2 The Mössbauer Source

The decay of ^{57}Co emits a γ photon of energy 14.4 keV ($t_{\frac{1}{2}}$ = 270 days) which has a natural line width of 0.1940 mms^{-1}. [1] The source used during this work was a 25 mCi ^{57}Co isotope in a Rhodium matrix supplied by Amersham International Ltd., having a single line with full width at half height of 0.22 mms^{-1} and a recoil free fraction of 0.75 at room temperature. The isomer shift relative to α-Fe is +0.11 mms^{-1}. For the purpose of calibration and linearity checks, the magnetic hyperfine splitting of the ground and first excited state of ^{57}Fe was used. The decay scheme for ^{57}Co is given in Figure 3.2. The nuclear parameters for ^{57}Fe are given in Table 3.1

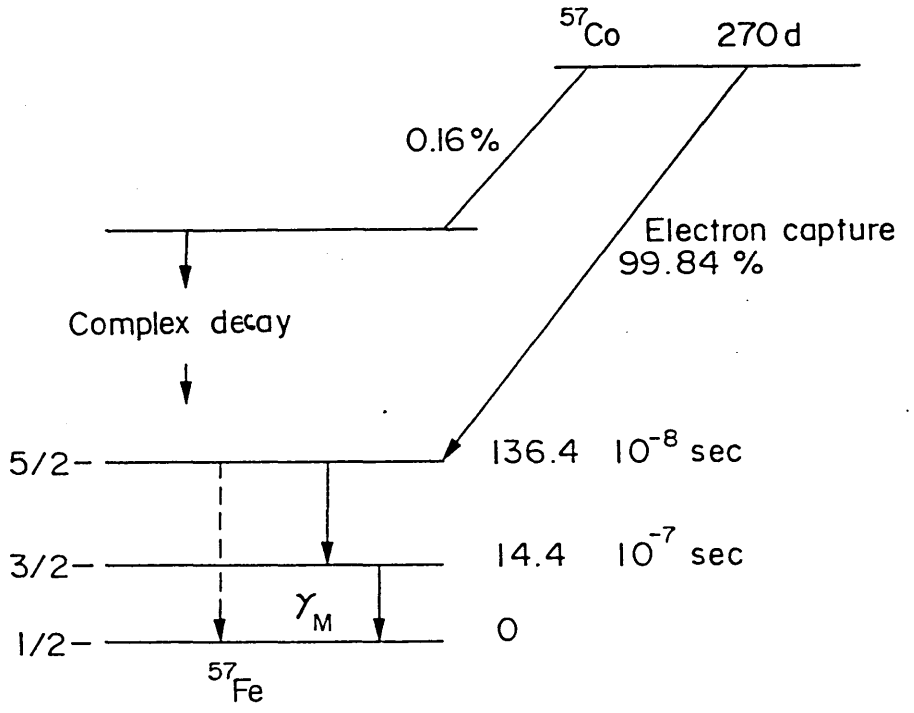

Figure 3.2 : Decay Scheme for ^{57}Co

E = 14.4 keV	$\Gamma = 4.665 \times 10^{-9}$ eV
$\mu_g = +0.09024$ nm	$\omega_0 = 0.1940$ mms^{-1}
$\mu_e = -0.15460$ nm	Isotopic Abundance 2.14%
$\frac{\mu_e}{\mu_g} = -1.71321$	Symmetrical line posns. for iron foil
$\frac{g_e}{g_g} = -0.57106$	1,6 ± 5.312 mms^{-1}
	2,5 ± 3.076 mms^{-1}
	3,4 ± 0.840 mms^{-1}

nm = nuclear magneton (nm = 5.0504×10^{-27} J T^{-1})

Table 3.1 : Mössbauer Nuclear Parameters and Calibration Data for ^{57}Fe

3.3 The Absorbers

3.3.1 Absorber Thickness

It was shown earlier (Section 2.1.2) that the line width of the emitted γ-ray is related to the half-life of the excited nuclear state. In practice, the observed line width at half height is influenced by the absorber thickness. As the thickness of the absorber increases, the line shape begins to deviate from the Lorentzian shape and saturation effects occur.

A quantitative appreciation of the effect of absorber thickness is gained by considering the area under the absorption curve. Williams and Brooks [2] showed that, in general, the area under the absorption curve A(t) is related to the Mössbauer thickness (t) by the expression:

$$A(t) \alpha \tfrac{1}{2}t \exp(-\tfrac{1}{2}t).[I_0(\tfrac{1}{2}t) + I_1(\tfrac{1}{2}t)] \qquad (3.2)$$

I_0 and I_1 are zero and first order Bessel functions. The above expression can be reduced to a first approximation to:

$$A(t) \alpha f_s t(1 - 0.25t + 0.0625\ t^2 + ...) \qquad (3.3)$$

for values of $t < 5$. (f_s = recoilless fraction in the source). Where t is large ($\gtrsim 10$), equation 3.2 must apply.

The absorber thickness is calculated using the equation

$$t = \beta.n'.f_a.\sigma_0.X \qquad (3.4)$$

where β = 1/number of absorption lines

n' = number of resonant nuclei cm^{-3}

f_a = recoil free fraction of the absorber

σ_0 = resonant cross section

X = actual absorber thickness.

In practice, evaluation of the optimum absorber thickness using (3.2) is limited as f_a is unknown for many absorbers. Particle size also has a major influence on observed lineshapes as described in Section 2.3.

3.3.2 Absorbers for Transmission Mössbauer Spectroscopy

In general, absorbers can be thin metal foils, compacted powders, mixtures with inert solid diluents, mixtures with inert greases, frozen liquids, or frozen solutions. The only limitation is on the material used for the window of the sample container, as this must be free of the resonant isotope and have a low attenuation coefficient for the γ-ray being studied. For this study, perspex sample holders were used to record room temperature spectra. For variable temperature work (Section 3.6), graphite sample holders were used to eliminate temperature gradients across the sample.

3.3.3 Absorbers (Fluorescer) for Backscatter Mössbauer Spectroscopy

In backscatter Mössbauer spectroscopy, it is fluorescent radiation which is detected and consequently one should refer to fluorescers rather than absorbers when using this geometry. Internal conversion (Section 3.4.2) leads

to the emission of conversion electrons and conversion X-rays [3,4] either of which may be preferentially detected by choice of the appropriate detector flow gases. The very limited escape depth of the conversion electrons requires the surface under investigation to be scrupulously clean. For backscatter Mössbauer spectroscopy, the sample must normally be mounted inside the detector. Typically, samples have been 2 cm x 2 cm x 0.1 cm tablets of mild steel. For one aspect of this work, isotopic enrichment in ^{57}Fe at the surface was required. This is described in more detail in Section 5.2.

3.4 Detectors

The detection system employed consisted of a proportional counter, a pre-amplifier and a high count-rate amplifier.

3.4.1 Detector for Transmission Spectra

Several types of detector are commonly used, notably sodium iodide scintillators, solid-state silicon or germanium detectors and gas-filled proportional counters. The 14.4 keV Mössbauer transition in iron is best observed using a proportional counter to detect the γ-rays. The low energy γ-rays are totally absorbed by the gas-filled counter. This has better resolution and signal/noise ratio than the scintillation counter, the efficiency of which deteriorates at low energies on account of the thickness of the NaI(Tl) crystal employed. (The scintillation counter is preferred for the study of tin

compounds using the 23.8 keV γ-ray Mössbauer transition). The proportional counter used contains an argon-5% methane mixture providing optimum conditions for the low energy γ-ray. The operating voltage was -2.8 keV.

3.4.2 Detectors for Backscatter Spectra

Backscatter spectra are obtained by detecting the decay products of the de-excitation of nuclei in the specimen which have been resonantly excited by the source radiation. The emitted radiation may be X-rays, conversion electrons or Auger electrons, and backscatter detectors are designed to be sensitive to these radiations. Table 3.2 gives the proportion of X-rays and conversion or Auger electrons emitted following resonance absorption of the 14.4 keV γ-ray in iron.

	Energy (keV)	Number (per 100) absorption events	Approximate maximum range in typical solids
^{57}Fe			
γ photons	14.4	9	
K X-rays	6.3	27	10 μm
K conversion electrons	7.3	81	250 nm
L conversion electrons	13.6	9	900 nm
M conversion electrons	14.3	1	
KLL Auger electrons	5.4	63	
LMM Auger electrons	0.53		

Table 3.2 : Summary of Major Events During the Decay of I = 3/2 Excited-Spin States of ^{57}Fe

Figure 3.3 is a schematic representation of the internal conversion process.

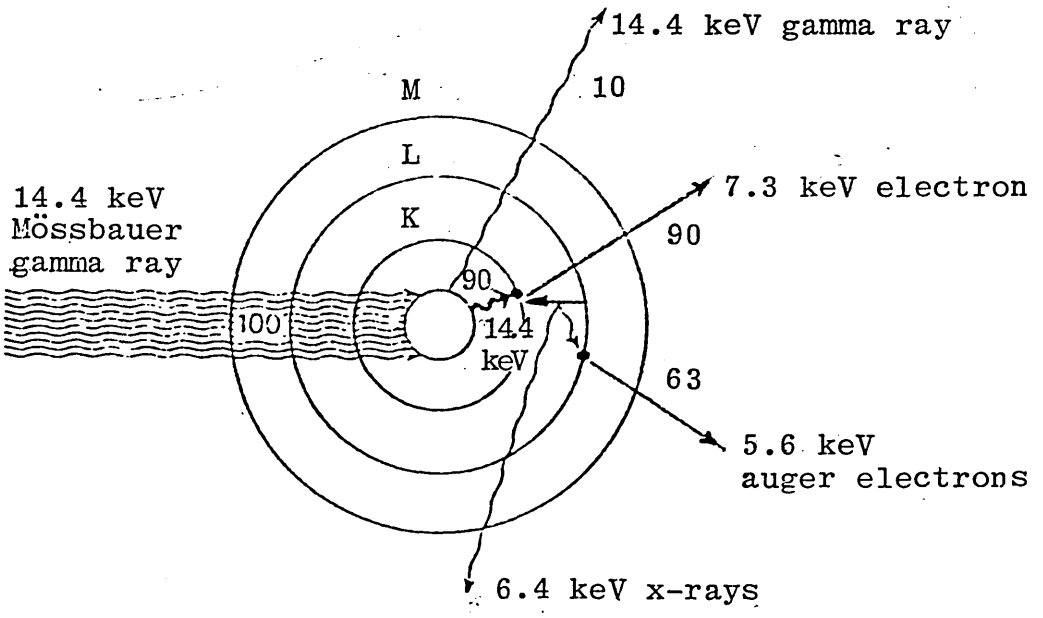

Figure 3.3 Internal Conversion Processes for ^{57}Fe

The range of X-rays and conversion electrons are widely different, typically 10 μm and 0.01 μm respectively in solid materials. Such limited escape depths require the sample to be mounted inside the detector. The arrangement of apparatus for backscatter spectroscopy is illustrated in Figure 3.4. The γ-rays from the source pass through a thin window, cross the counter, and fall upon the specimen. Backscattered radiation is then detected in the counter, the crucial distinction between electron and X-ray detection is the gas filling. A filling of Argon with 5% methane at atmospheric

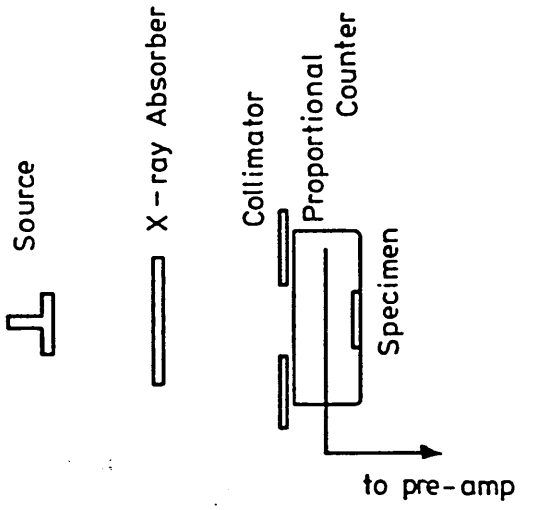

Counter filled with Ar 5% CH_4, X-rays

He 5% CH_4, electrons

Figure 3.4 : Layout of Apparatus for Backscatter Mössbauer Spectrometry

pressure will absorb most of the X-rays producing a 6 keV photo-electron. A filling of helium with 5% methane has a very low efficiency for X-rays or γ-rays but is easily able to absorb low energy conversion electrons by ionisation. The ionisation electrons are collected by the positively charged wire and gas amplification occurs in the normal way. The pulse produced by the amplifier is thus closely proportional to the energy lost by the electron in the gas.

3.4.3 X-ray Detection

The X-rays of interest from the specimen have the same energy as X-rays emitted by the source, and observation of the source X-rays makes setting the window very simple. The source X-rays are filtered out using a thin aluminium

foil when recording a spectrum.

3.4.4 Electron Detection

The electron detector may be set up as follows. A fluorescer of the same composition as the source, eg: a foil of $Rh^{57}Fe$ for a $Rh^{57}Co$ source is placed in the specimen position. The ^{57}Fe concentration is kept below a few per cent to avoid magnetic splitting or broadening of the line [5]. When stationary, the source is resonant with the fluorescer and conversion or Auger electrons are produced with a background of electrons mainly produced by the 122 keV radiation. If the source is then vibrated, the resonant processes are removed, but electrons produced by other processes remain. An energy window is now easily set for the conversion and Auger electrons.

The energy loss of electrons, and the possibility of obtaining spectra related to particular depths in the specimen has been the subject of a great deal of work [6-11]. It is sufficient to remark here that if two windows are set, one on the highest energy part of the spectrum, and one on the lowest, the spectrum recorded by the low-energy window samples a layer deeper in the specimen than the high energy window.

Gas flow proportional counters described above suffer the disadvantage that it is not easy to change the temperature. Low temperature experiments are not possible because the gases will condense. Ways of using channeltrons or other

electron detectors in vacuo which remove this obstacle are described elsewhere [12-14].

3.5 Instrumentation

A Mössbauer spectrum is a record of the rate of interactions occurring in a specimen as a function of energy. The occurrence of the interactions may be detected by the absorption of γ rays from the beam, in which case we have a transmission spectrum, or by the detection of the decay products, such as γ-rays, X-rays or conversion electrons, of the excited nucleus in which case we have a backscatter spectrum. A Mössbauer spectrometer is an instrument for obtaining the spectra. A block diagram of the system used is shown in Figure 3.5. It consists basically of a drive mechanism to impart a controlled Doppler velocity to the radioactive source, a detector with associated amplifying and data collection equipment, and a data storage device which is often a multichannel analyser.

3.5.1 Mössbauer Drive System and Multichannel Analyser

Throughout this work, a Canberra Industries Series 30 1024 channel multichannel analyser (MCA) was used. The two available modes of operation were: either the time mode, in which the analyser operates as a multichannel scaler (MCS); or the pulse height analyser (PHA) mode. In the time mode, the analyser stores the total count information in each channel through a preset time interval of 200 μs. At the end of the time interval, the address

is advanced to the next sequential channel. A dead time, estimated at 10% of the total scan time, is incurred during this channel advance. This operating cycle is repeated over 512 channels and then recycled.

When operating in the PHA mode, a single channel analyser is used to set a window for the radiation of interest.

The Elscint Function Generator, Model MFG-N-5, and Transducer Driving Unit, Model MDF-N-5, are operated in conjunction with the Elscint Linear Velocity Transducer, Model NVT4, to form the velocity servo system. This contains a wave function generator providing a sawtooth wave which operates on the Most Significant Bit (MSB) of the MCA. The transducer driving unit imparts a linear motion to the moving rod of the transducer.

Using 512 channels of the MCA, a square wave is extracted from the MSB of the MCA such that its leading edges are at channels 256 and 512. This is integrated to obtain the signal representing the velocity waveform (Figure 3.6). The transducer produces a voltage proportional to the velocity of the vibrator drive shaft. The servo amplifier compares this signal to the reference triangular waveform and applies corrections to the drive coil to minimise any differences. The amplitude of the triangular waveform determines the velocity range of the vibrator. While the vibrator is continuously sweeping over a range of velocities, the MCA is sweeping through 512 channels. The two sweeps are automatically synchronised and counts

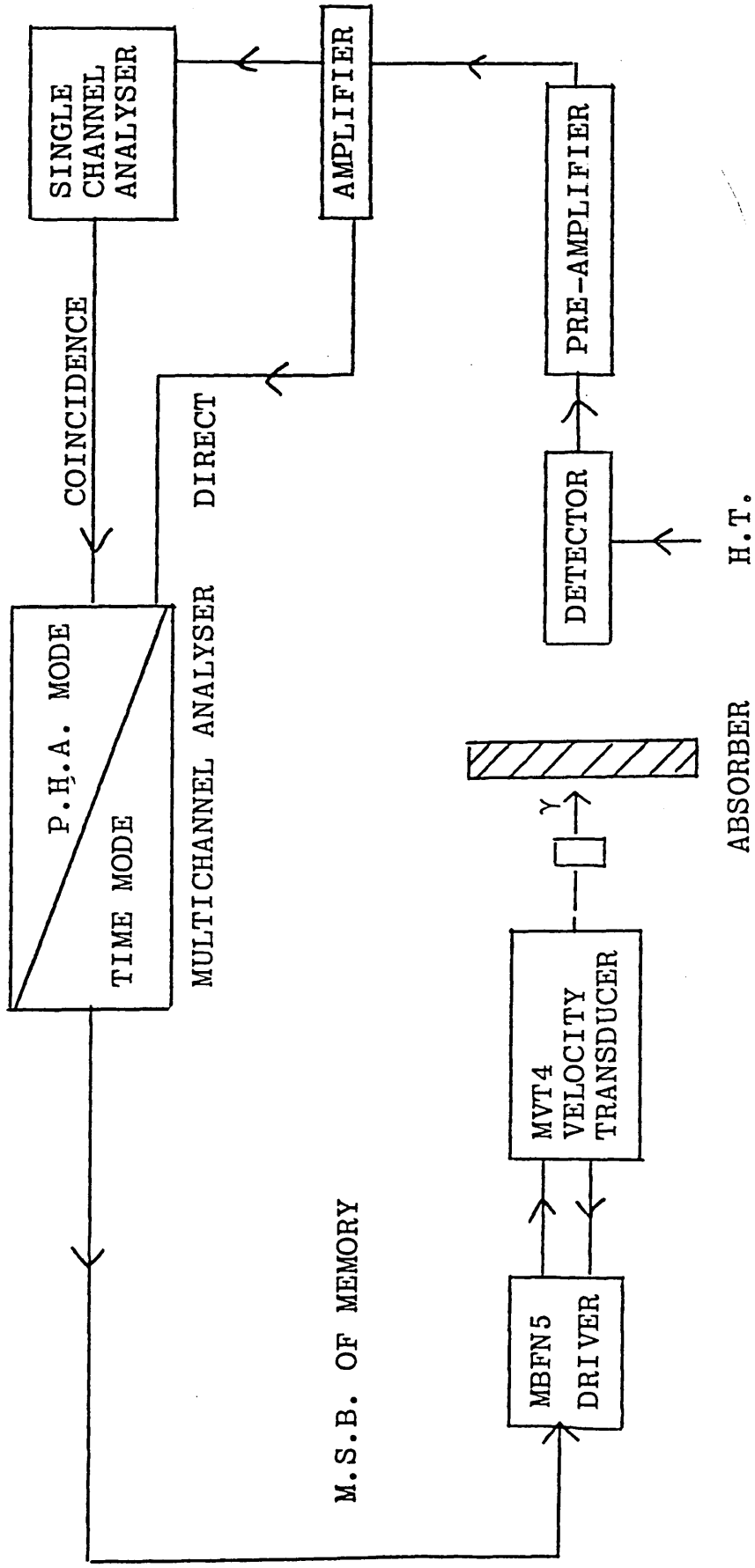

Figure 3.5 : Schematic of the Mössbauer System

corresponding to a particular velocity are fed to the same channel in the MCA. Using the above symmetric waveform, a mirror image of the spectrum is obtained since, by nature of the waveform, the velocity of the source will change from positive to negative and from negative to positive during a complete cycle.

This type of electromechanical drive has excellent long-term stability and synchronisation is ensured in a very

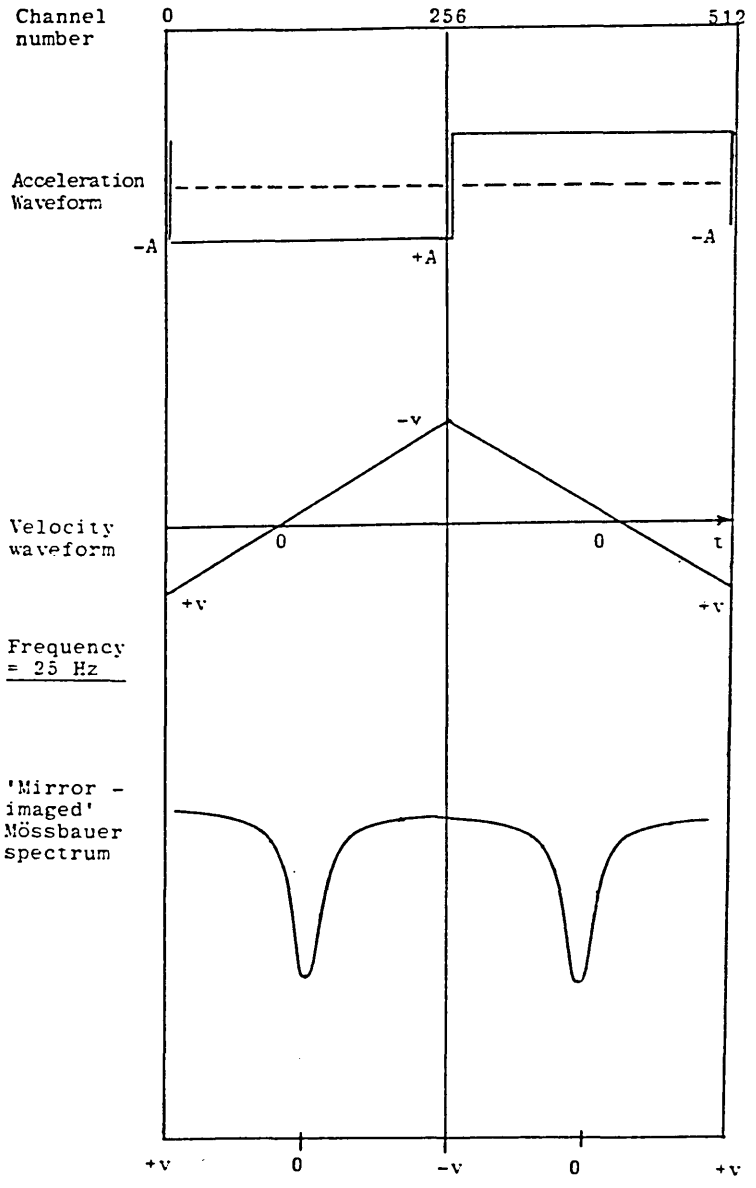

Figure 3.6 : The Mössbauer Spectrum and Related Waveforms

simple manner. The velocity range required (typically ± 12 mms^{-1} for ^{57}Fe) can easily be obtained with this device, and the linearity of such systems is typically better than 1%. The duplicate spectra obtained are useful because they can easily be folded over and computer averaged, which eliminates any curvature of the baseline due to the slightly different count rates observed at the extremes of the source displacement, and serves as a useful check on the linearity of the system. Any lack of linearity in the scan will in general destroy the mirror symmetry and any spurious absorptions due to electronic faults can be easily identified.

3.6 Variable Temperature Facilities

Many early spectra proved difficult to interpret because the corrosion products formed on iron may be a mixture of phases of iron oxyhydroxides which give doublets at room temperature and/or relaxation, particle size effects described earlier (Sections 2.2.3 and 2.3 respectively) may be influencing the observed spectra. To resolve these problems spectra must be recorded at temperatures well below the magnetic ordering temperature. This has now become possible using an Air Products Cryogenic Refrigeration System (Figure 3.7). The CS-202 Expander Module used in conjunction with the DMX-20 interface is designed for applications in which the sample area must be isolated from all vibrations (ie to observe the Mössbauer effect).

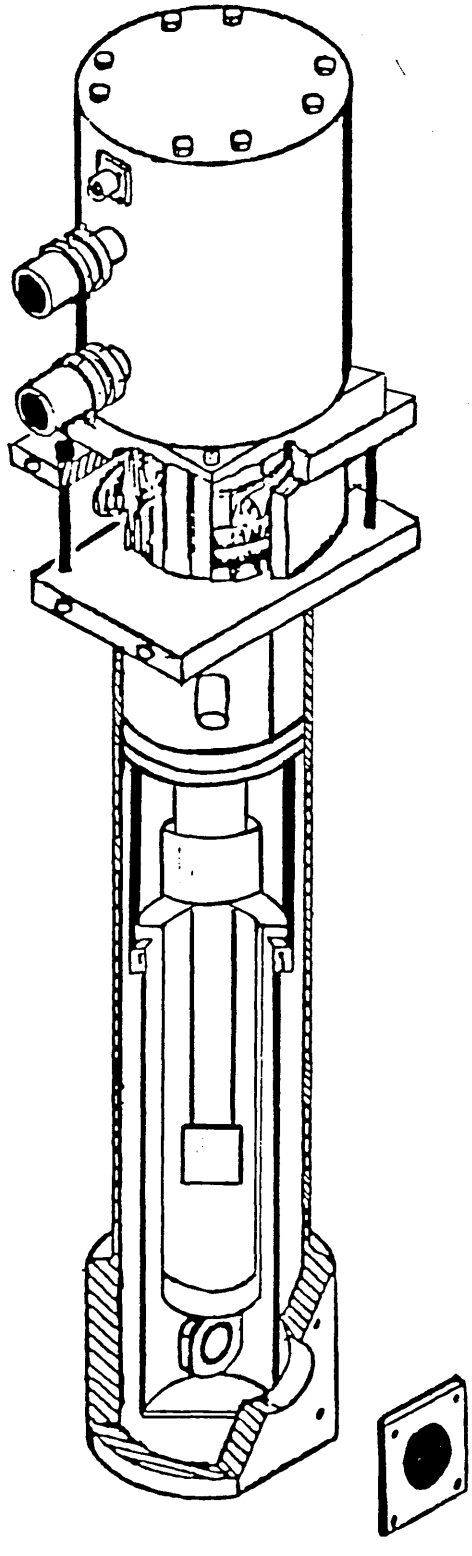

Figure 3.7 : Air Products Cryogenic Refrigerator

The CS-202 Expander Module is a two-stage cryogenic refrigerator using gaseous helium as the refrigerant. Power to operate the expander module is drawn from and controlled by a compressor module which also supplies the required gaseous helium. Figure 3.8 is a simplified diagram identifying the key elements by which the expander module produces refrigeration.

During operation, the compressor module continuously draws low pressure helium from the system return line; compresses, cools and cleans it; then delivers it at high pressure through the system supply line to the refrigeration module. Figure 3.9 illustrates the gas flow cycle.
Gas leaving the compressor contains heat and compressor lubricant which must be removed.

From the compressor, the hot gas and entrained oil flows through one circuit of a three circuit heat exchanger. After being cooled, it returns to the compressor to cool the motor windings and to lose some of the suspended oil. It is then recooled by making a second circuit through the oil separator and the adsorber for oil and moisture removal. From the adsorber, the high pressure gas is piped to the expander.

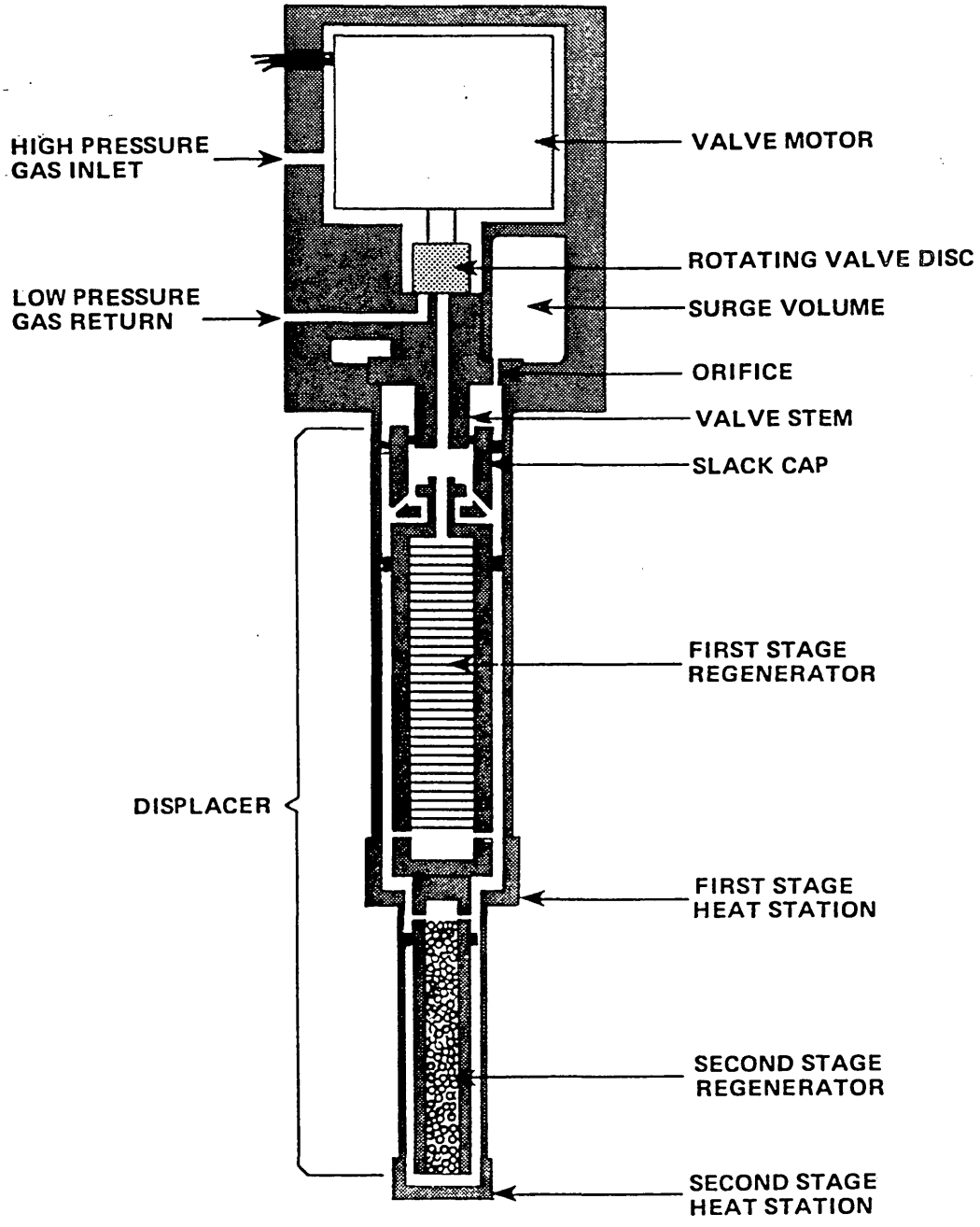

Figure 3.8 Simplified Expander Diagram

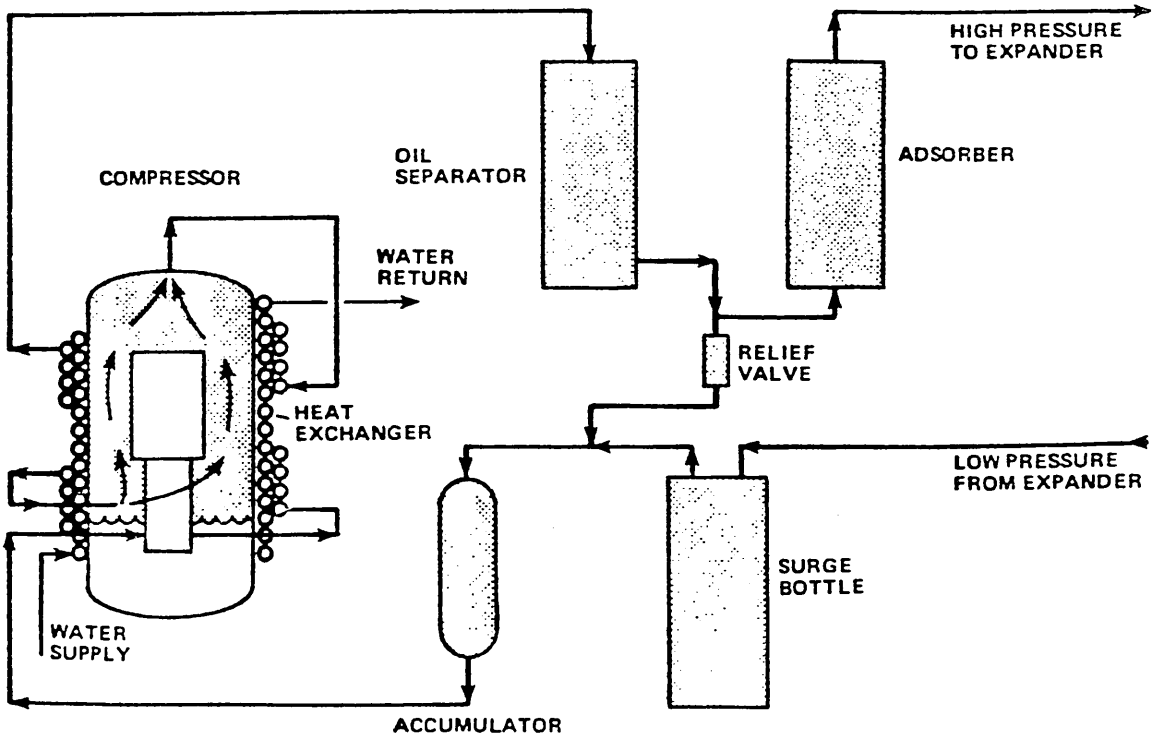

Figure 3.9 : Schematic Gas Flow Diagram

The main problem in the use of this type of closed cycle refrigerator is the elimination of vibration at the sample low temperature stage. The cryogenic system is designed such that the valve motor assembly and the cylinder assembly, Figure 3.10, can be mounted independently. These two parts are only 'directly' coupled by a rubber bellows and the exchange gas, NOT as shown in Figure 3.10 which shows a conventional cryostat where vibration isolation from the sample area is not a problem. However, the two parts must be

rigidly held in precise alignment and this requires some external framework.

An initial attempt utilised a rigid steel frame to support both parts. The only direct mechanical linkage being through the floor. However, this proved unsuccessful, the line widths of the spectra recorded at this stage exhibited line broadening due to residual vibration being transmitted to the sample low temperature stage.

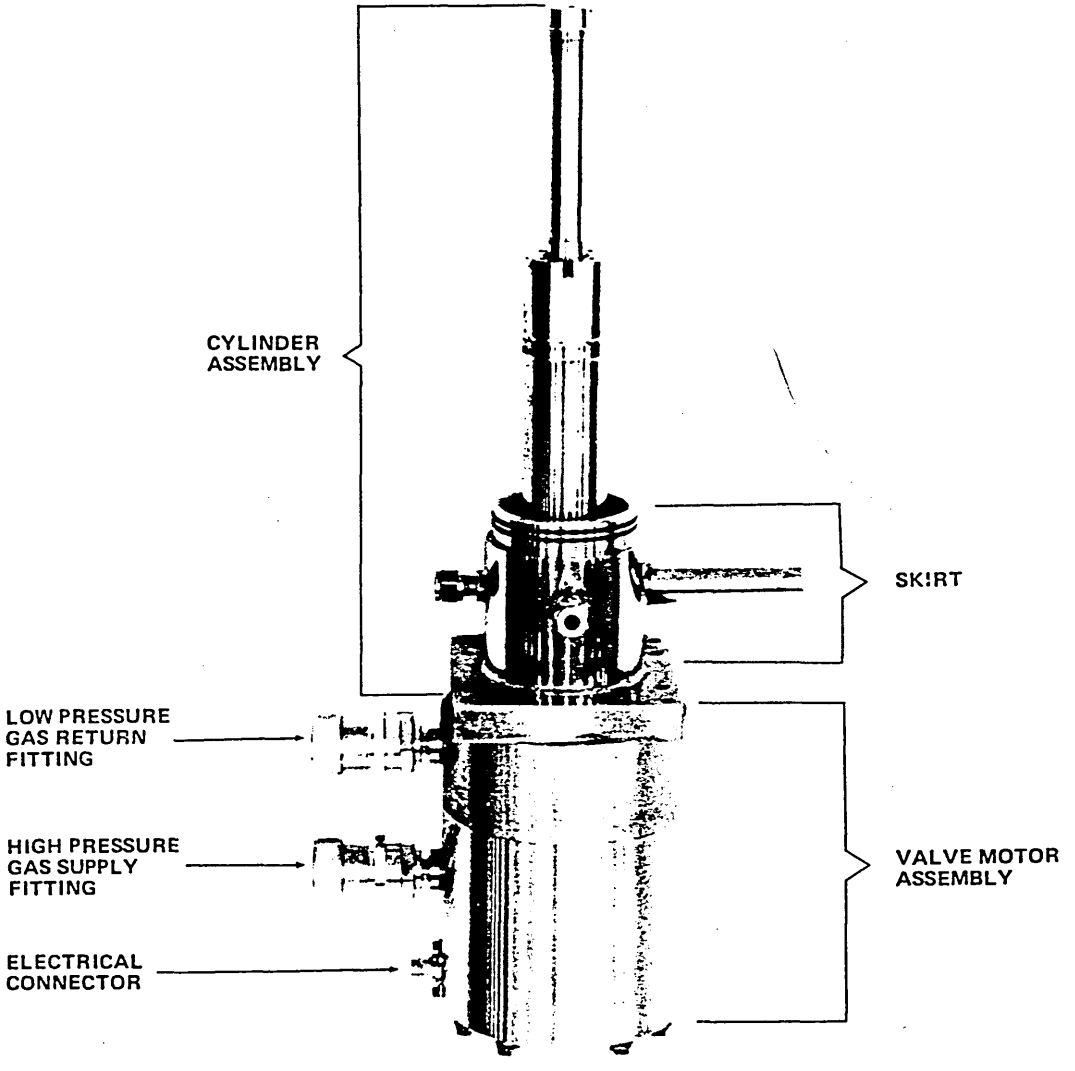

Figure 3.10 : Identifying the Cylinder and Valve Motor Assemblies

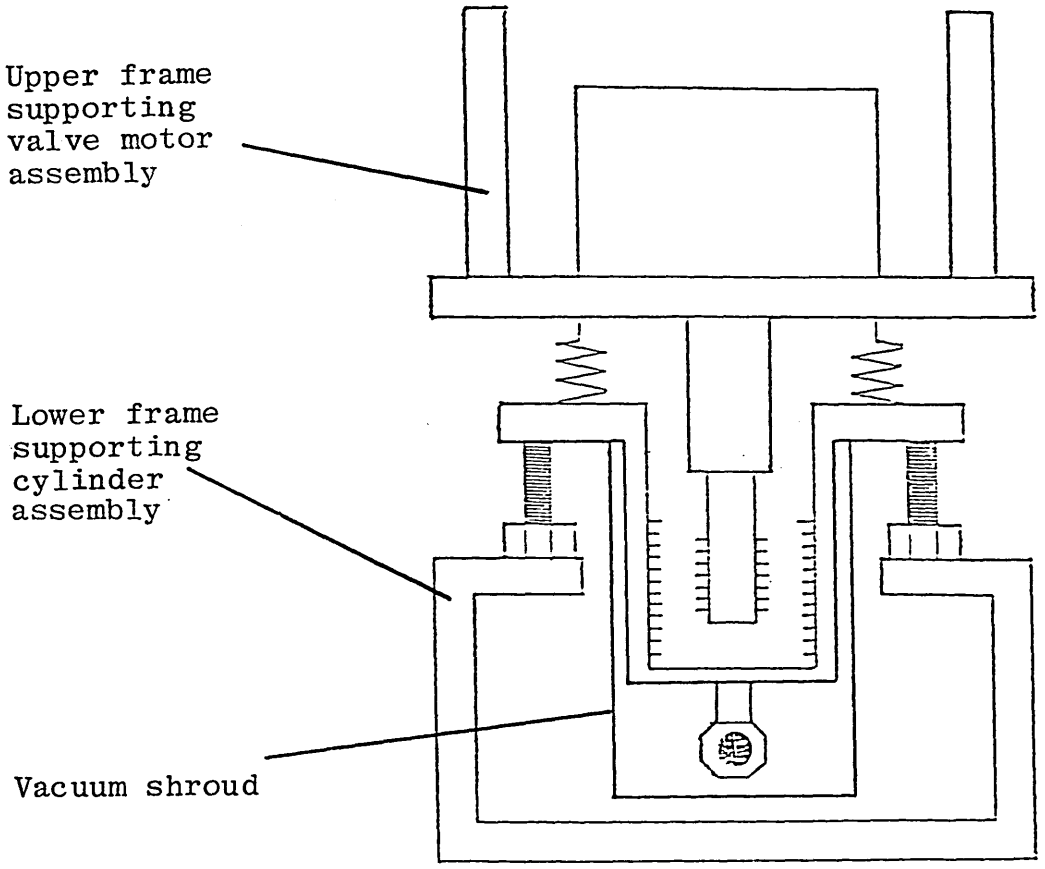

Figure 3.11 : Schematic showing the Modified Framework used to Support the Valve Motor Assembly and the Cylinder Assembly Cryostat Supported by a Rigid Steel Frame

A modified support system was devised in which the valve motor assembly was supported by an aluminium plate hung from a concrete pillar, and the cylinder assembly was supported by a lower frame bolted to the floor, Figure 3.11. A final solution was achieved by making the frame more rigid and by introducing damping between the uprights and at the base of the cylinder assembly. The Mössbauer spectrum of sodium nitroprusside $Na_2[Fe(CN)_5NO].2H_2O$ and an enriched ^{57}Fe foil were recorded at room temperature and at 12 K (the base temperature of the cryostat) to ensure all vibrations

had been isolated from the sample area. The data are summarized in Section 4.1.

3.7 Computer Fitting of Mössbauer Spectra

The use of computer facilities is essential for the determination of line positions, line widths and relative intensities in a Mössbauer spectrum. A program based on the work of Lang and Dale [15] on the computer fitting of Mössbauer spectra was used for the analysis of the data.

The constant acceleration vibrator produces a Doppler velocity which varies linearly from + V to 0 to - V and back to + V through a complete cycle of 512 channels. By the nature of the triangular waveform produced by the transducer, the two zero velocity positions are at mirror positions at the extremities of the source displacement. Consequently, the spectrum produced contains the mirror image of the data shown in the first half (0-255 channels) of the memory of the multichannel analyser, stored in the corresponding channels in the second half of the memory (256-511 channels).

3.7.1 Folding Program

The first operation in the fitting process is to fold the data stored in channels 0-255 on to the data in channels 256-511 and to add the counts stored in the corresponding channels. An accurate determination of the zero velocity position is ensured in the folding process by scanning 10 half-channels either side of

the expected folding position (128.5 channels) to find the best mirror axis for the absorption peaks so allowing for fluctuations in DC levels of the drive system. The best mirror axis is determined from the sum of the squares of the difference of the mirrored points.

3.7.2 Fitting Program

A visual inspection of the Mössbauer spectrum determined the type of fit to the data. Three options were used and these are summarised below:

OPTION 0.0 - This proved to be the most commonly used option for this work. Option 0.0 allows complex spectra to be fitted with a relatively small number of variable (or fixed) parameters. To achieve this, a matrix is constructed and a computer file describing this matrix is written. To illustrate this point, a typical matrix (Figure 3.12) and computer file (Figure 3.13) demonstrate how the magnetically split six line spectrum of α-Fe_2O_3 - which is complicated by a quadrupole perturbation - can be described using only nine parameters.

PRMTR NO	1	2	3	4	5	6	7	8	9
PRMTR TYPE*	P	P	P	W	W	W	D	D	D
PRMTR =	δ	H	Δ	$W_{1,6}$	$W_{2,5}$	$W_{3,4}$	$D_{1,6}$	$D_{2,5}$	$D_{3,4}$
LINE									
1	1	-2.7132	1	1	-	-	1	-	-
2	1	-1.5711	-1	-	1	-	-	1	-
3	1	-0.4289	-1	-	-	1	-	-	1
4	1	0.4289	-1	-	-	1	-	-	1
5	1	1.5711	-1	-	1	-	-	1	-
6	1	2.7132	1	1	-	-	1	-	-

* P = POSITION PARAMETER

W = WIDTH PARAMETER

D = DEPTH PARAMETER

Figure 3.12 : Matrix describing standard iron oxide α-Fe_2O_3

Thus:

Position of line 1 = $1 \times \delta - 2.7132 \times H + \Delta$

Width of line 1 = $1 \times W_{1,6}$

Depth of line 1 = $1 \times D_{1,6}$

where δ; H; Δ; $W_{1,6}$; $D_{1,6}$ are independent variables

```
 E MOSPARS PARSON B
OLD FILE.
.T*
TOF:
 &PRMTRS
 NLINES=6,
 OPTION=0.0,
 NPARS=9,
 OPPRMT=1.0,
 OFMINB=0.0,
 TEMIN=1.0,
 MAXFUN=200,
 KSW=5,
 TRUNC=1000,
 CENTRE=128.5,
 CALIBR=11.8
 KEEP=0,
 ISOLID=+1,
 DMAX=0.5,
 IPRINT=-20,
 H=0.002,
 ACC=2.5,
 POSPAR(1,1)=1,
 POSPAR(1,2)=-2.7132,
 POSPAR(1,3)=1,
 POSPAR(2,1)=1,
 POSPAR(2,2)=-1.5711,
 POSPAR(2,3)=-1,
 POSPAR(3,1)=1,
 POSPAR(3,2)=-0.4266,
 POSPAR(3,3)=-1,
 POSPAR(4,1)=1,
 POSPAR(4,2)=0.4266,
 POSPAR(4,3)=-1,
 POSPAR(5,1)=1,
 POSPAR(5,2)=1.5711,
 POSPAR(5,3)=-1,
 POSPAR(6,1)=1,
 POSPAR(6,2)=2.7132,
 POSPAR(6,3)=1,
 WIDPAR(1,4)=1,
 WIDPAR(2,5)=1,
 WIDPAR(3,6)=1,
 WIDPAR(4,6)=1,
 WIDPAR(5,5)=1,
 WIDPAR(6,4)=1,
 DEFPAR(1,7)=1,
 DEFPAR(2,8)=1,
 DEFPAR(3,9)=1,
 DEFPAR(4,9)=1,
 DEFPAR(5,8)=1,
 DEFPAR(6,7)=1,
 PRMTR=125.35,1.3,4,3,2,2,1.5,1,
 &END
    SEXTET PLUS QUADRUPOLE INTERACTION FITTING MATRIX
  2450000000000000020
EOF.
```

Figure 3.13 : Fitting File for α-Fe_2O_3

OPTION 1.0 - The absorption peaks are fitted as individual lines. Each line is described by a position, a width and a depth parameter. The computer varies each of these independently to obtain the best fit.

OPTION 2.0 - The absorption peaks are fitted as a number of doublets. The centre, splitting/2, widths and depths estimated from the folded data are varied until the best fit is obtained. The widths of the component lines are made equal.

Using any of these options (usually Option 0.0), a non-linear least squares subroutine is used to fit theoretical Lorentzian line shapes to the experimental data relative to a constant background, which takes into account small variations due to the cosine effect. The program is then used to:

(i) Calculate the line positions, widths and relative depths in the spectrum from the folded data.

(ii) Calculate a minimum in the differences between the sum of the squares of the experimental data points and the theoretical data points (obtained from a second subroutine in the program). This defines the χ^2 value which has the expression:

$$\chi^2 = \sum_{i=0}^{i=255} (\chi_i \text{experimental} - \chi_i \text{theoretical})^2$$

If the difference between the experimental and theoretical data is large or if the amount of

background scatter is great, then χ^2 will be large.

(iii) Use the least squares analysis to determine the optimum values of the background counts, baseline curvature and overall intensity of the final spectrum.

3.7.3 Calibration of the Mössbauer Spectrometer

The amplitude of the symmetric triangular waveform which drives the vibrator, is determined by the helipot setting on the servo amplifier and is related to the velocity range through which the vibrator is driven. Consequently, the 512 channels containing the data must be calibrated using the velocity range set by the helipot relative to the amplitude of the waveform. The calibration constant (in channels mm^{-1} s^{-1}) for a particular helipot is usually obtained using the magnetically split six line spectrum of enriched iron as a calibration standard (Figure 3.14). From Figure 3.15, it can be seen that the data on the ascending arm of the voltage ramp (0-256 channels) is the mirror image of the data on the descending arm of the voltage ramp.

The folded data (Section 3.7.1) is then fitted using Option 1.0. The line positions are now known in channels and in mms^{-1}, the calibration constant, c, is determined using the expression:

$$c = \frac{\text{Splitting}}{2 \times \text{Doppler Velocity}} \quad \text{channels } mm^{-1} \; s^{-1}$$

The positions of the lines are known to occur at the following Doppler velocities [1]:

lines (1,6) = ± 5.312 mms^{-1}

lines (2,5) = ± 3.076 mms^{-1}

lines (3,4) = ± 0.840 mms^{-1}

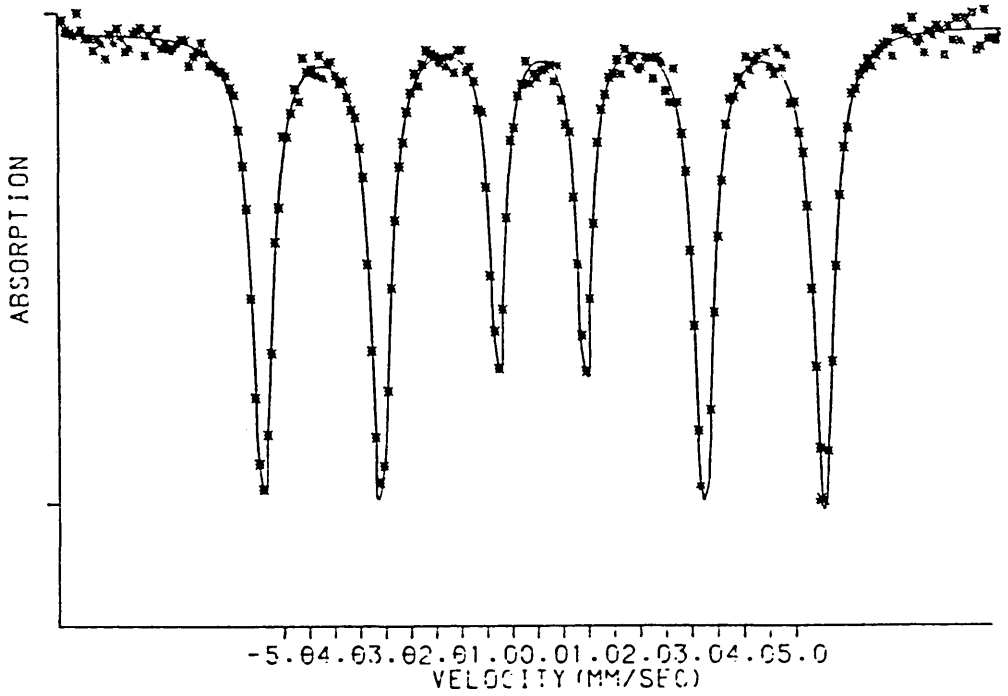

Figure 3.14 : ^{57}Fe Mössbauer Spectrum of Enriched Iron

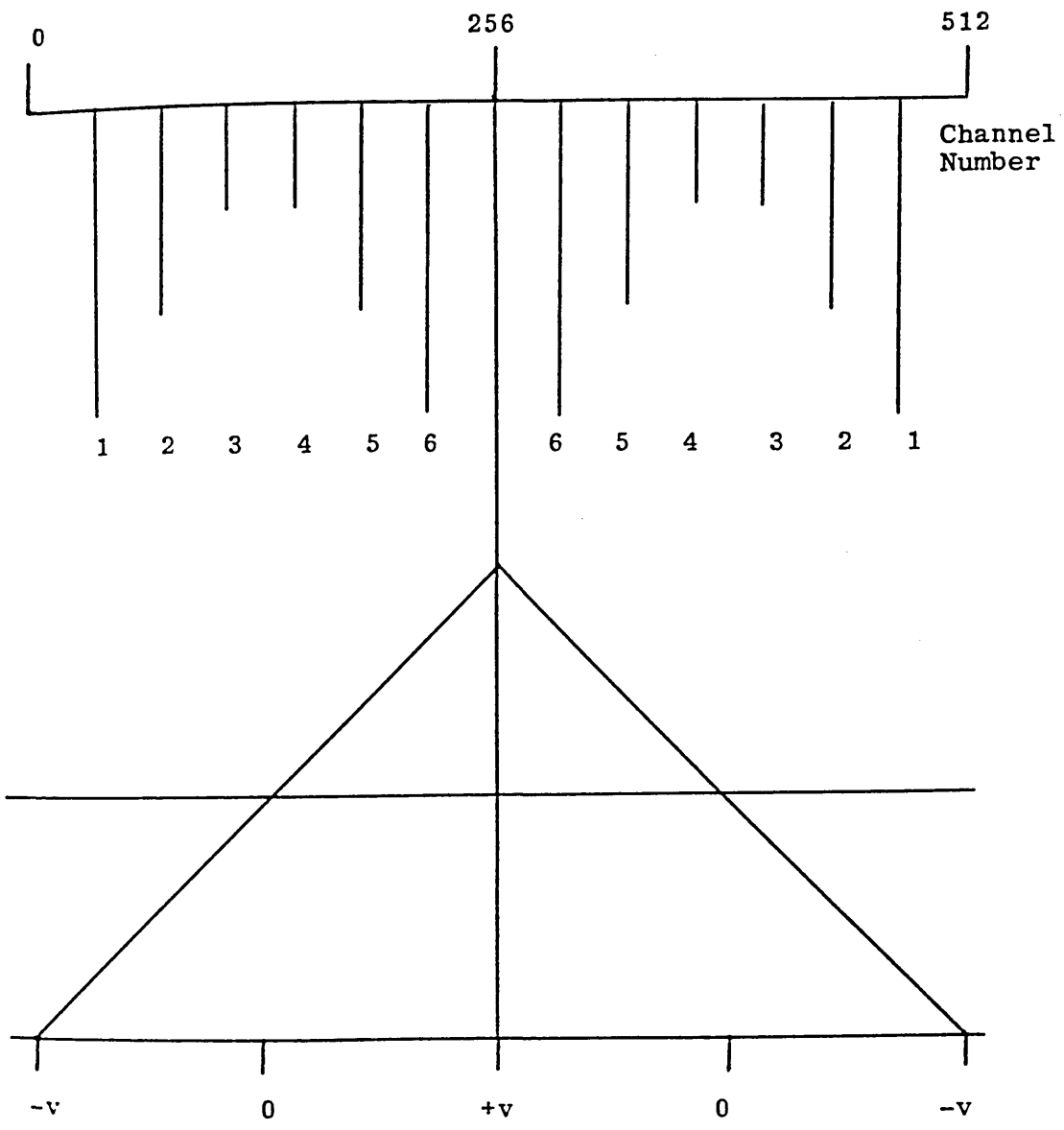

Figure 3.15 : Schematic Enriched Iron Spectrum Recorded Over 512 Channels

The final value for c is taken from the average of the three results obtained.

REFERENCES

1. J.G. Stevens, V.E. Stevens, Mössbauer Effect Data Index, p 54, 1975.

2. J.M. Williams, J.S. Brooks, Nucl. Instrm. Methods, 128, p 363, 1975.

3. F.J. Berry, Trans. Met. Chem., 4, p 209, 1979.

4. G. Longworth, X-ray and Conversion Electron Mössbauer Scattering for Chemists in: Mössbauer Spectroscopy Applied to Inorganic Chemistry, Vol 1, Edited by G.J. Long, 1984.

5. G. Longworth and R. Atkinson, in: Mössbauer Spectroscopy and its Chemical Applications, Edited by J.G. Stevens and G.K. Shenoy, Amer. Chem. Soc., Washington D.C., p 101, 1981.

6. M.J. Tricker, Mössbauer Spectroscopy and its Chemical Applications, Edited by J.G. Stevens and G.K. Shenoy, Amer. Chem. Soc., Washington D.C., p 63, 1981.

7. G.P. Huffman, H.H. Podgurski, Oxid. Met., 10, p37, 1976.

8. G.P. Huffman, Nucl. Instrms. Methods, 137, p 267, 1976.

9. M.J. Graham, D.F. Mitchell, D.A. Channing, Oxid. Met., 10, p 377, 1976.

10. Liljequist, Scanning Electron Microscopy, III, S. E. M., Inc., Illinois, p 997, 1983.

11. D. Liljequist, T. Ekdahl, U. Baverstam, Nucl. Instrm. Methods, 155, p 529, 1978.

12. O. Massenet, Nucl. Instrm. Methods, 153, p 419, 1978.

13. J.A. Sawicki, T. Tyliszczak, O. Gzewski, Nucl. Instrm. Methods, 190, p 433, 1981.

14. R. Atkinson, T.E. Cranshaw, Nucl. Instrm. Methods, 204, p 577, 1983.

15. G. Lang, B.W. Dale, Nucl. Instrm. Methods, 116, p 567, 1974.

CHAPTER 4 : VARIABLE TEMPERATURE MOSSBAUER SPECTROSCOPY

4.1 Vibration Isolation from the Displex Cryostat

4.2 Standard Oxide, Haematite, α-Fe_2O_3

4.3 Standard Oxide, Magnetite, Fe_3O_4

4.4 Environmental Corrosion Product

4.5 Aqueous Corrosion Product

4.6 Spectra

References

The interpretation of the Mössbauer spectra of many iron oxides and oxyhydroxides is often facilitated if spectra are recorded over a wide temperature range. Indeed, if relaxation or particle size phenomena are influencing the observed spectra, then variable temperature data is vital. The variable temperature facility described in Section 3.6 was used to record Mössbauer spectra of two standard oxides and two natural corrosion products over the temperature range 10-300 Kelvin. The samples were packed with iron-free graphite powder in a graphite sample holder to ensure a uniform temperature across the sample.

The standard oxides investigated were the best commercially available powder grades supplied by Johnson Matthey Chemicals. For reference purposes, the Mössbauer parameters of the common oxides and oxyhydroxides of iron are given in an appendix to this chapter.

4.1 Vibration Isolation from the Displex Cryostat

A major problem with the use of a closed cycle refrigeration system, as developed and used for this work, was the elimination of vibration at the sample low temperature stage. Figure 4.1 uses the spectrum of a thin ^{57}Fe foil to demonstrate the effect of vibration in the sample area. The spectra given in Figure 4.1 were recorded (a) using the cryostat before all vibration had been isolated and (b) using a conventional sample holder.

The effect of residual vibration is to significantly broaden the observed linewidths thereby reducing the amount of useful information gained. The linewidth of line 1, Γ_1, in Figure 4.1(a) is 0.54 mm s^{-1} compared to 0.24 mm s^{-1} in Figure 4.1 (b).

(a)

(b)

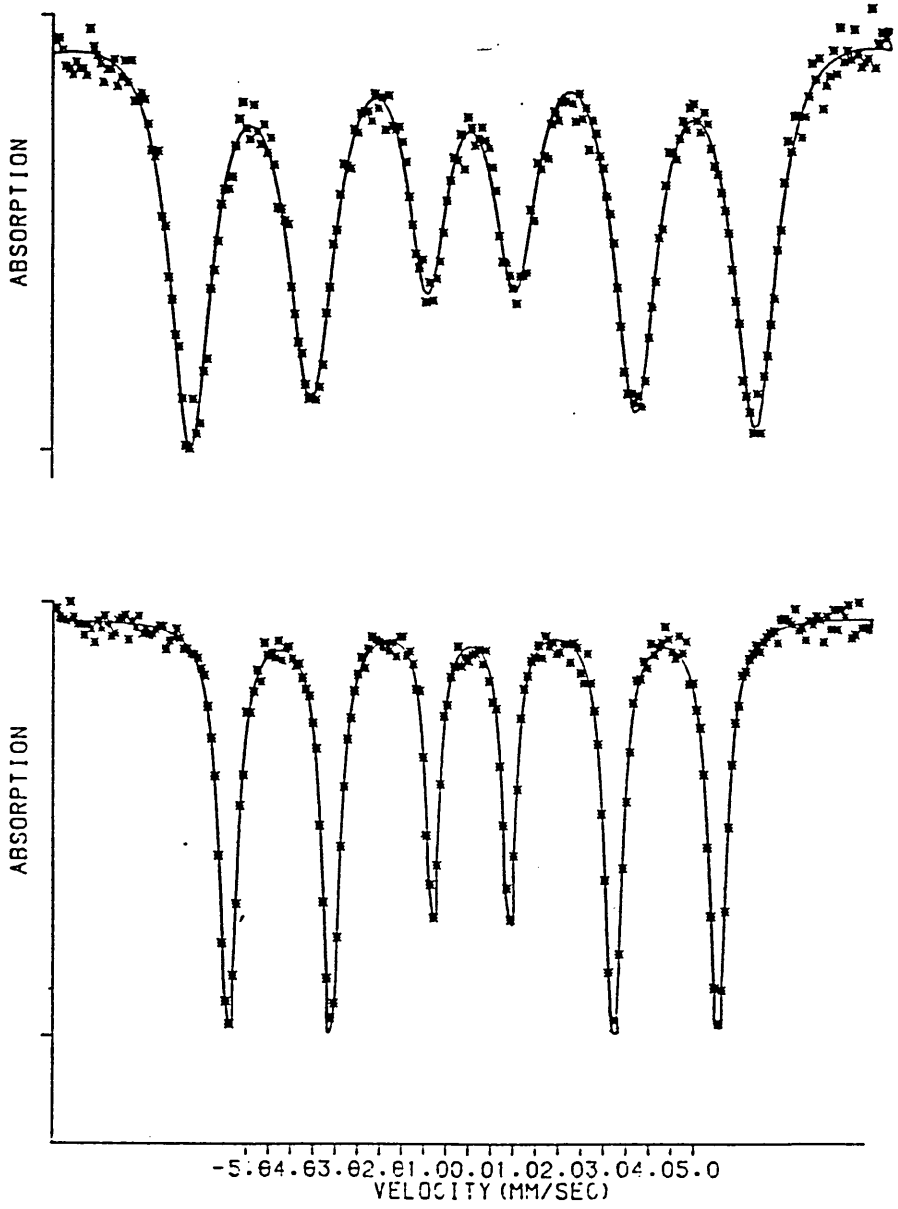

Figure 4.1 : The Effect of Vibration in the Sample Area on the Observed Spectrum of an ^{57}Fe Foil

Vibration isolation from the displex cryostat was finally achieved as described in Section 3.6 (in particular see Figure 3.11). To verify that all vibration had been isolated from the sample area, Mössbauer spectra of sodium nitroprusside, $Na_2[Fe(CN)_5NO].2H_2O$, and ^{57}Fe were recorded (a) at room temperature, the cryostat not operating, and (b) at 12 Kelvin, the base temperature of the operational cryostat with the Displex motor running. The observed linewidths (Table 4.1) remained constant.

Absorber	T/K	Γ_1/mm s^{-1}	Velocity Range
$Na_2[Fe(CN)_5NO].2H_2O$	298	0.12	± 4 mm s^{-1}
$Na_2[Fe(CN)_5NO].2H_2O$	12	0.12	± 4 mm s^{-1}
^{57}Fe	298	0.23	±12 mm s^{-1}
^{57}Fe	12	0.24	±12 mm s^{-1}

Table 4.1 : Linewidths for Two Different Absorbers at Room Temperature and at the Base Temperature of the Cryostat

The cryostat could now be used for the variable temperature study of certain absorbers.

4.2 Standard Oxide, Haematite, α-Fe_2O_3

The Mössbauer spectrum of a standard iron oxide haematite, α-Fe_2O_3, was recorded at 290 Kelvin (Spectrum 1) and at 6 Kelvin (Spectrum 2) using a liquid helium facility in the Department of Physics at the University of Sheffield. A computer fit to the data

revealed parameters in good agreement with published values [1,2]. On cooling to 6 Kelvin, a small positive increase in the isomer shift was observed, the reversal of the sign of the quadrupole perturbation of the magnetic field was clearly demonstrated in the spacings of the outer lines, and the internal magnetic field increased to a value of 544 kG. The data are summarised in Table 4.2

Spectrum	T/K	δ(Rh)/mm.s^{-1}	δ(Fe)/mm.s^{-1}	ε/mm.s^{-1}	H_{INT}/kG
1	290	0.24	0.34	- 0.11	520
2	6	0.29	0.40	0.18	544

Table 4.2 : Mössbauer Parameters for Haematite, α-Fe_2O_3, at 290 and 6 Kelvin

The value, epsilon ε, is quoted as a small quadrupole perturbation of the internal magnetic field where:

$$\varepsilon = \frac{e^2qQ}{4} \left(\frac{3\cos^2\Theta - 1}{2}\right)$$

Mössbauer spectra of the same sample were recorded at several temperatures between room temperature and 12 Kelvin using the displex cryostat (Spectra 3-12).

The instrumental operating conditions and absorber temperatures are summarised in Table 4.3.

Spectrum	T/K	Controller		
		Set point/K	Heater power/W	Vernier
3	287	-	OFF	-
4	200	200	12	34
5	175	175	12	38
6	150	150	12	50
7	125	125	12	60
8	100	100	12	63
9	75	75	5	63
10	50	50	5	63
11	23-26	25	1	68
12	12	0	0	-

Table 4.3 : Experimental Conditions for a Variable Temperature Study of α-Fe_2O_3 using the Displex Cryostat

Temperature control within ± 0.5 Kelvin was achieved in all cases except at a set point of 25 Kelvin when the sample area temperature fluctuated between 23 and 26 Kelvin.

On cooling from 287 K to 200 K, the sample has undergone the 90° spin rotation at 250 K (T_m), known as the Morin transition [3], this transition again manifests itself in the spectrum in the spacing of the outer lines. On cooling below 200 Kelvin, the spectrum remained essentially constant, the internal magnetic field increased very slightly as the temperature was lowered to an observed

value of 544 kG at 12 Kelvin. Spectra 1-12 are given in Section 4.6.1.

4.3 Standard Oxide, Magnetite, Fe_3O_4

The liquid helium facility at the University of Sheffield was again used to record spectra at 290 Kelvin (Spectrum 13) and 6 Kelvin (Spectrum 14). At room temperature, above the Verwey transition temperature, T_V = 119 Kelvin, [4], the Mössbauer spectrum consists of two unresolved sets of six line patterns. A computer fit of the data revealed parameters in good agreement with published values [1]. The ferric ions in tetrahedral (A) sites give rise to one six line pattern of internal magnetic field 494 kG. The other six line pattern of internal field 462 kG is assigned to the octahedral (B) sites occupied by ferrous and ferric ions. Above T_V, a fast electron hopping process between the ferrous and ferric ions is the reason why one pattern is observed [5,6].

At 6 Kelvin, well below T_V, the hopping process is inhibited due to an ordering of the ferrous ions in alternate [100] layers, which gives rise to the orthorhombic symmetry [7]. Two partially resolved six line patterns are apparently observed, (Spectrum 14). A computer fit of the data as two sextets revealed two internal magnetic fields of 518 kG and 489 kG. The larger of these fields is assigned to ferric ions on both A and B sites. The smaller field is assigned to the ferrous ions, the large quadrupole interaction results

from the orthorhombic symmetry [8]. The data, which are in broad agreement with published values, are summarised in Table 4.4.

Spectrum	T/K	δ(Rh)mm.s^{-1}	δ(Fe)/mm s^{-1}	ε/mm.s^{-1}	H_{INT}/kG
13	290	0.15 (A)	0.26 (A)	0.00 (A)	494 (A)
		0.53 (B)	0.64 (B)	0.00 (A)	462 (B)
14	6	0.27 (Fe^{3+})	0.38 (Fe^{3+})	0.00 (Fe^{3+})	518 (Fe^{3+})
		0.73 (Fe^{2+})	0.84 (Fe^{2+})	-0.39 (Fe^{2+})	489 (Fe^{2+})

Table 4.4 : Mössbauer parameters for Magnetite, Fe_3O_4 Recorded at 290 K and 6 K

The displex cryostat was used to obtain the Mössbauer spectrum of magnetite at various temperatures. The instrumental operating conditions and absorber temperatures were identical to those used for the variable temperature study of haematite. Temperature control was achieved as previously described (Table 4.3).

On cooling from room temperature to 125 Kelvin, the spectra remained essentially constant (Spectra 15-19). A slight increase in the internal magnetic fields from 484 kG and 462 kG for the A and B site iron atoms respectively at room temperature to 508 kG and 484 kG at 125 Kelvin was observed as the temperature was lowered. On cooling through the Verwey transition temperature, the spectrum changed dramatically as previously described (Spectrum 20).

Further cooling to 12 Kelvin had no appreciable effect on the spectrum (Spectra 21-24). A computer fit to the data recorded at 12 Kelvin, again as two sextets, revealed parameters identical with those for the 6 Kelvin spectrum given in Table 4.4. Below the Verwey transition temperature the areas of the lines are not fully consistent with the simple analysis of a unique B site ferrous cation site [9,10]. This has been taken into account in the computer fitting of data obtained by other groups [11,12]. Spectra 13-24 are given in Section 4.6.2.

4.4 Environmental Corrosion Product

The sample investigated was the long-term corrosion product formed on a wall tie widely used in the local construction industry of the 1920's. The loosely adhered corrosion product was carefully removed from a wall tie to provide the sample.

The room temperature Mössbauer spectrum revealed a quadrupole doublet plus additional unresolved high and low velocity lines suggested by the triangulation of the baseline (Spectrum 25). Considering only the dominant doublet, a computer fit to the data revealed an isomer shift $\delta(Fe) = 0.40$ mm s^{-1} and a quadrupole splitting $\Delta = 0.75$ mm s^{-1}, characteristic of Fe^{3+} (typical parameters for Fe^{3+}; $\delta(Fe) = 0.1 - 0.7$ mm s^{-1}; $\Delta = 0.0 - 1.0$ mm s^{-1}). This is the limit of the structural information that can be extracted from the

room temperature spectrum. A variable temperature study was therefore undertaken, the instrumental operating conditions and absorber temperatures were identical to those previously described. In this example, as the temperature was lowered, in addition to the doublet a sextet of broadened non-Lorentzian lines was observed. The relative intensity of the magnetic and paramagnetic components changed as a function of temperature (Spectra 26-36). These spectra are typical of a microcrystalline sample with a distribution of particle sizes. The spectra exhibit superparamagnetic relaxation, responsible for the collapse of the six line pattern, and collective magnetic excitations responsible for the unusual line shapes [13]. These phenomena are discussed in Section 2.3. At a sufficiently low temperature approximately 25 Kelvin for this sample, a more typical six line pattern was observed. A computer fit to the data recorded at 12 Kelvin as one sextet revealed an isomer shift δ(Fe) = 0.37 mm s^{-1}, a small quadrupole interaction ε = 0.10 mm s^{-1}, and an internal magnetic field H_{int} = 493 kG. These parameters correspond most closely to those of α-FeOOH [14]. However, if the same data were treated as two unresolved sextets, after the work of Chambaere et al [15], a better fit was obtained (Spectrum 26) and β-FeOOH is the suggested corrosion product. The parameters from this fit and those for the room temperature spectrum are summarised in Table 4.5. Spectra 25-36 are given in Section 4.6.3.

The complementary technique of X-ray diffraction (X.R.D.) was used to corroborate this interpretation.

Spectrum	T/K	δ(Rh)/mm.s^{-1}	δ(Fe)/mm s^{-1}	Quadrupole Interaction	H_{int}/kG
25	290	0.29	0.40	0.75	-
26	12*	0.40	0.51	- 0.05	495
		0.50	0.61	- 0.10	477

*The 12K spectrum is treated as two unresolved sextets.

Table 4.5 : Mössbauer Parameters for the Long Term Corrosion Product on a Wall Tie Recorded at 290K and 12K

The data was obtained using a Philips PW 1130/00/60 generator with a Philips PW 1050/25 diffractometer and an Advanced Metals Research graphite crystal monochromator.

Using the Bragg relationship, $n\lambda = 2d\sin\theta$ and knowing the wavelength of the incident radiation, Cu K_α = 1.5418 Å, values of d_{hkl} were obtained. If sufficient d values are accurately known then the diffracting material can be identified using the American Society for Testing of Materials (ASTM) search manual [16]. The instrumental operating conditions are summarised in Table 4.6. A part of the X.R.D. trace is given as an example in Figure 4.2. The data are summarised in Table 4.7. The reference number quoted in the final column, eg 13-157, identifies the search manual volume number, 13, and the card number,

157, for each of the compounds of interest. The relevant ASTM search manual cards are given in Table 4.8.

Generator Voltage:Current	2θ	Chart Speed	Target	Filter
40 kV:40 mA	5-110°	Variable	Cu	None

Table 4.6 : Instrumental Operating Conditions for the X-ray Diffraction Study of an Iron Corrosion Product

The X.R.D. data confirms the presence of β-FeOOH and the absence of α-FeOOH, consistent with the Mössbauer data considered as two sets of unresolved sextets. All but one of the more intense lines of β-FeOOH are observed, whereas many lines corresponding to α-FeOOH are absent, most notably those at d = 4.18 Å, (corresponding to a value of 2θ = 21.3°); d = 2.452 Å, (2θ = 36.6°); d = 2.192 Å, (2θ = 41.2°); and d = 1.721 Å, (2θ = 53.2°).

It is established that the presence of chloride ion favours the formation of β-FeOOH [17,18], the energy dispersive analysis of X-rays (EDAX) detection system of a Philips 500 scanning electron microscope was used to confirm the presence of chloride ion in this sample. All the evidence therefore suggests that β=FeOOH is the major corrosion product on this sample.

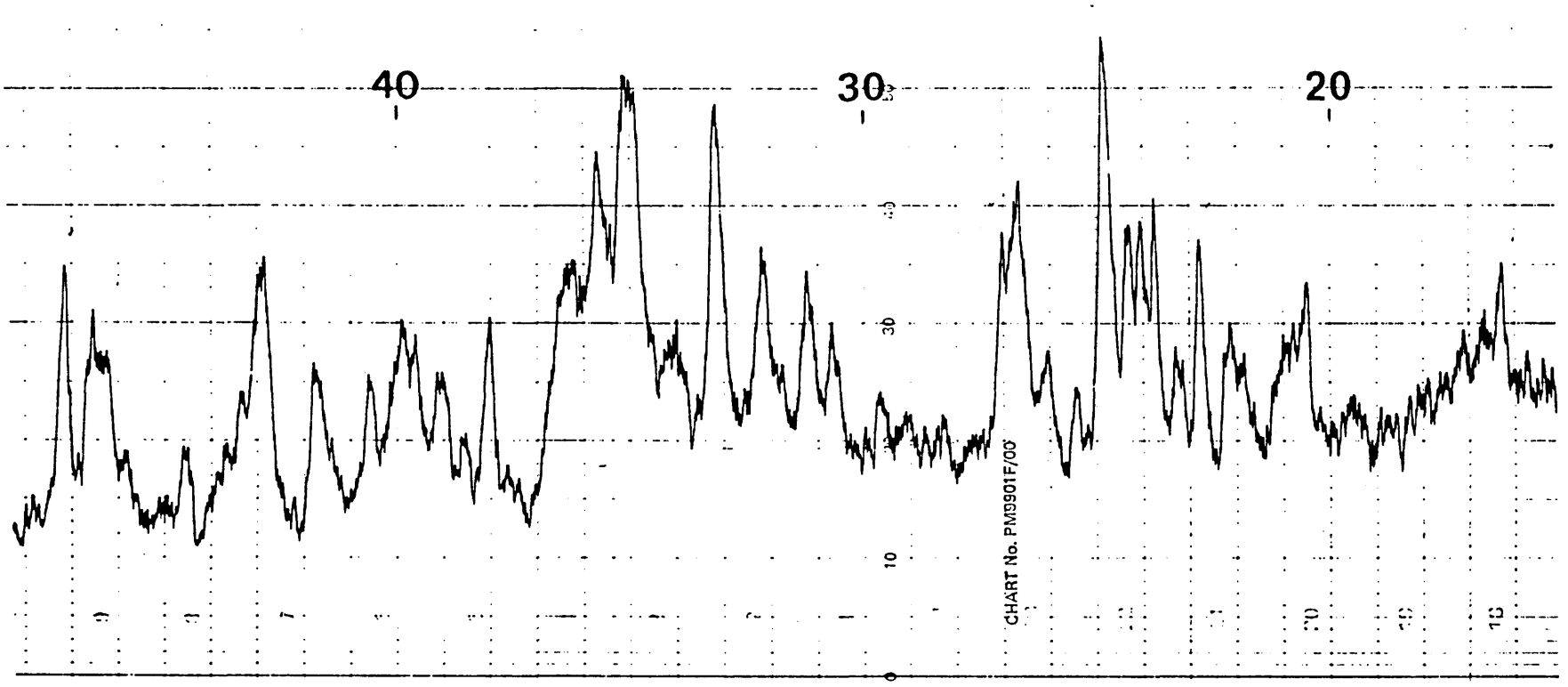

Figure 4.2 : Part of the X-ray Diffraction Trace obtained from the Long-term Corrosion Product in a Wall Tie

2θ	θ	sin θ	d/Å	Inference	Reference
16.9	8.45	0.1469	5.246	β-FeOOH	13-157
23.8	11.9	0.2062	3.739	γ-Fe_2O_3	24-81
27.0	13.5	0.2334	3.302	β-FeOOH	13-157
32.2	16.1	0.2773	2.780	γ-Fe_2O_3	24-81
34.2	17.1	0.2940	2.622	β-FeOOH	13-157
35.3	17.65	0.3032	2.543	β-FeOOH	13-157
38.6	19.3	0.3305	2.333	β-FeOOH	13-157
39.6	19.8	0.3387	2.276	β-FeOOH	13-157
43.1	21.55	0.3673	2.099	β-FeOOH	13-157
43.4	21.7	0.3697	2.086	γ-Fe_2O_3	24-81
43.6	21.8	0.3714	2.076	BOTH	BOTH
46.6	23.3	0.3955	1.949	β-FeOOH	13-157
52.2	26.1	0.4399	1.752	β-FeOOH	13-157
52.8	26.4	0.4446	1.734	β-FeOOH	13-157
53.9	26.95	0.4532	1.701	γ-Fe_2O_3	24-81
56.3	28.15	0.4718	1.634	β-FeOOH	13-157
61.0	30.5	0.5075	1.519	β-FeOOH	13-157
62.2	31.1	0.5165	1.493	β-FeOOH	13-157
62.8	31.4	0.5210	0.1480	BOTH	BOTH
63.7	31.85	0.5277	1.461	β-FeOOH	13-157
68.3	34.15	0.5614	0.373	β-FeOOH	13-157
74.4	37.2	0.6046	0.275	γ-Fe_2O_3	24-81

Table 4.7 : X-ray Diffraction Data for the Long-term Corrosion Product on a Wall Tie

(a)

13-157

d	7.40	3.31	1.64	7.40	β-FeOOH
I/I$_1$	100	100	100	100	BETA IRON(III) OXIDE HYDROXIDE (AKAGANÉITE)

Rad. A Filter Dia.
Cut off I/I$_1$, VISUAL ESTIMATE
Ref. MACKAY, MIN. MAG. 28 545 (1960)

Sys. TETRAGONAL S.G.
a_0 10.48 b_0 c_0 3.023 A C 0.2885
α β γ Z 8 Dx 3.555
Ref. IBID.

εα nωβ εγ Sign
2V D mp Color
Ref.

SYNTHETIC BY HYDROLYSIS OF $FeCl_3$ OR FeF_3 IN SOLUTION AT 60–100°C FOR 6 HOURS.

d Å	I/I$_1$	hkl	d Å	I/I$_1$	hkl
7.40	100	110	1.438	80	541
5.25	40	200	1.374	40	730,312
3.70	10	220			
3.311	100	310			
2.616	40	400			
2.543	80	211			
2.343	20	420			
2.285	40	301			
2.097	20	321			
2.064	20	510			
1.944	60	411			
1.854	10	440			
1.746	40	600			
1.719	10	501,431			
1.635	100	521			
1.515	40	002			
1.497	20	611			
1.480	20	112,7104			
1.459	10	640			

(b)

24-81 24-80A

d	2.52	1.48	2.95	5.90	γ-Fe_2O_3
I/I$_1$	100	53	34	2	gamma Iron Oxide (Maghemite)

Rad. FeKα λ 1.9373 Filter Dia.
Cut off I/I$_1$ Photometer I/Icor.
Ref. Haul and Shoon, Z. phys. Chemie, 44 216-26 (1939)

Sys. Cubic S.G. *
a_0 8.350 b_0 c_0 A C
α β γ Z Dx
Ref. Ibid.

εα nωβ εγ Sign
2V D mp Color
Ref.

*T^4 - $P2_13$ or O^2 - $P4_132$.
†Davies and Evans, J. Chem. Soc., 4373 (1956).
Low angle lines calculated from cell dimensions.

d A	I/I$_1$	hkl	d A	I/I$_1$	hkl
5.90	2	110	1.32	7	620
4.82	5	111	1.27	11	533
4.18	1	200	1.26	3	622
3.73	5	210	1.21	5	444
3.41	2	211	1.12	7	642
2.95	34	220	1.09	19	553,731
2.78	19	221	1.07	1	650
2.64†	-	310	1.04	8	800
2.52	100	311	1.04	1	652,740+
2.41	1	222	1.03	1	554,741+
2.32	6	320			
2.23	<1	321			
2.08	24	400			
1.87	<1	420			
1.70	12	422			
1.61	33	511,333			
1.55	<1	432,520			
1.53	1	521			
1.48	53	440			
1.43	1	433,530			

FORM T-2
W

(c)

17-536

d	4.18	2.69	2.45	4.98	αFeO(OH) $Fe_2O_3.H_2O$ ★
I/I$_1$	100	30	25	10	Iron Oxide Hydroxide Goethite

Rad. Co λ Filter Fe Dia. 19cm.
Cut off I/I$_1$
Ref. G. Brown, X-ray Ident. and Cryst. Struct. Clay Minerals, p. 386 London 1961 *

Sys. Orthorhombic S.G. Pbnm (62)
a_0 4.596 b_0 9.957 c_0 3.021 A 0.462 C 0.303
α β γ Z 4 Dx 4.264
Ref. Peacock, Trans. Roy. Soc. Canada 36 IV, 116 (1942)

εα 2.260 nωβ 2.393 εγ 2.398(Na) Sign
2V D 4.26 mp Color Black
Ref. Posnjak and Merwin, Am. J. Sci. 47 311 (1919)

Peacock records a weak line at 2.09, 5, 220.
* Cited by Harrison and Peterson, Am. Min. 50 704-712 (1965)

d Å	I/I$_1$	hkl	d Å	I/I$_1$	hkl
4.98	10	020	1.467	4	320
4.18	100	110	1.453	10	061
3.38	10	120	1.418	2	112
2.69	30	130	1.392	8	330
2.58	8	021	1.357	8	311
2.520	4	101	1.317	8	321
2.490	16	040	1.264	2	331
2.452	25	111	1.241	2	142
2.252	10	121	1.198	2	341
2.192	20	140			
2.009	2	131			
1.920	6	041			
1.799	8	211			
1.770	2	141			
1.721	20	221			
1.694	10	240			
1.661	4	060			
1.606	6	231			
1.564	16	151,160			
1.509	10	250,002			

Table 4.8 : The American Society for the Testing of Materials Search Manual Cards for a) β-FeOOH, b) γ-Fe_2O_3, c) α-FeOOH

The diffraction data might also suggest the presence of γ-Fe_2O_3. The d = 2.52 Å, (2θ = 35.6°); line may be present as a shoulder on an adjacent line. Other of the more intense lines are also present, for example d = 1.48 Å, (2θ = 62.8°); and d = 2.08 Å, (2θ = 43.5°). The lines at d = 2.95 Å (2θ = 30.3°); and d = 1.61 Å, (2θ = 57.2°), are however notably absent, and, in conjunction with the Mössbauer data it is therefore suggested that γ-Fe_2O_3 is not present in this sample. The many lines not accounted for are due to non-iron containing matter within the sample for example sand and cement.

4.5 Aqueous Corrosion Product

The corrosion product on an ordinary mild steel [19] immersed in deionised water for 3, 30 and 200 days respectively were investigated. Transmission and backscatter Mössbauer techniques were used. A variable temperature transmission study of the corrosion product obtained after 200 days was also undertaken. X-ray diffraction was again used to confirm the interpretation of the Mössbauer data.

The 2.5 cm x 2.5 cm tablets of mild steel were carefully removed from their aqueous environment, allowed to dry in air for a few minutes, then placed in the backscatter detector and the helium-methane gas mixture immediately turned on. The suspension of corrosion products in the aqueous medium were quickly filtered to provide a sample

for transmission experiments.

After 3 days immersion in deionised water, the transmission spectrum revealed a doublet with parameters $\delta(Fe) = 0.36$ mm s^{-1}, $\Delta = 0.60$ mm s^{-1}, typical of Fe^{3+} (Spectrum 37), the associated backscatter spectrum revealed a similar doublet with parameters $\delta(Fe) = 0.29$ mm s^{-1}, $\Delta = 0.66$ mm s^{-1} in addition to the typical six line pattern associated with the substrate (Spectrum 38). The transmission spectrum observed from the sample immersed for 30 days was more complex (Spectrum 39): in addition to a doublet, the characteristic pattern attributable to Fe_3O_4 was observed. A computer fit to the data revealed an isomer shift $\delta(Fe) = 0.36$ mm s^{-1} and a quadrupole interaction $\Delta = 0.55$ mm s^{-1}, typical of Fe^{3+} for the doublet and typical parameters for Fe_3O_4 from the other lines (Table 4.9). The associated backscatter spectrum (Spectrum 40) revealed essentially the same features. This spectrum is, however, further complicated by the six line pattern of the substrate. A computer fit to the data again revealed parameters typical of ferric iron plus Fe_3O_4. The variation in the observed parameters, particularly for the doublet, are not surprising in view of the small contribution to the total spectrum made by this component.

The transmission spectrum observed from the sample immersed for 200 days was identical to that observed after 30 days immersion (Spectrum 41). However, the

associated backscatter spectrum revealed no lines corresponding to Fe_3O_4 (Spectrum 43). The six line pattern of the substrate and a ferric doublet are the only lines observed. As the aqueous corrosion of this steel proceeds, it appears that each corrosion product is dislodged from the substrate surface to continuously expose a fresh surface to the corrosion process and the stable protective layer formed in some corrosion processes was not observed in this case [20].

A variable temperature study of the transmission sample after 200 days immersion was undertaken (Spectra 44-53). In marked contrast to the variable temperature study of the environmental corrosion product, the spectra remained essentially constant as the temperature was lowered. The internal field for both the A and B site ions in Fe_3O_4 increased to a value of 508 kG and 484 kG respectively at 125 Kelvin. Below the Verwey transition temperature, T_V = 119 K, the characteristic changes in the Fe_3O_4 pattern described in Section 4.3 were observed. A dramatic change in the spectrum was observed on cooling from 75 Kelvin (Spectrum 50) to 50 Kelvin (Spectrum 51). Further cooling produced a simpler spectrum and a computer fit to the data recorded at 12 Kelvin (Spectrum 42) revealed parameters typical of Fe_3O_4, again treated as two partially resolved six line patterns, plus a further sextet with an isomer shift δ(Fe) = 0.49 mm s^{-1} and internal hyperfine field H_{int} = 456 kG. These parameters are in excellent agreement with published values for

lepidocrocite, γ-FeOOH, which is paramagnetic down to at least 70 Kelvin and antiferromagnetic below about 50 Kelvin [21]. The exact values being influenced by the crystallinity of the sample [22].

The data are summarised in Table 4.9. Spectra 37-53 are given in Section 4.6.4.

The interpretation of the Mössbauer data was similarly confirmed using the X-ray diffraction technique. In this instance, the wavelength of the incident radiation was Co K_α = 1.7902 Å. The instrumental operating conditions are summarised in Table 4.10. A part of the X.R.D. trace is given as an example in Figure 4.3. The data are summarised in Table 4.11. The relevant ASTM search manual cards are given in Table 4.12. The X.R.D. data confirms magnetite and lepidocrocite are the corrosion products of this sample, all the major lines for both species are clearly identified. A far simpler trace is obtained from this corrosion product which is not contaminated with non-iron containing material.

In conclusion, the variable temperature Mössbauer facility developed as part of this work enables characteristic spectra to be recorded over a wide temperature range down to a base temperature of approximately 10 Kelvin without the requirement of a liquid helium facility. The technique demonstrates quite clearly the differences in the observed spectra between a sample which exhibits only bulk properties and one in which the particle size

distribution within the sample is such that the relaxation effects described in Section 2.3 become important. The non-destructive nature of the method enables the use of complementary techniques to confirm any interpretation made from the Mössbauer data. The value of a complementary technique will also be realised when the sample includes non-iron containing material about which the Mössbauer technique cannot yield any information.

Spectrum*	T/K	δ(Rh)/mm s^{-1}	δ(Fe)/mm s^{-1}	Quadrupole Interaction	H_{INT}/kG
37	290	0.25	0.36	Δ = 0.60	-
38	290	0.18	0.29	Δ = 0.66	-
39	290	0.25	0.36	Δ = 0.55	-
		0.18 (A)	0.29 (A)	ε = 0.00 (A)	485 (A)
		0.53 (B)	0.64 (B)	ε = 0.00 (B)	454 (B)
40	290	0.17	0.28	Δ = 0.61	-
		0.12 (A)	0.23 (A)	ε = 0.00 (A)	479 (A)
		0.45 (B)	0.56 (B)	ε = 0.00 (B)	447 (B)
41	290	0.25	0.36	Δ = 0.55	-
		0.18 (A)	0.29 (A)	ε = 0.00 (A)	491 (A)
		0.54 (B)	0.65 (B)	ε = 0.00 (B)	459 (B)
42	12	0.38	0.49	ε = 0.00	456
		0.34 (Fe^{3+})	0.45 (Fe^{3+})	ε = 0.00 (Fe^{3+})	522 (Fe^{3+})
		0.54 (Fe^{2+})	0.65 (Fe^{2+})	ε = 0.29 (Fe^{2+})	510 (Fe^{2+})
43	290	0.23	0.34	Δ = 0.64	-

*Spectra 38, 40 and 43 are backscatter electron spectra, an iron sextet with typical parameters is observed in each case.

Table 4.9 : Mössbauer Parameters for the Corrosion Products on a Mild Steel Immersed in Deionised Water

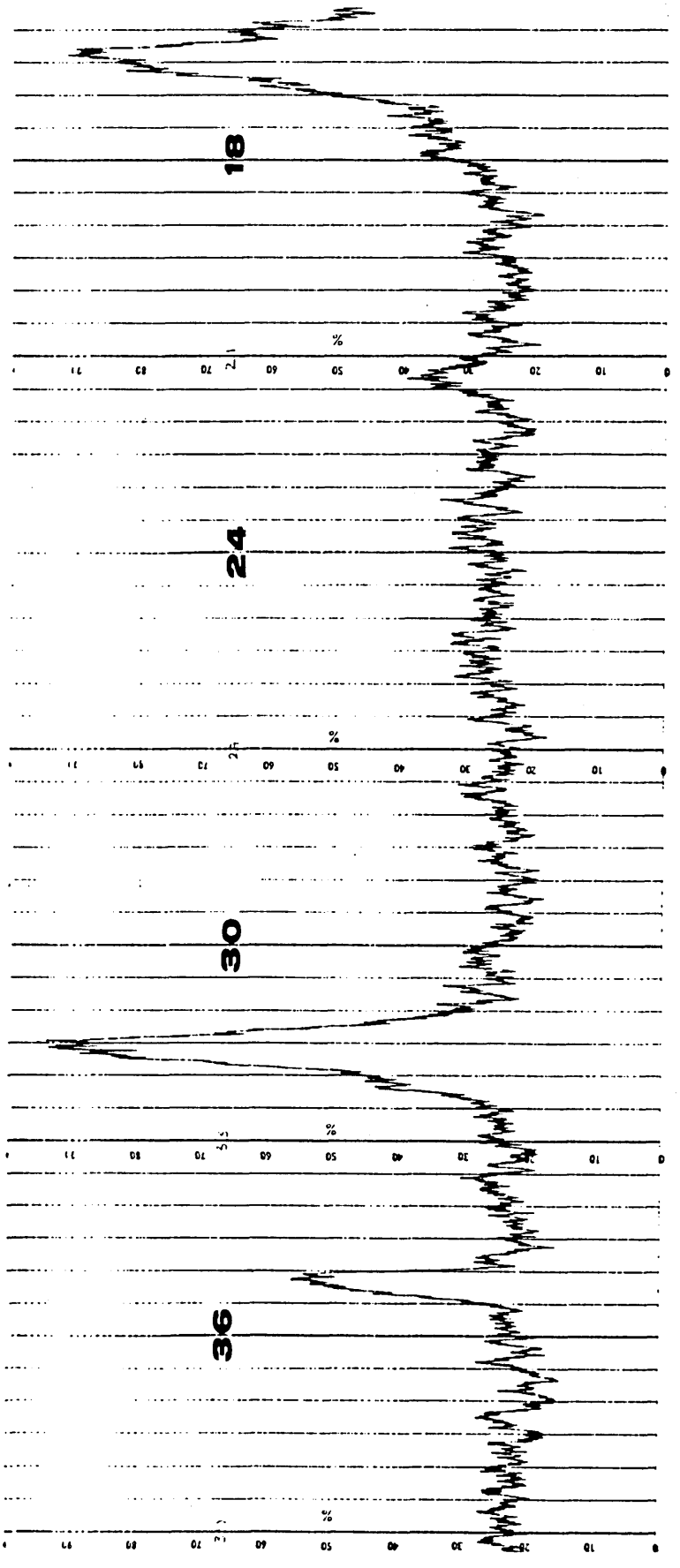

Figure 4.3 : Part of the X-ray Diffraction Trace obtained from the Aqueous Corrosion Product on a Mild Steel

2θ	θ	sin θ	d/Å	Inference	Reference
16.4	8.2	0.1426	6.277	γ-FeOOH	8-98
21.3	10.65	0.1848	4.844	Fe_3O_4	19-629
31.6	15.8	0.2723	3.287	γ-FeOOH	8-98
35.2	17.6	0.3024	2.960	Fe_3O_4	19-629
41.5	20.75	0.3543	2.526	Fe_3O_4	19-629
42.5	21.25	0.3624	2.470	γ-FeOOH	8-98
44.8	22.4	0.3811	2.349	γ-FeOOH	8-98
50.6	25.3	0.4274	2.094	BOTH	BOTH
55.2	27.6	0.4633	1.932	γ-FeOOH	8-98
57.7	28.85	0.4825	1.855	γ-FeOOH	8-98
62.2	31.1	0.5165	1.733	γ-FeOOH	8-98
63.2	31.6	0.5240	1.708	Fe_3O_4	19.629
67.4	33.7	0.5548	1.613	Fe_3O_4	19-629
69.7	34.85	0.5714	1.567	γ-FeOOH	8-98
71.5	35.75	0.5842	1.532	γ-FeOOH	8-98
72.2	36.1	0.5892	1.519	γ-FeOOH	8-98
74.2	37.1	0.6032	1.484	Fe_3O_4	19-629
77.2	38.6	0.6239	0.435	γ-FeOOH	8-98
81.7	40.85	0.6541	1.368	γ-FeOOH	8-98
82.3	41.15	0.6580	1.360	γ-FeOOH	8-98
85.2	42.6	0.6769	1.322	Fe_3O_4	19-629
89.0	44.5	0.7009	1.277	Fe_3O_4	19-629

Table 4.11 : X-ray Diffraction Data for the Corrosion Products on a Mild Steel Immersed in Deionised Water

(a)

8-98 MAJOR CORRECTION

d	6.26	3.29	2.47	6.26	FeO(OH)	1/2($Fe_2O_3 \cdot H_2O$)
I/I_1	100	90	80	100	Iron Oxide Hydrate	Lepidocrocite

Rad. CoKα λ 1.7902 Filter Fe Dia. 19cm
Cut off I/I_1 Visual
Ref. Rooksby "X-ray Identification and Crystal Structures of Clay Minerals" London, 1951, Facing p. 264

Sys. Orthorhombic S.G. Amam (63)
a_o 3.88 b_o 12.54 c_o 3.07 A 0.309 C 0.245
α β γ Z 4 Dx 3.95
Ref. Ibid.

εα 1.94 nωβ 2.20 εγ 2.51 Sign −
2V 83° D 3.854 mp 250°C Color red to red brown
Ref. Posnjak and Merwin, Am.J.Sci. 47 311 (1919)

Peacock, Trans. Roy. Soc. Canada 36 IV, 117 (1942) from Siegen, Westphalia, gives a=3.87, b=12.58, c=3.07, D_x=3.97
(Westphalia)
F-D values by Rooksby only

d Å	I/I_1	hkl	d Å	I/I_1	hkl
6.26	100	020	1.196	20	022,191
3.29	90	120	1.189	20	1.10.0
2.79	10R	011	1.10	2[illegible]	
2.47	80	031	1.075	40	Indices by Peacock
2.36	20	111			
2.09	20	131,060			
1.937	70	051,200			
1.848	20	220			
1.732	40	151			
1.566	20	080			
1.535	20	002			
1.524	40	231			
1.496	10R	022			
1.449	10	180			
1.433	20	171			
1.418	10	260			
1.389	10	122			
1.367	30	251			
1.261	10	091,320			
1.213	10	280			

(b)

19-629

d	2.53	1.49	2.97	4.85	Fe_3O_4
I/I_1	100	40	30	8	Iron(II,III) Oxide (Magnetite)

Rad. CuKα₁ λ 1.5405 Filter Ni Dia.
Cut off I/I_1 Diffractometer
Ref. National Bureau of Standards, Monograph 25, Sec. 5, 31 (1967)

Sys. Cubic S.G. Fd3m (227)
a_o 8.396 b_o c_o A C
α β γ Z 8 Dx 5.197
Ref. Ibid.

εα nωβ εγ Sign
2V D mp Color Black
Ref. Ibid.

Sample obtained from the Columbian Carbon Co., New York 17, New York.
Spectrographic analysis showed the following major impurities: 0.01 to 0.1% Co, 0.001 to 0.01% Ag, Al, Mg, Mn, Mo, Ni, Si, Ti and Zn.
Pattern taken at 25°C.

d A	I/I_1	hkl	d A	I/I_1	hkl
4.85	8	111	.8952	2	664
2.967	30	220	.8802	6	931
2.532	100	311	.8569	8	844
2.424	8	222	.8233	4	1020
2.099	20	400	.8117	6	951
1.715	10	422	.8080	4	1022
1.616	30	511			
1.485	40	440			
1.419	2	531			
1.328	4	620			
1.281	10	533			
1.266	4	622			
1.212	2	444			
1.122	4	642			
1.093	12	731			
1.050	6	800			
0.9896	2	822			
.9695	6	751			
.9632	4	662			
.9388	4	840			

FORM T-2

Table 4.12 : The American Society for the Testing of Materials Search Manual Cards for (a) γ-FeOOH (b) Fe_3O_4

4.6.1 Haematite, α-Fe_2O_3

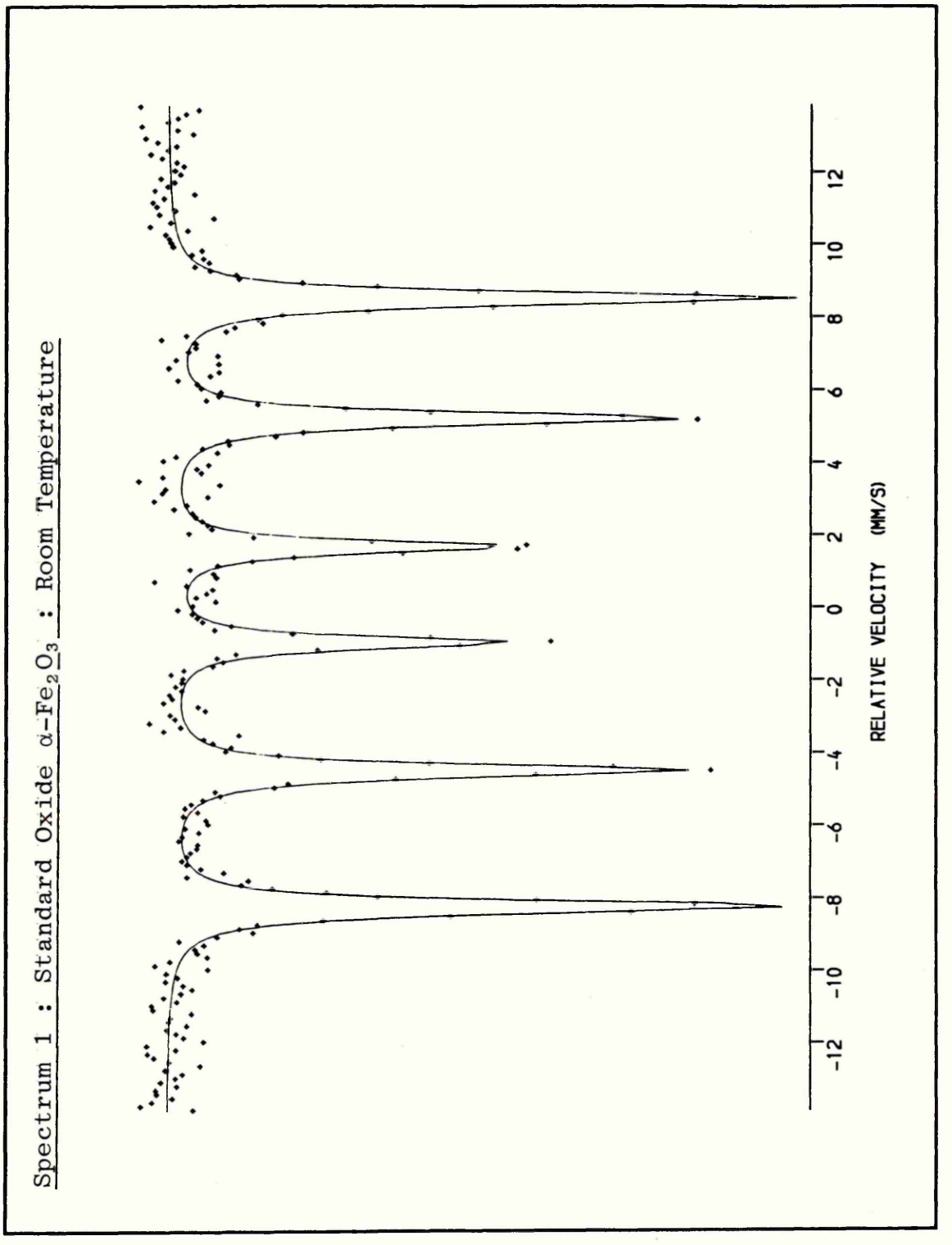

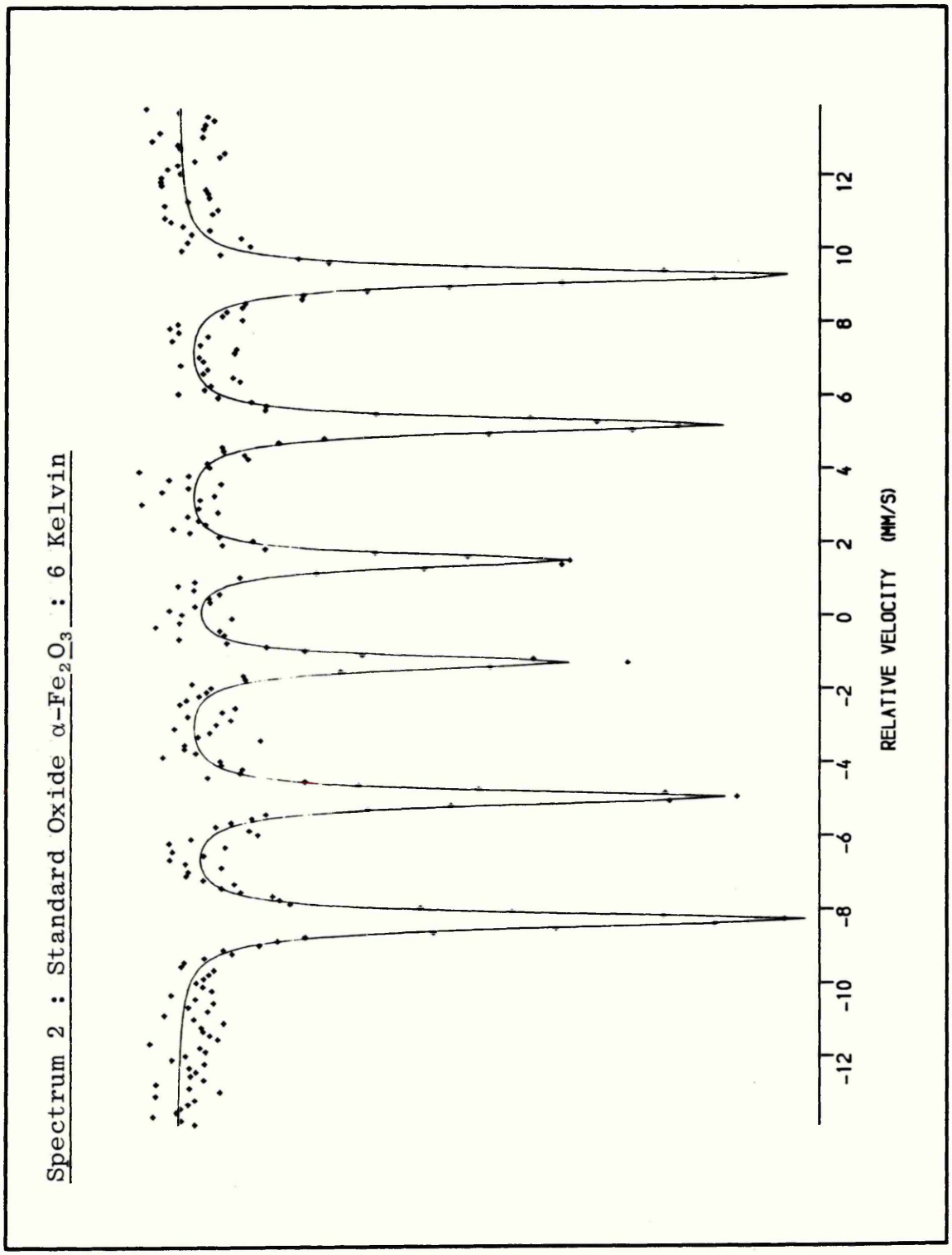
Spectrum 2 : Standard Oxide α-Fe2O3 : 6 Kelvin
-12
-10
-8
-6
-4
-2
0
2
4
6
8
10
12
RELATIVE VELOCITY (MM/S)

Standard Oxide, Fe_2O_3

Displex Variable Temperature Run.

Spectrum 3

SCT253T STANDARD OXIDE FE203 T=287K

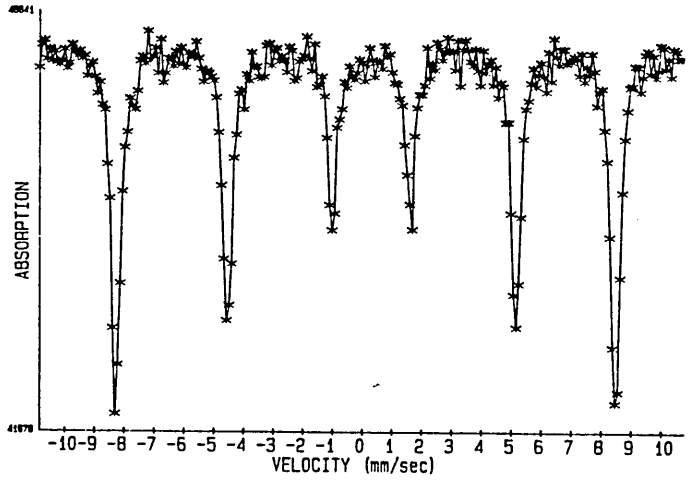

Spectrum 5

SCT261T STANDARD OXIDE FE203 T=175K

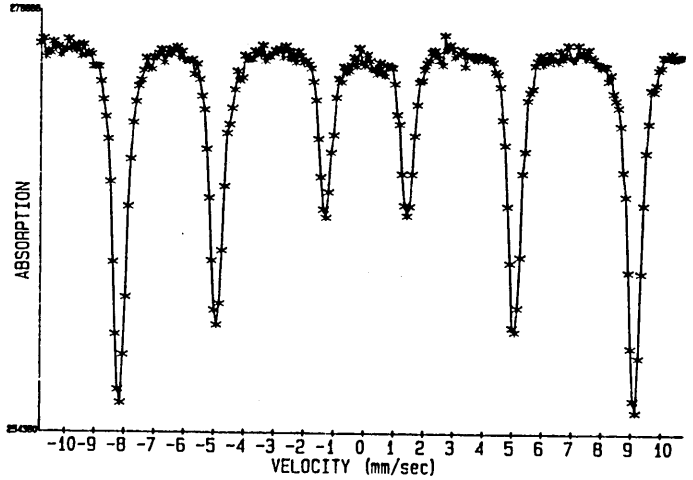

Spectrum 4

SCT262T STANDARD OXIDE FE203 T=200K

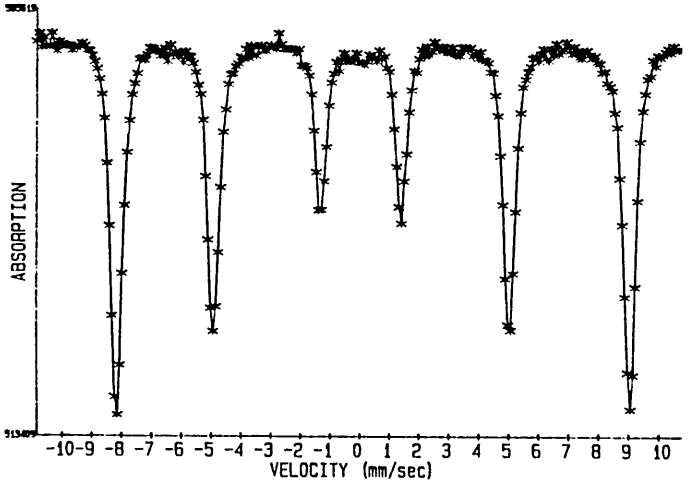

Spectrum 6

SCT260T STANDARD OXIDE FE203 T=150K

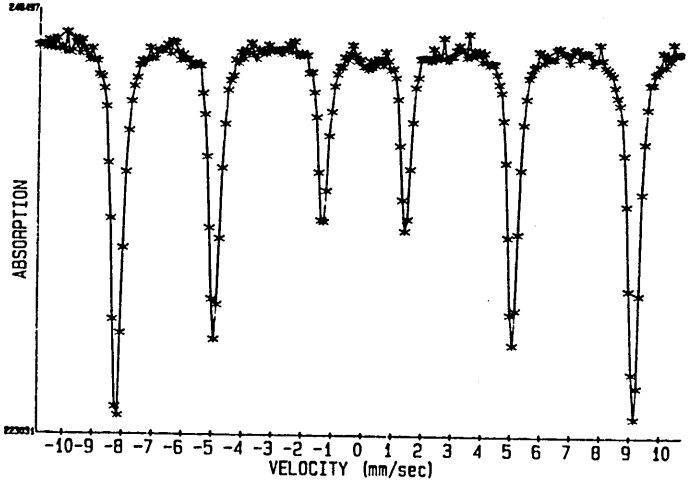

Spectrum 7

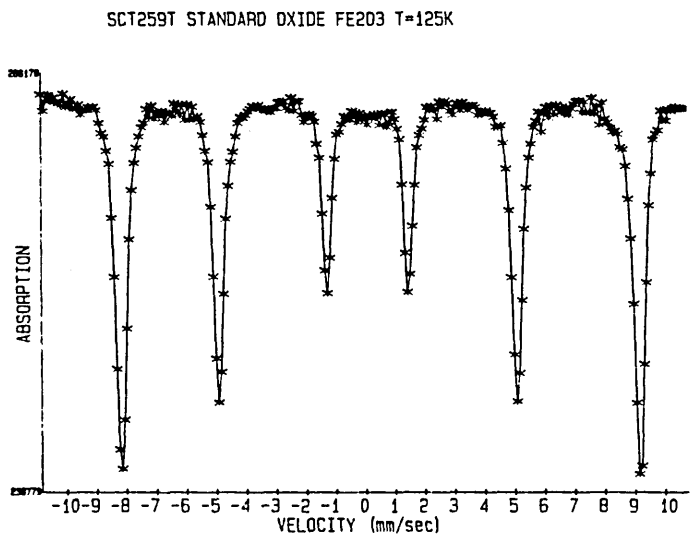

Spectrum 8

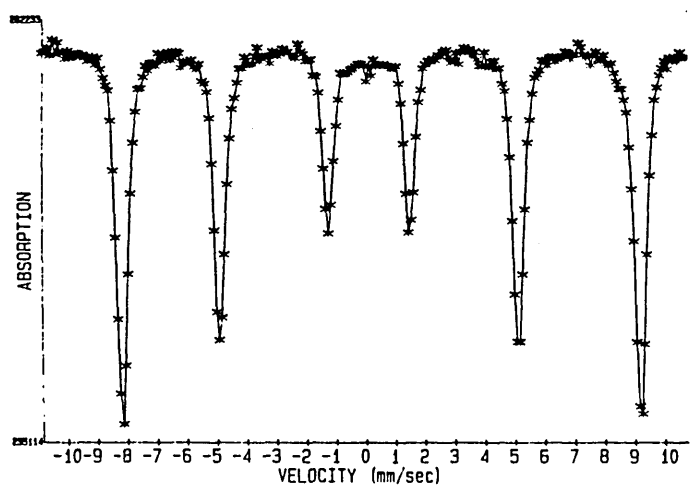

Spectrum 9

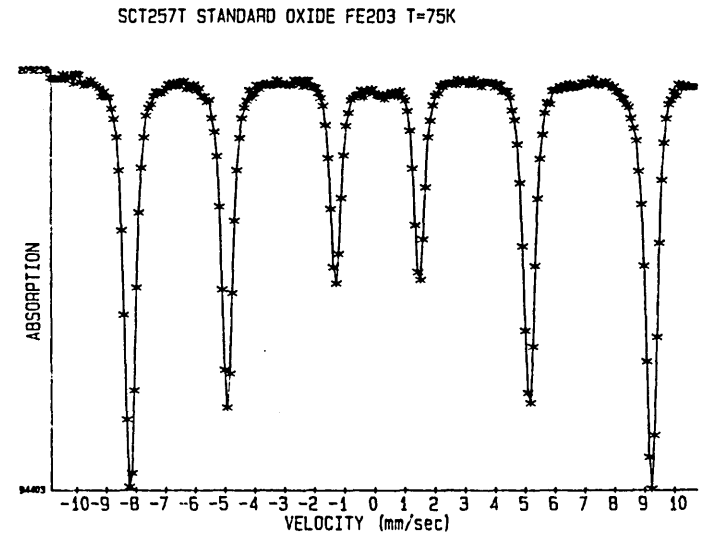

Spectrum 10

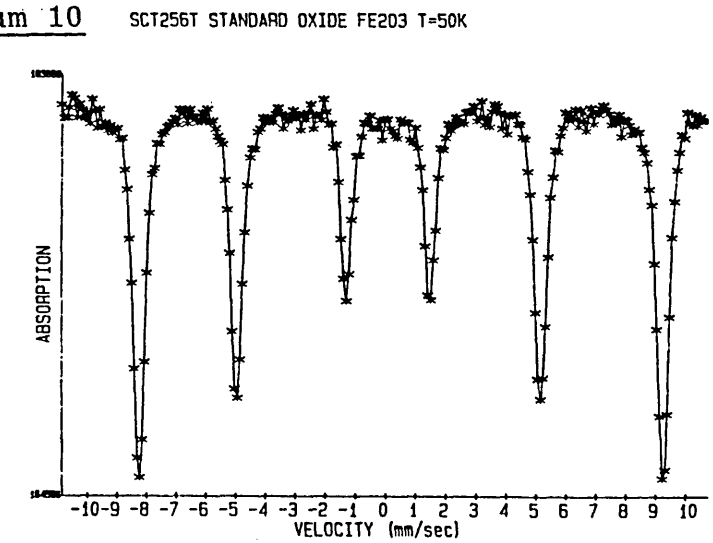

Spectrum 11

SCT255T STANDARD OXIDE FE203 T=25K

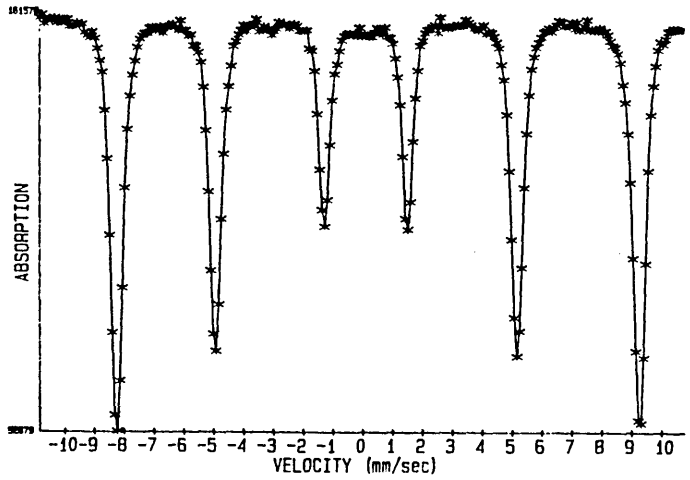

Spectrum 12

SCT254T STANDARD OXIDE FE203 T=12.5K

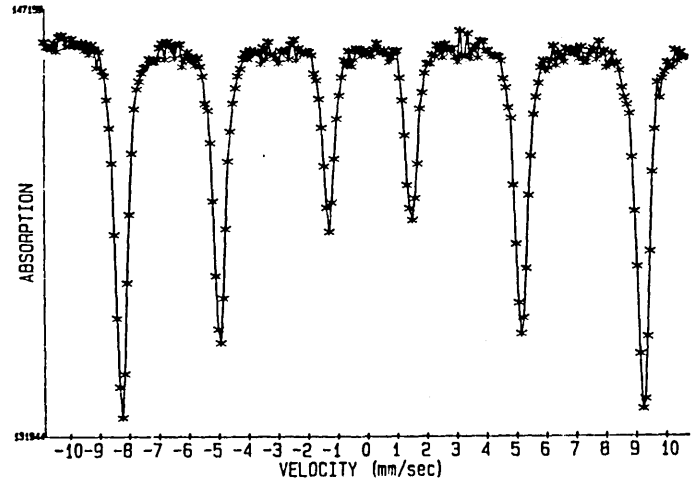

4.0.2 Magnetite, Fe_3O_4

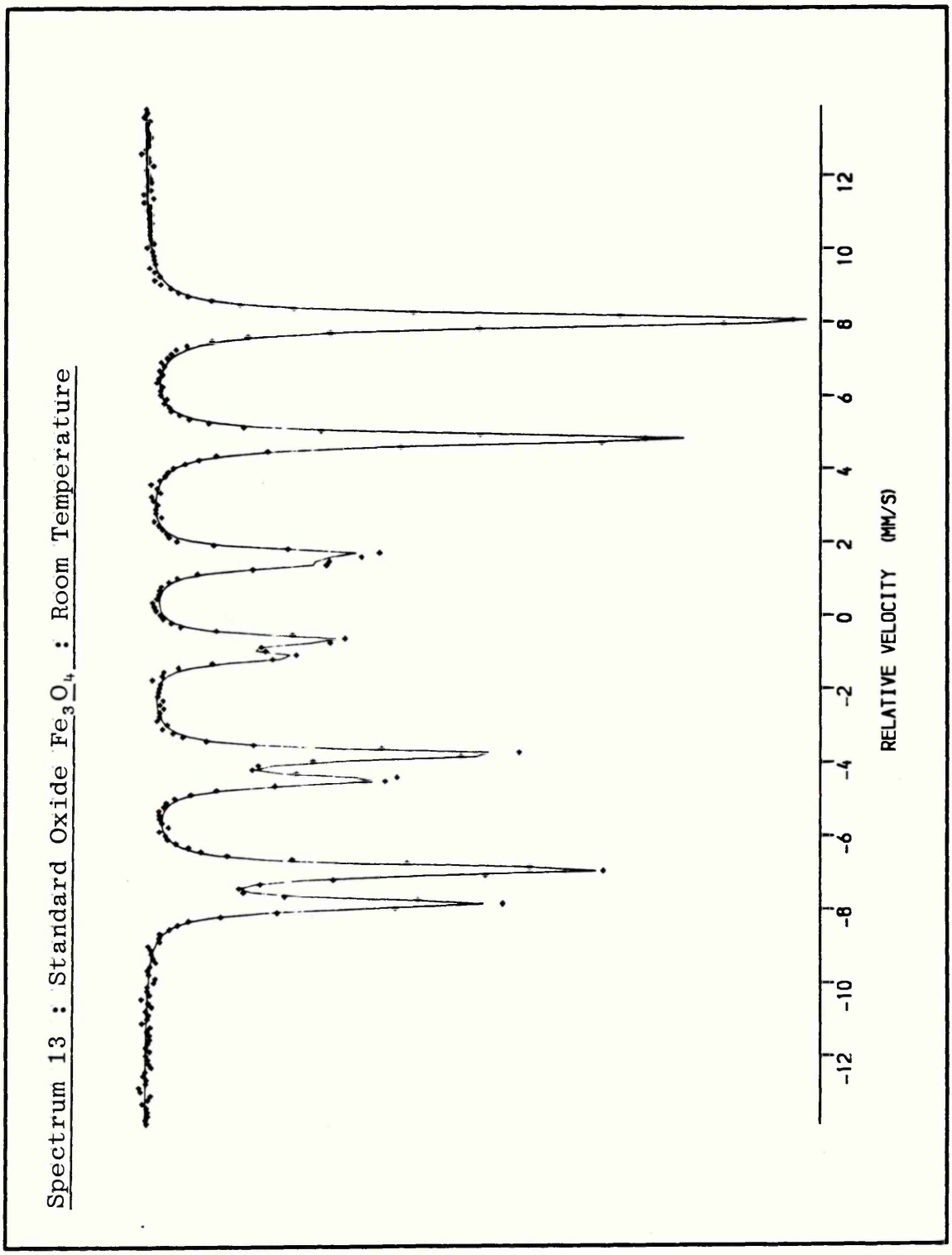

Spectrum 13 : Standard Oxide Fe_3O_4 : Room Temperature

Spectrum 14 : Standard Oxide Fe_3O_4 : 6 Kelvin

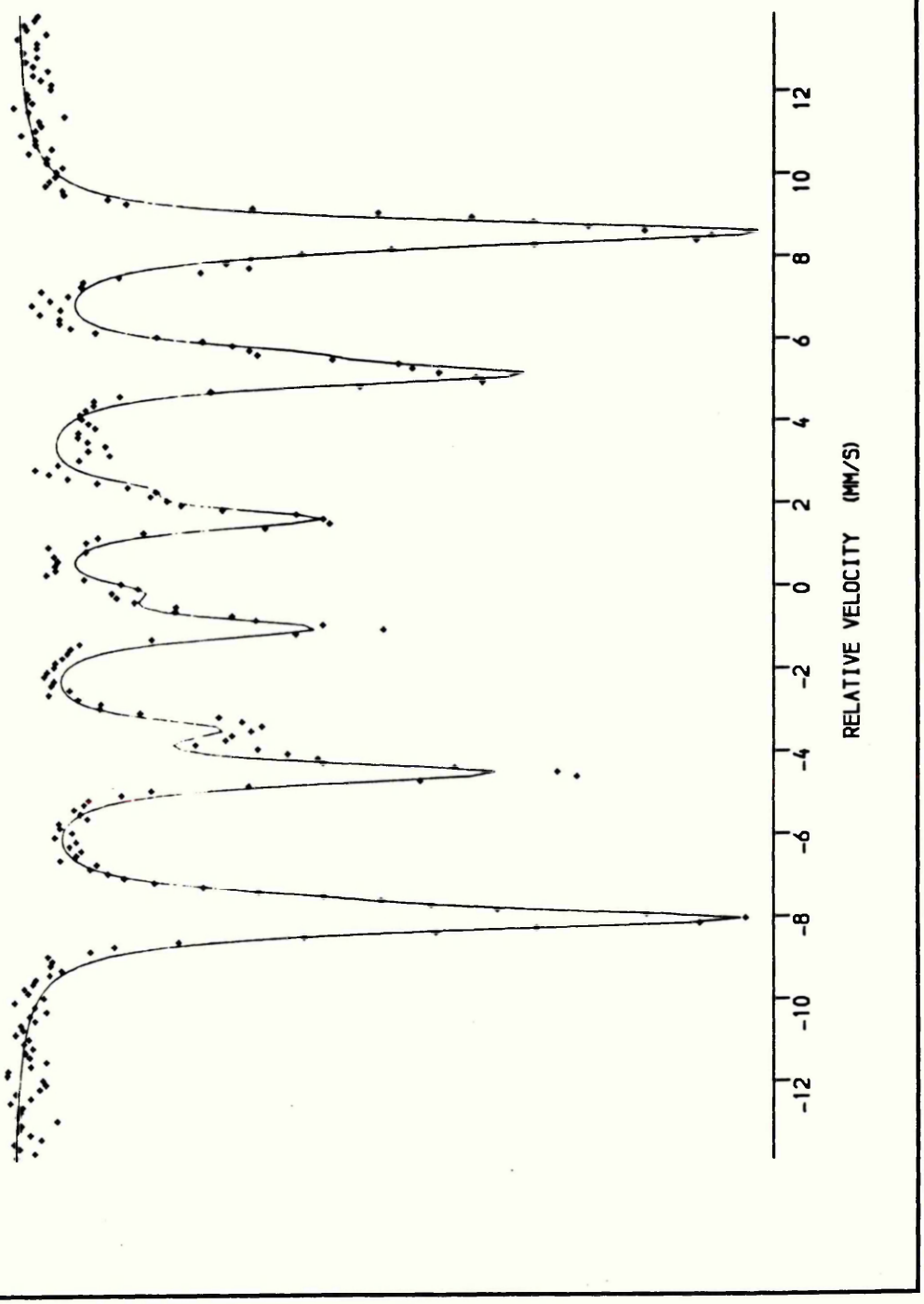

Standard Oxide, Fe_3O_4

Displex Variable Temperature Run

Spectrum 15

SCT359T STANDARD OXIDE FE304 T=290K

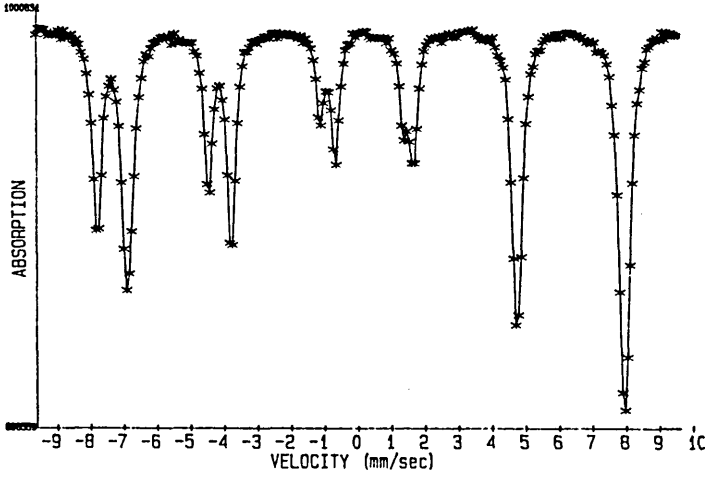

Spectrum 16

SCT252T STANDARD OXIDE FE304 T=200K

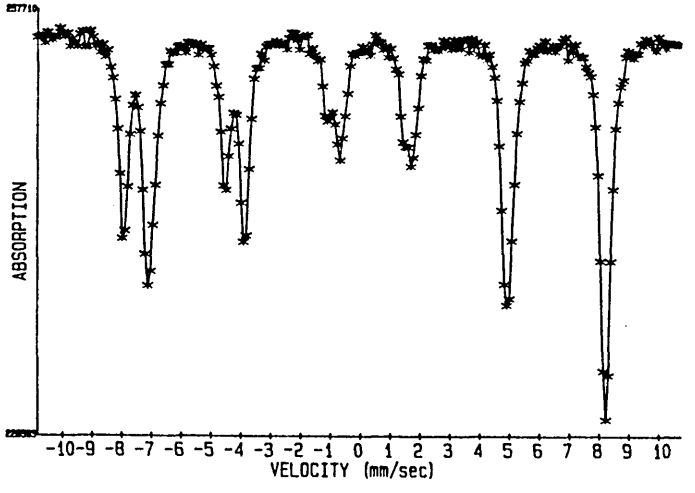

Spectrum 17

SCT251T STANDARD OXIDE FE304 T=175K

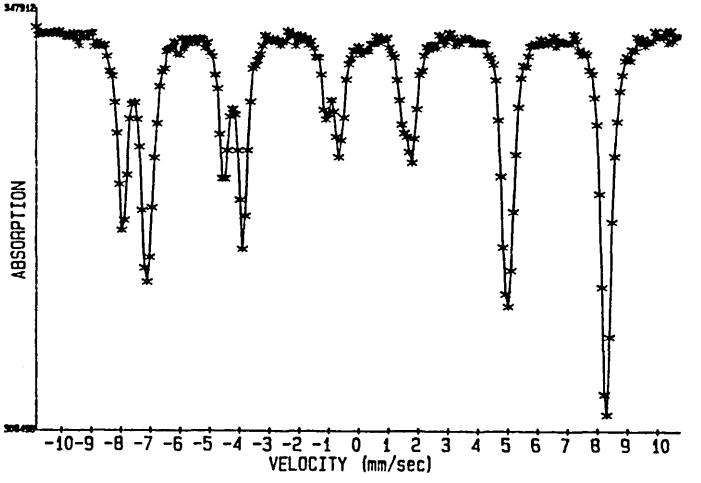

Spectrum 18

SCT250T STANDARD OXIDE FE304 T=150K

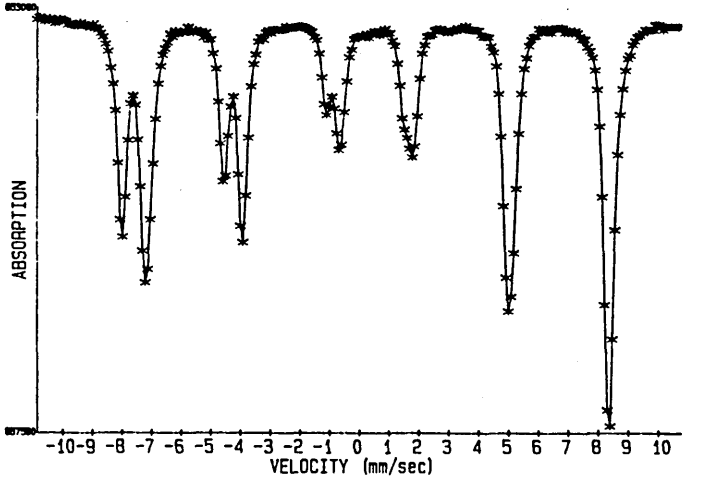

Spectrum 19

SCT249T STANARD OXIDE FE304 T=125K

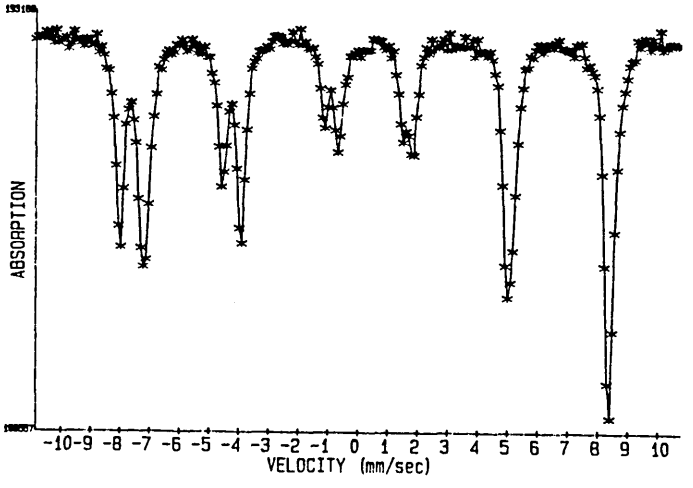

Spectrum 20

SCT248T STANDARD OXIDE FE304 T=100K

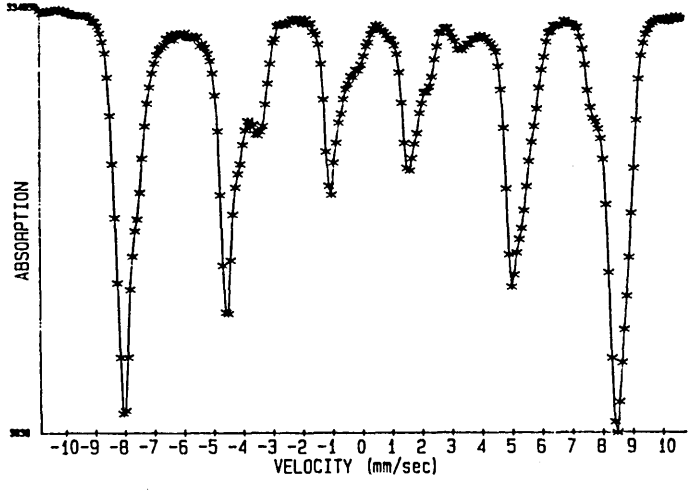

Spectrum 21

SCT247T STANDARD OXIDE FE304 T=75K

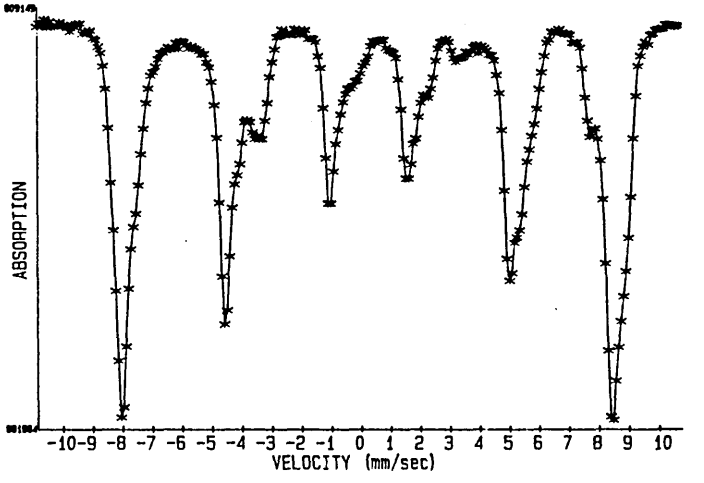

Spectrum 22

SCT246T STANDARD OXIDE FE304 T=50K

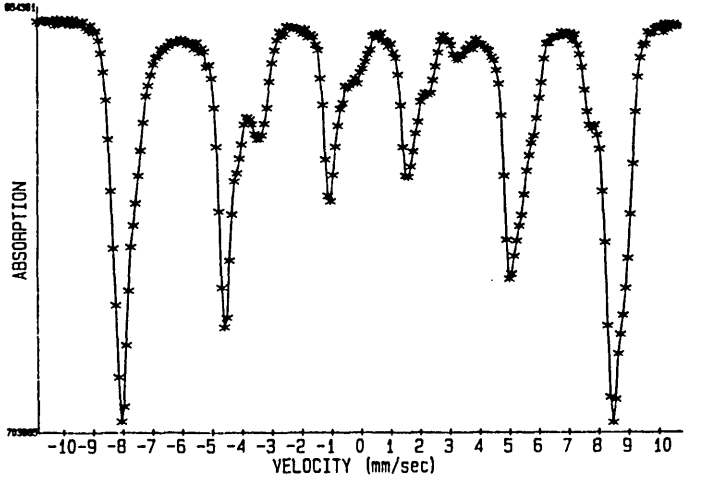

4.6.3 Environmental Corrosion Product

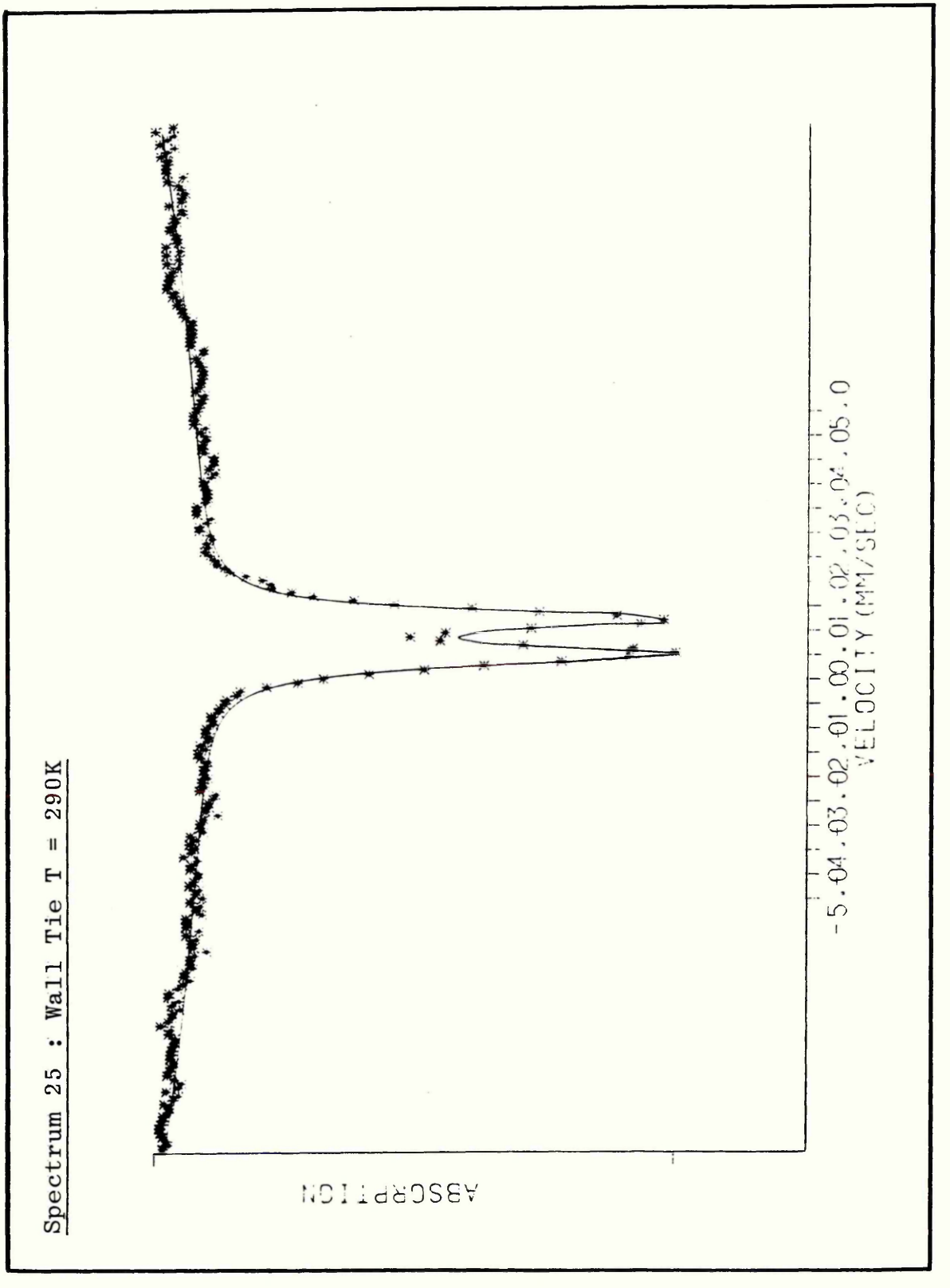

Spectrum 26 : Wall Tie T = 12K

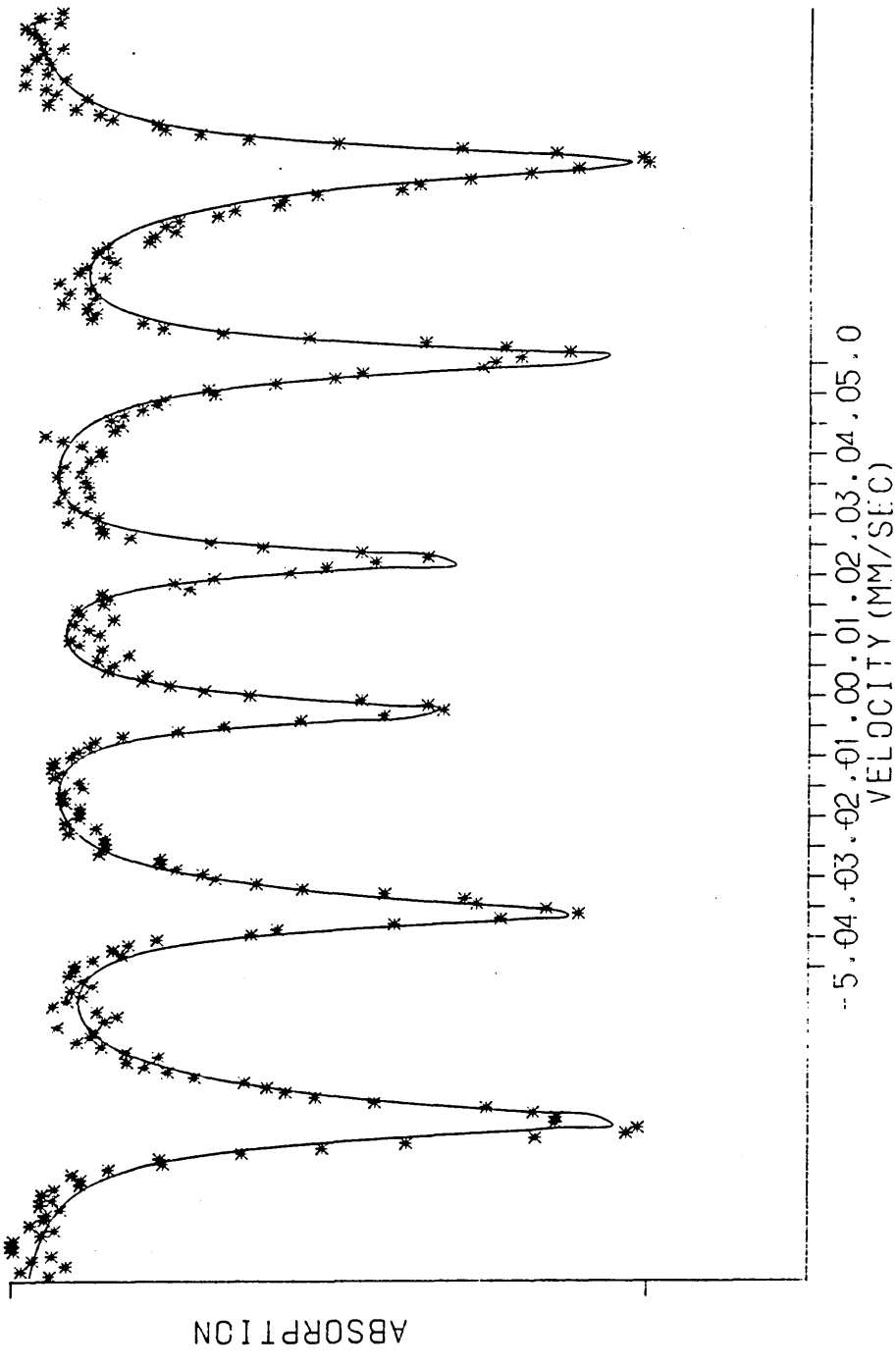

Wall Tie Corrosion Product

Displex Variable Temperature Run

Spectrum 27

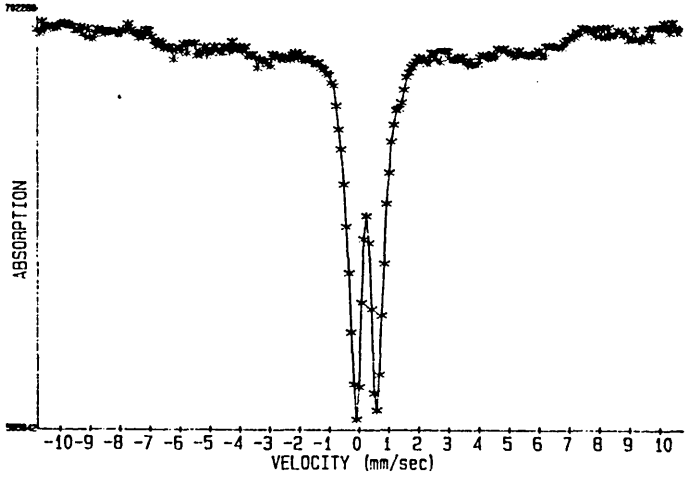

Spectrum 28

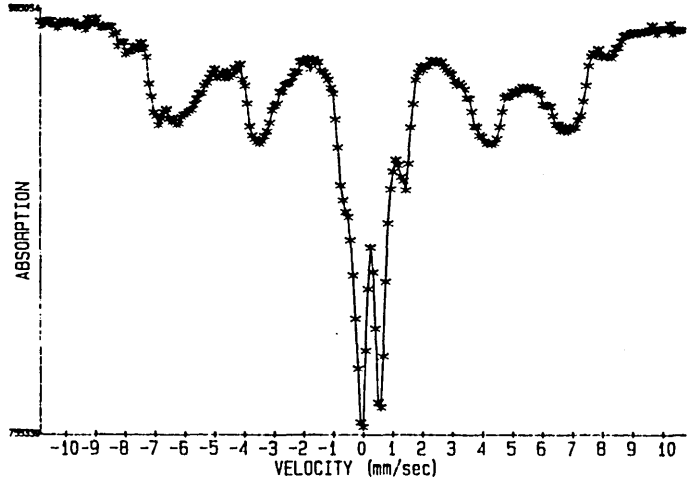

Spectrum 29

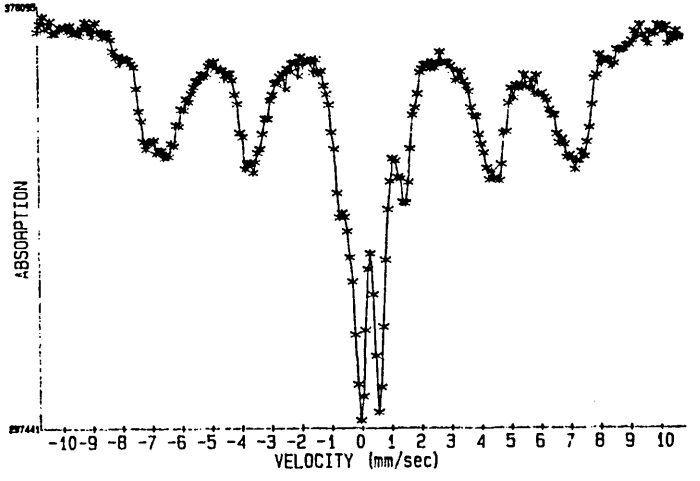

Spectrum 30

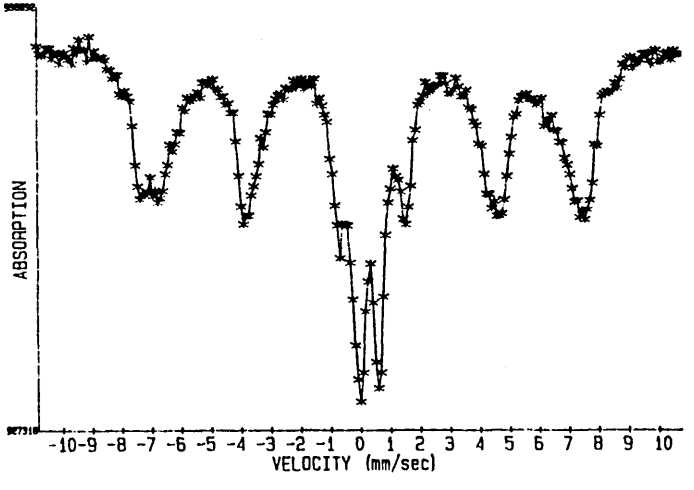

Spectrum 31

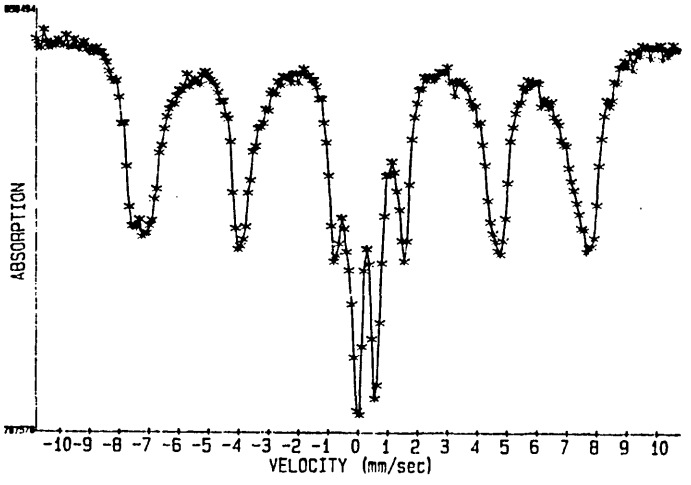

Spectrum 32

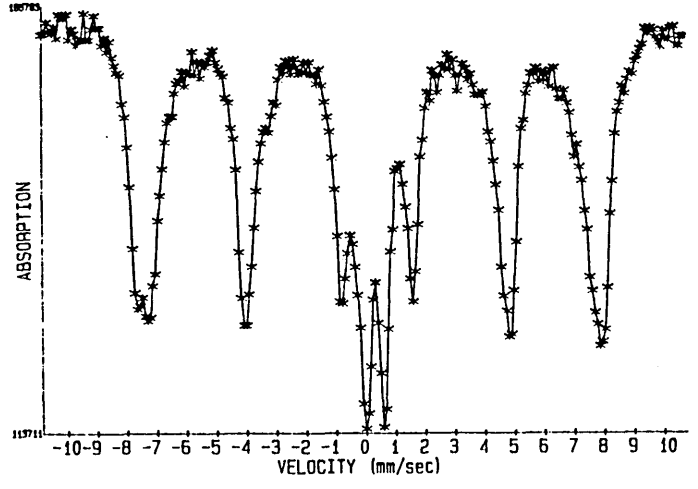

Spectrum 33

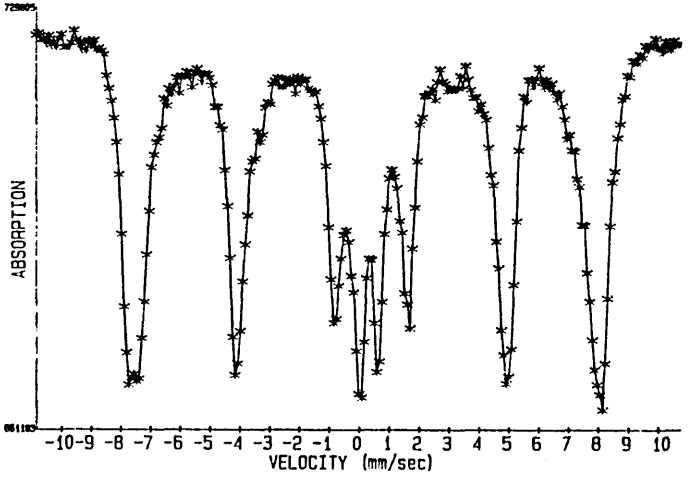

Spectrum 34

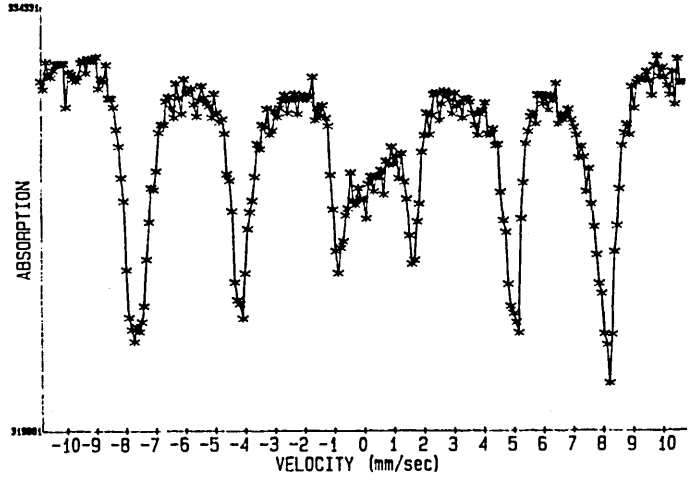

Spectrum 35

WALL TIE CORRN. PRODUCT T=25K SCT228T

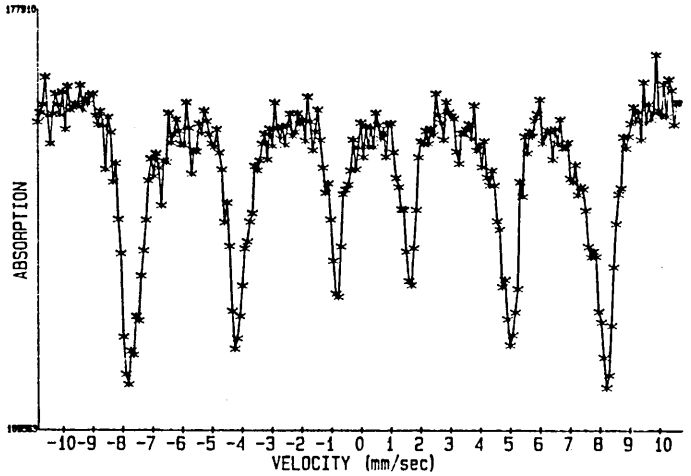

Spectrum 36

WALL TIE COORN. PRODUCT T=12K SCT226

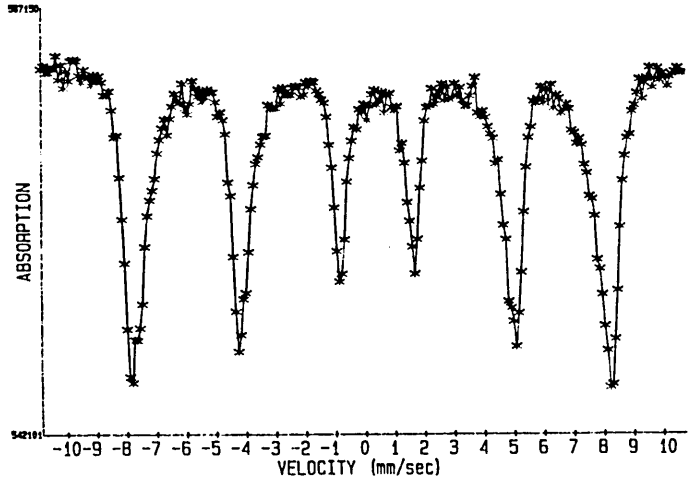

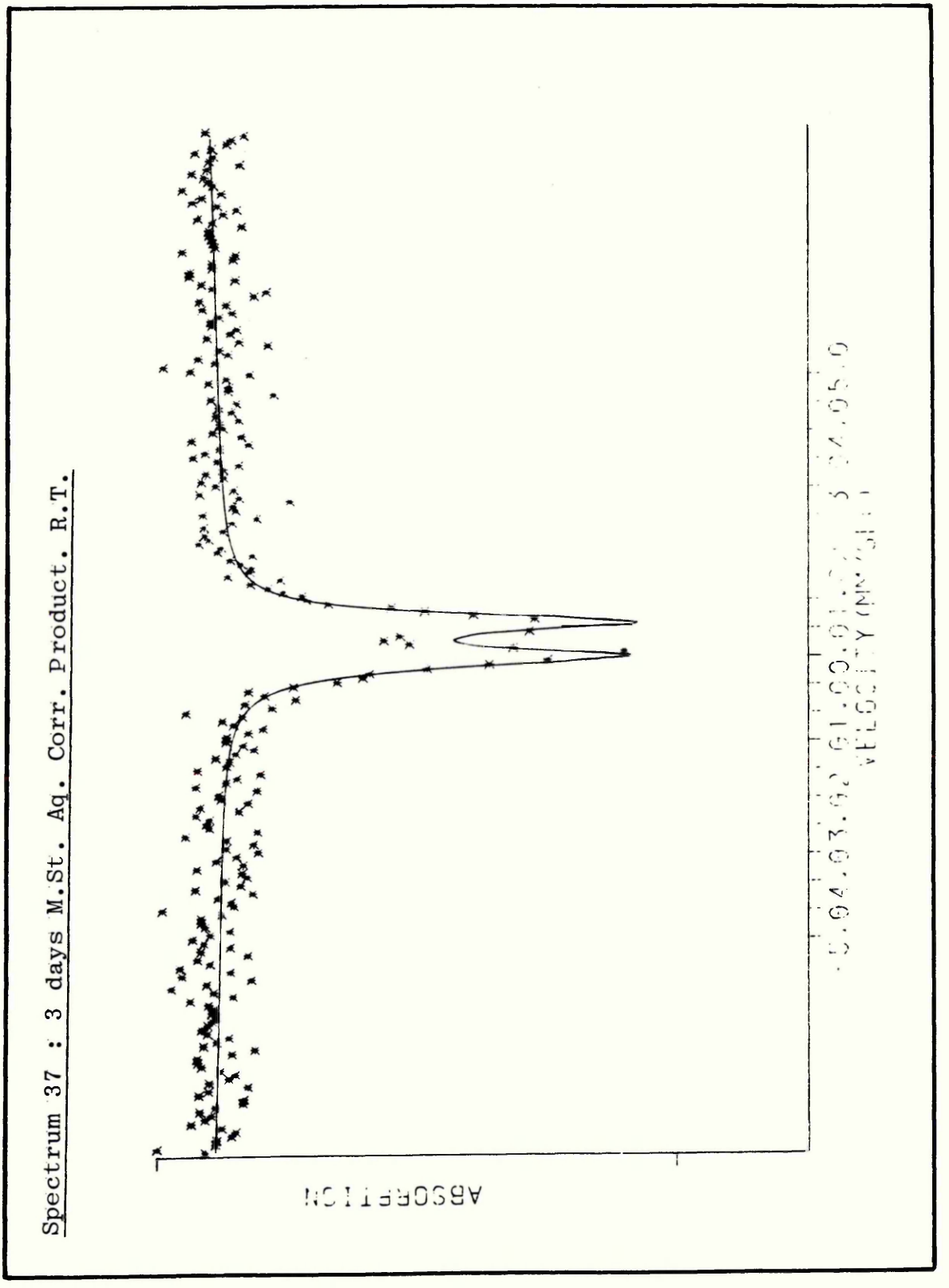

Spectrum 37 : 3 days M.St. Aq. Corr. Product. R.T.

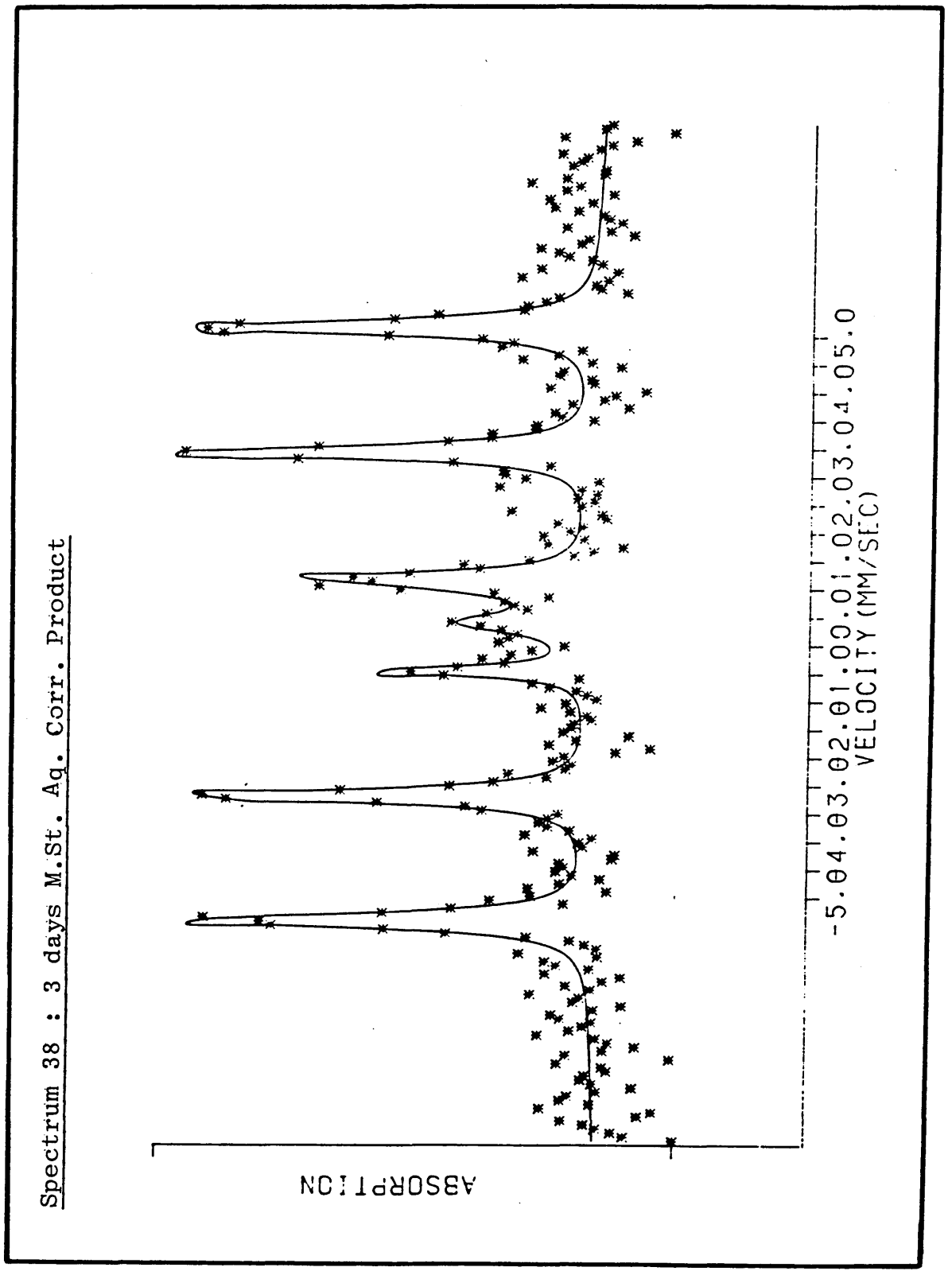
Spectrum 38 : 3 days M.St. Aq. Corr. Product
ABSORPTION
-5.0 4.0 3.0 2.0 1.0 0.0 1.0 2.0 3.0 4.0 5.0
VELOCITY (MM/SEC)

Spectrum 39 : 30 days M. St. Aq. Corr. Product

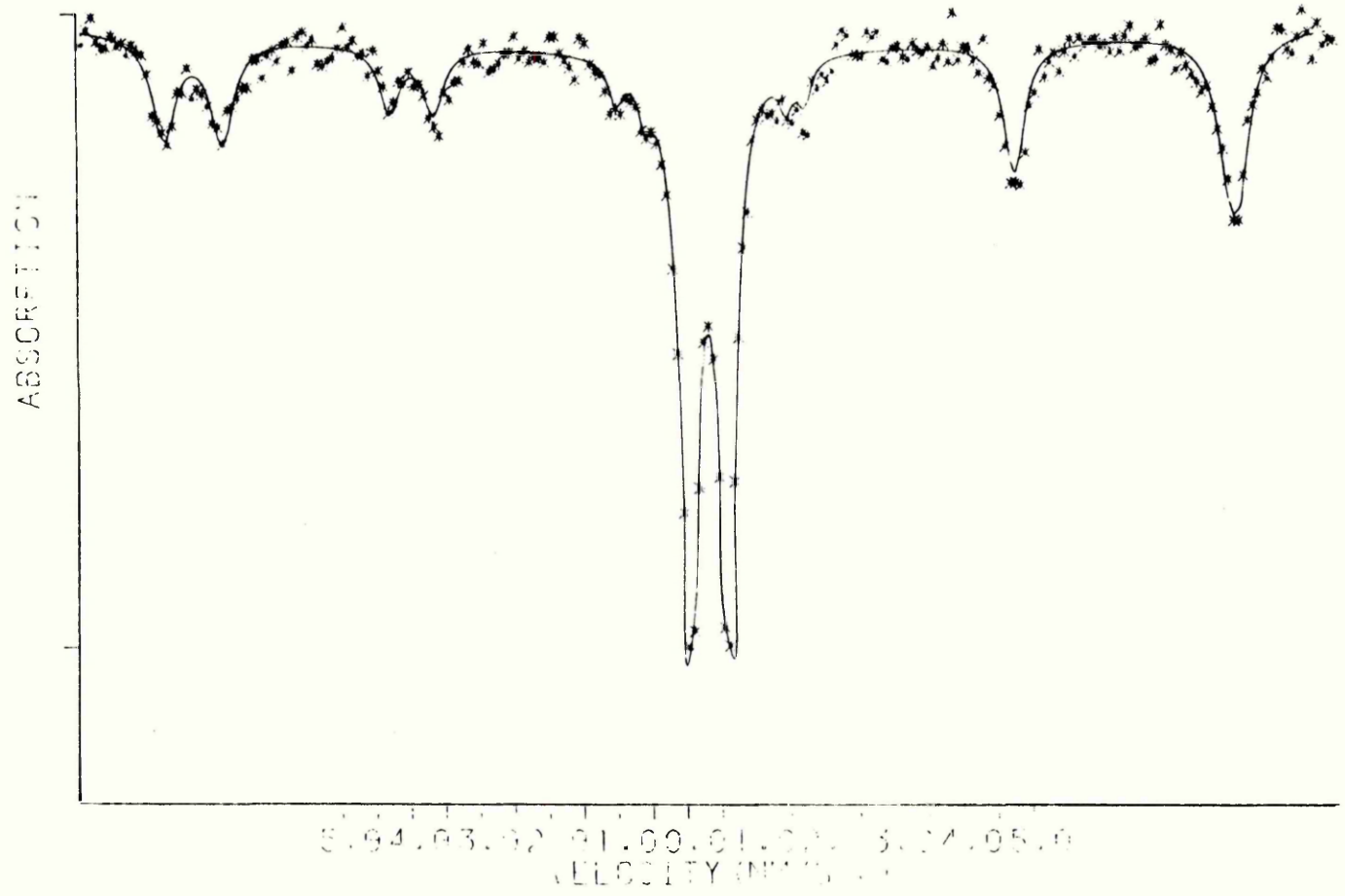

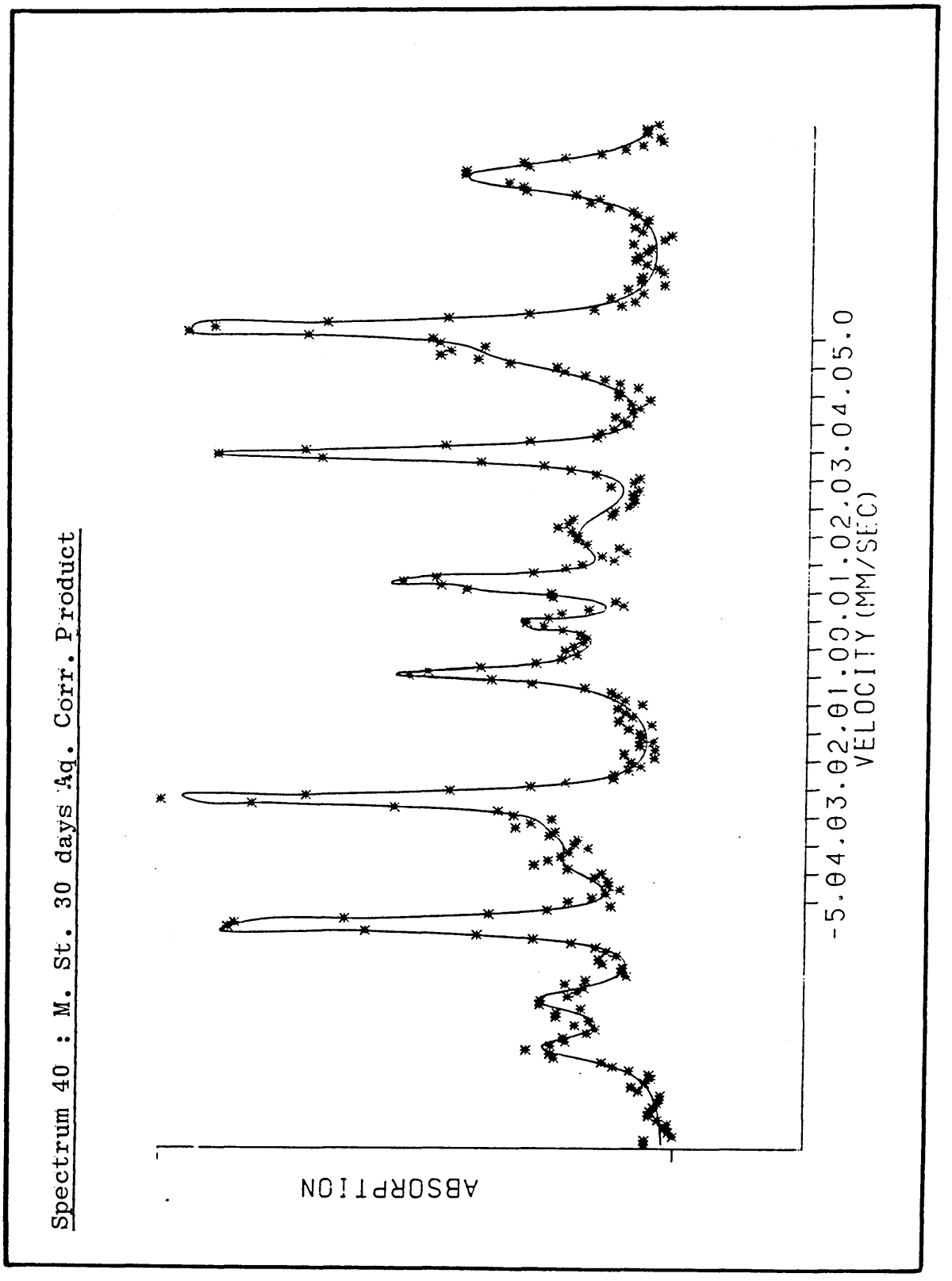
Spectrum 40 : M. St. 30 days Aq. Corr. Product
ABSORPTION
-5.0 4.0 3.0 2.0 1.0 0.0 1.0 2.0 3.0 4.0 5.0
VELOCITY (MM/SEC)

Spectrum 41 : M. St. Aq. Corr. Product 200 Days (Room Temperature)

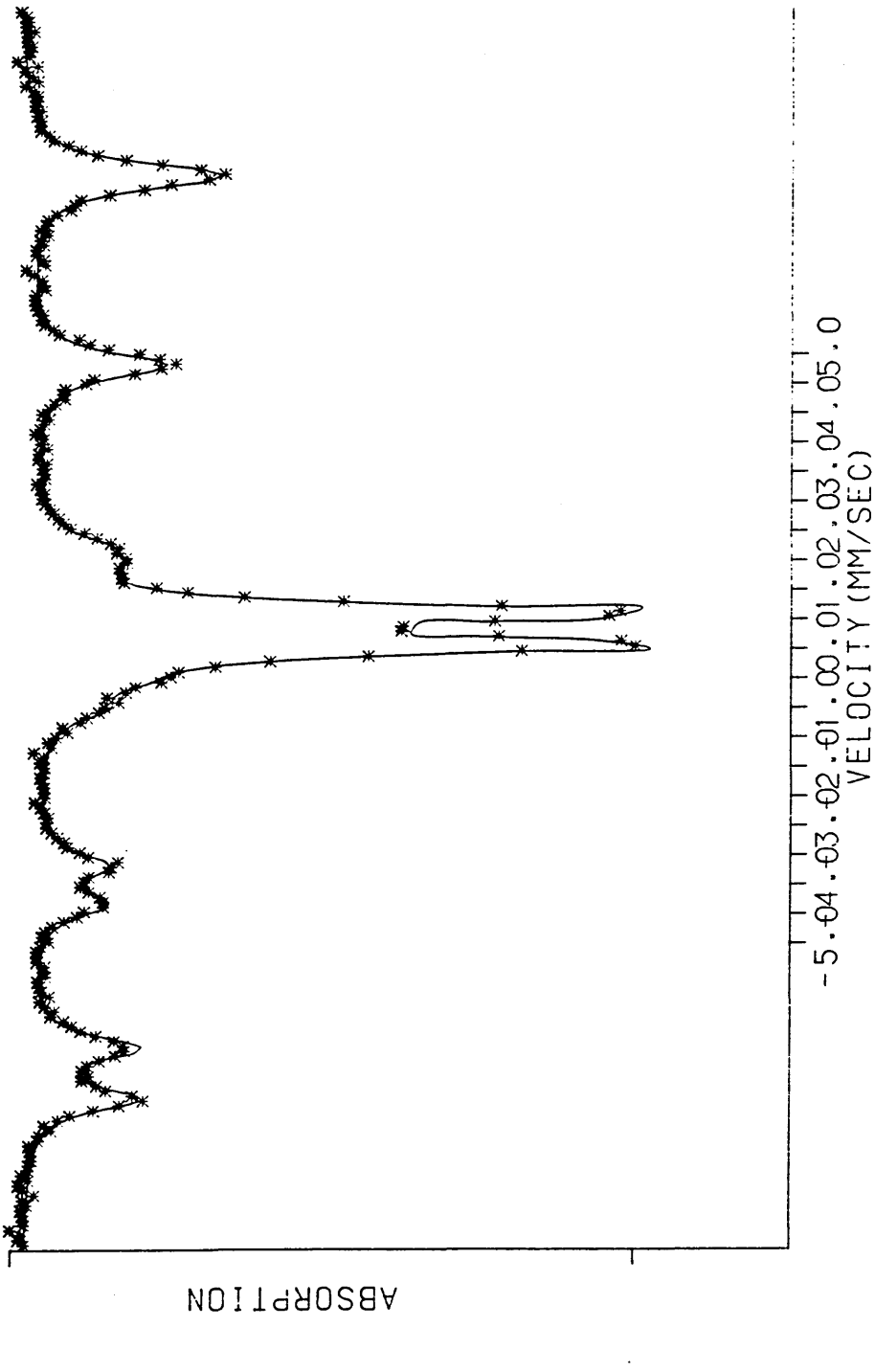

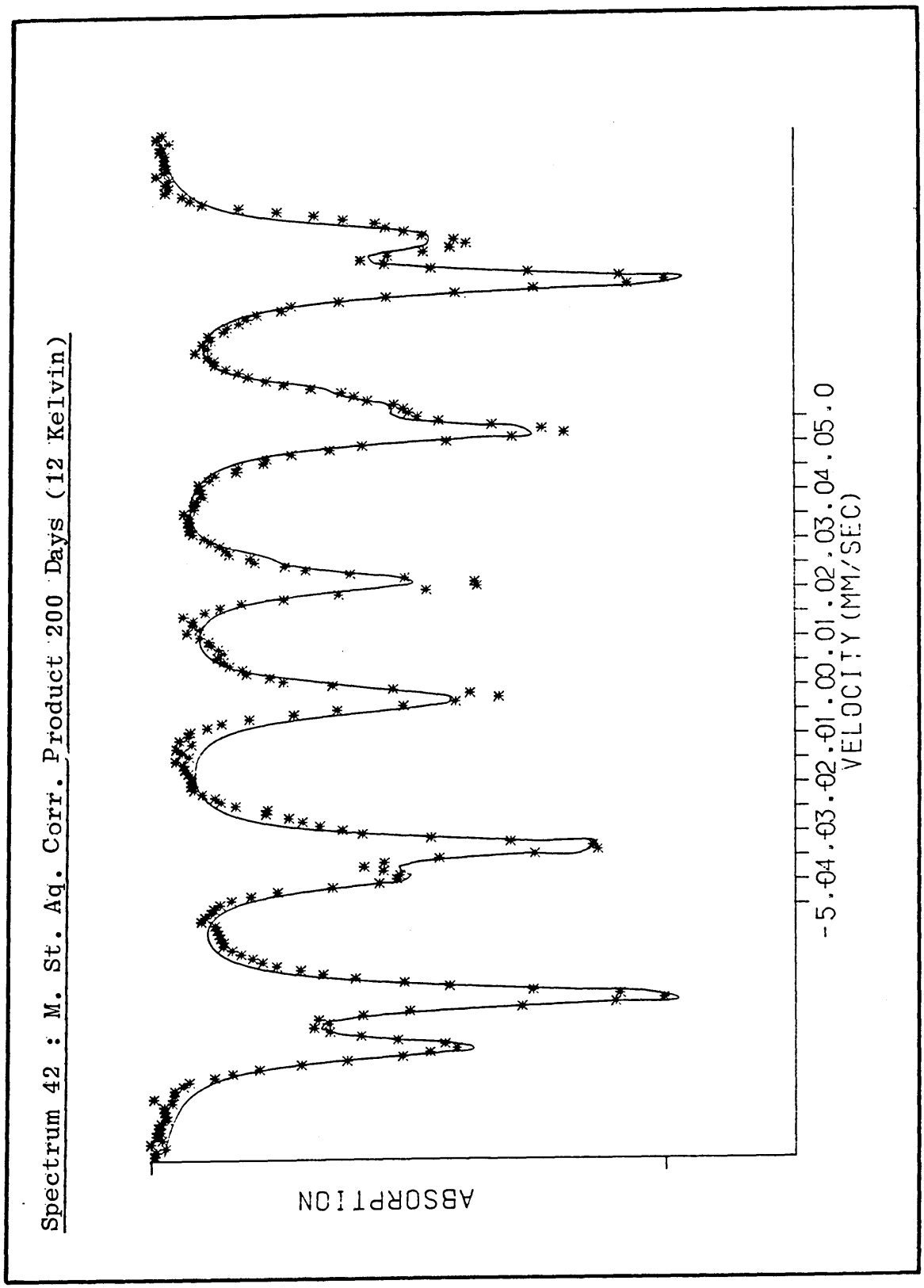
Spectrum 42 : M. St. Aq. Corr. Product 200 Days (12 Kelvin)
ABSORPTION
-5.0 -4.0 -3.0 -2.0 -1.0 0.0 1.0 2.0 3.0 4.0 5.0
VELOCITY (MM/SEC)

Spectrum 43 : M. St. Aq. Corr. Product 200 Days

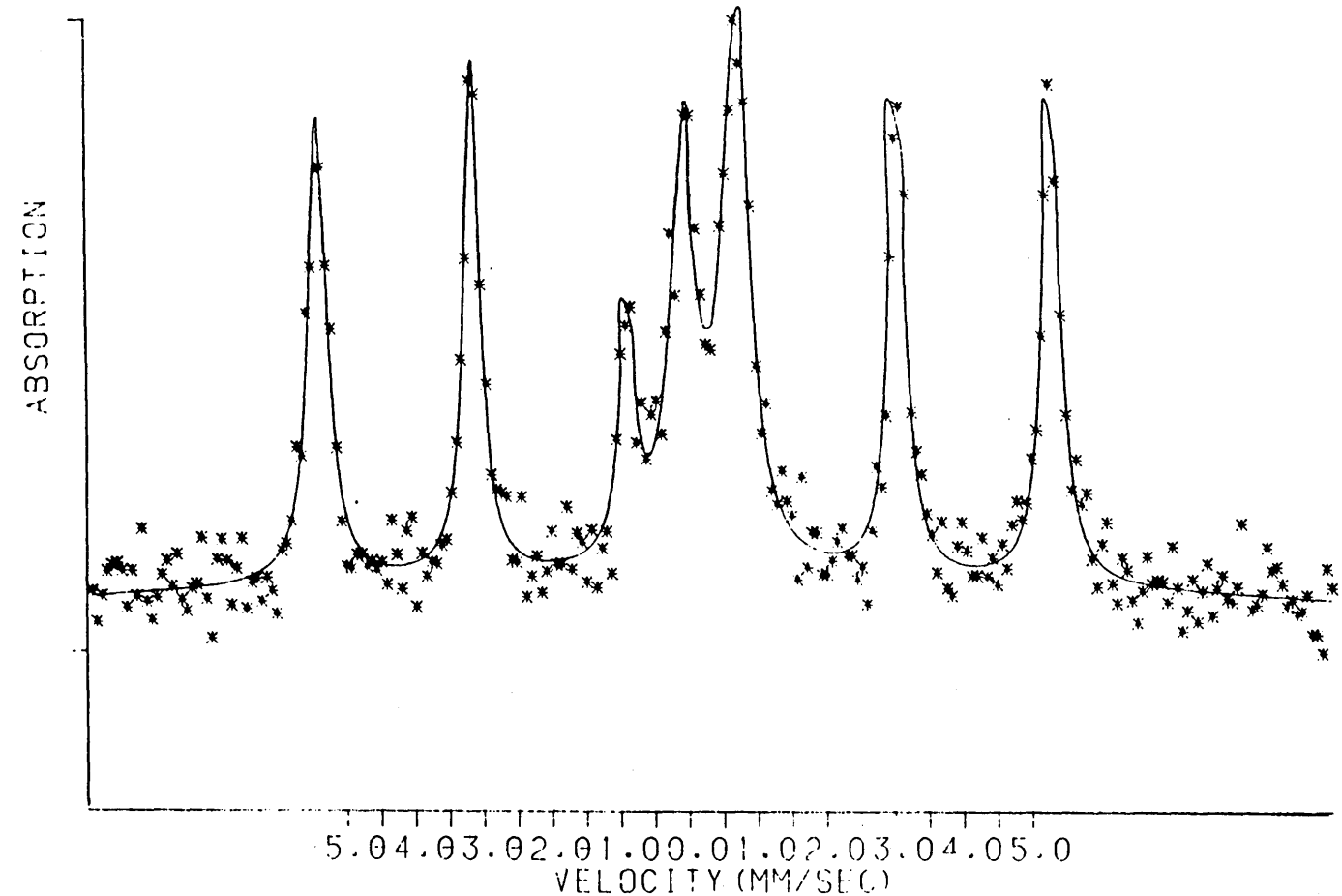

Aq. Corr. Product 200 Days

Displex Variable Temperature Run

Spectrum 44

SCT263T WET CORROSION PRODUCT T=293K

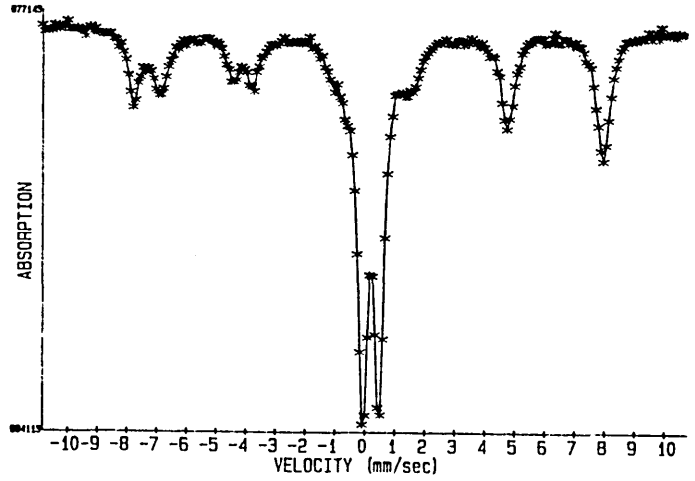

Spectrum 45

SCT272T WET CORROSION PRODUCT T=200K

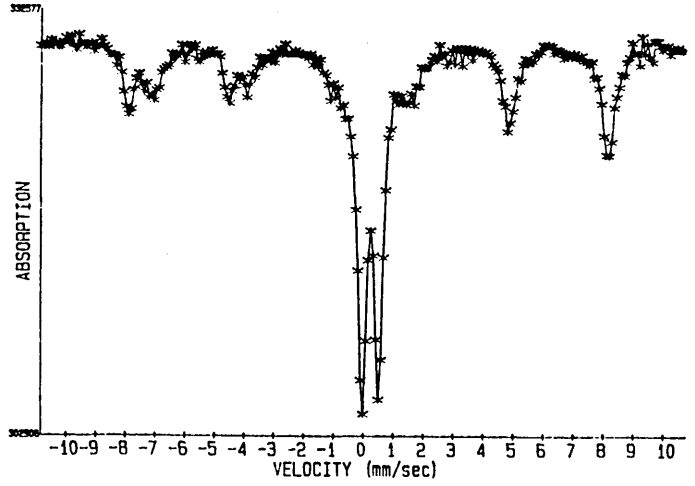

Spectrum 46

SCT271T WET CORROSION PRODUCT T=175K

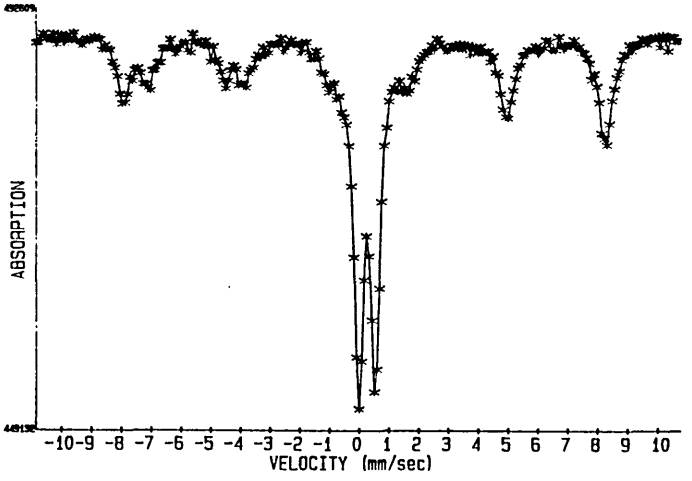

Spectrum 47

SCT270T WET CORROSION PRODUCT T=150K

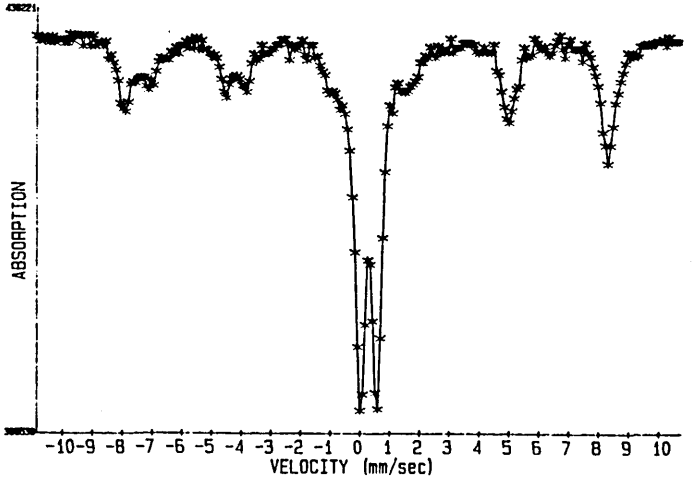

Spectrum 48

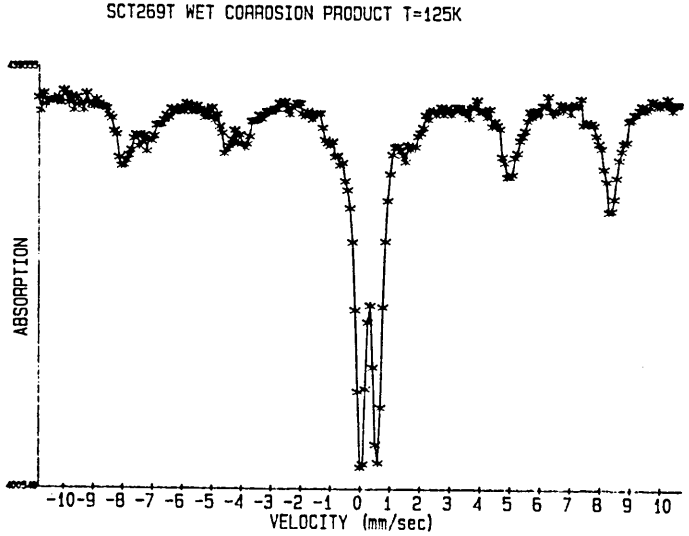

Spectrum 49

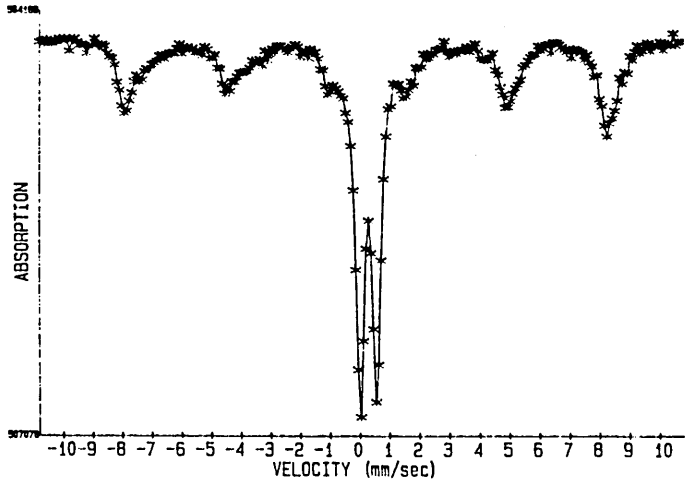

Spectrum 50

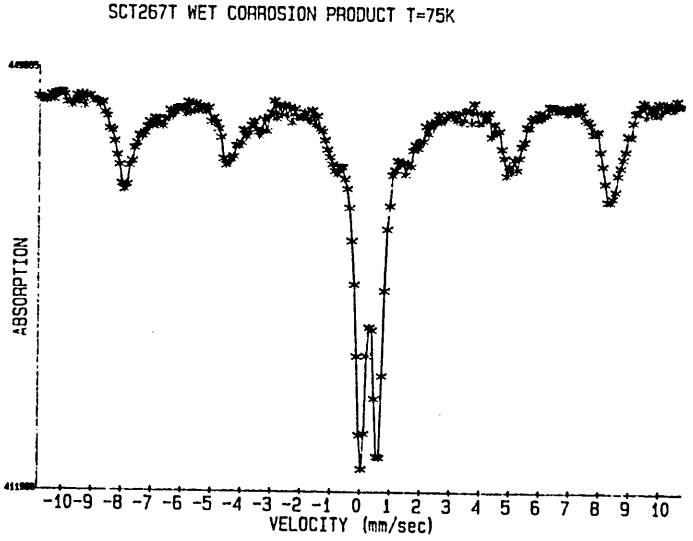

Spectrum 51

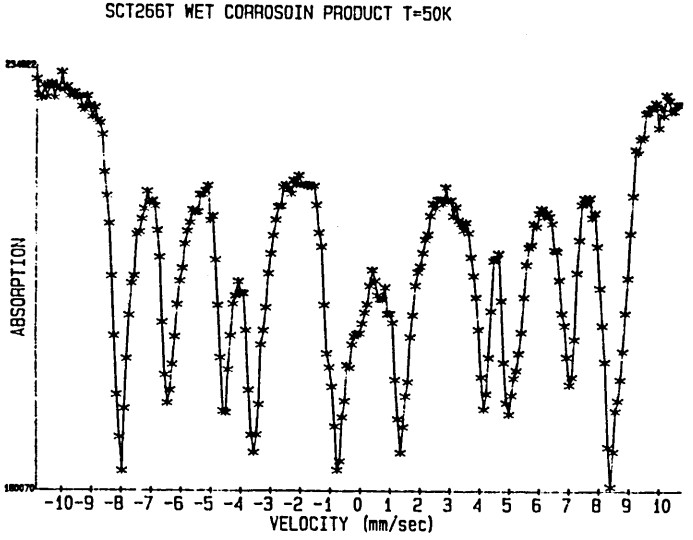

Spectrum 52

SCT265T WET CORROSION PRODUCT T=25K

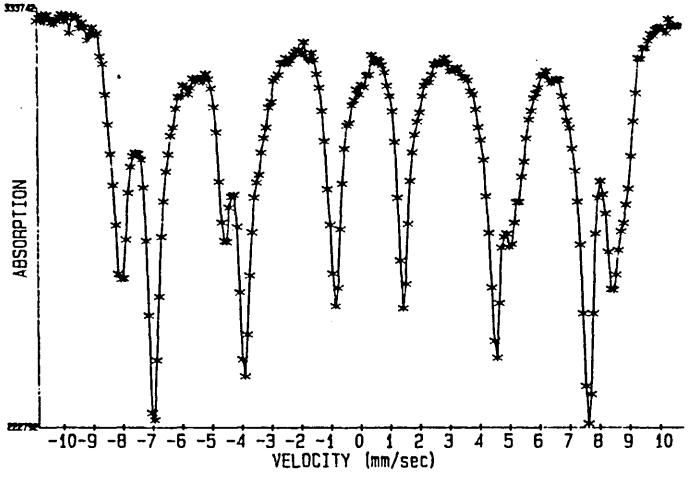

Spectrum 53

SCT264T WET CORROSION PRODUCT T=12K

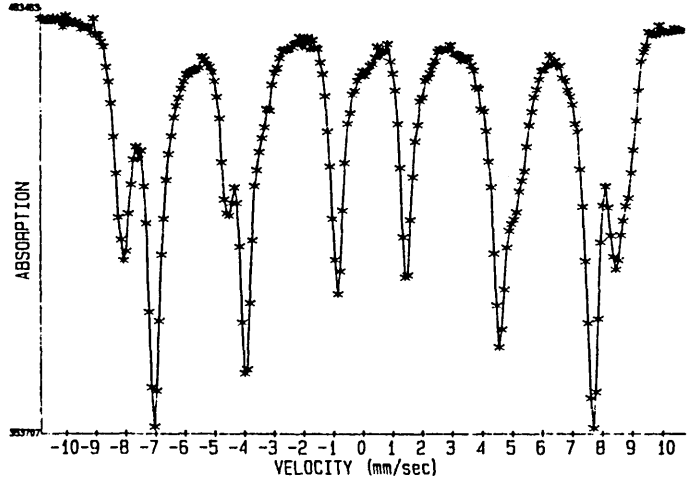

REFERENCES

1. N. N. Greenwood, T. C. Gibb, in Mössbauer Spectroscopy, Chapman and Hall, London, 1971.

2. F. Van der Woude, Phys. Stat. Solidi, 17, p 417, 1966.

3. F. J. Morin, Phys. Rev., 78, p 819, 1950.

4. E. J. W. Verwey, Nature, 144, p 327, 1939.

5. E. J. W. Verwey, P. W. Haaymaan, Physica, 8, p 979, 1941.

6. E. J. W. Verwey, P. W. Haaymaan, F. C. Romenijn, J. Chem. Phys., 15, p 181, 1947.

7. W. C. Hamilton, Phys. Rev., 110, p 1050, 1958.

8. S. K. Bannerjee, W. O'Reilly, C. E. Johnson, J. App. Phys., 38, 3, p 1289, 1967.

9. G. A. Sawatzby, J. M. D. Coey, A. H. Morrish, J. Appl. Phys., 40, p 1402, 1969.

10. B. J. Evans, S. S. Hafner, J. Appl. Phys., 40, p 1411, 1969.

11. R. S. Hargrove, W. Kündig, Solid State Commun., 8, p 303, 1970.

12. M. Rubenstein, D. W. Forester, Solid State Commun., 9, p 1675, 1971.

13. S. Mørup, J. A. Dumesic, H. Topsøe in: Applications of Mössbauer Spectroscopy, Vol. 2, edited by R. L. Cohen, Academic Press, New York, 1980.

14. J. B. Forsyth, I. G. Hedley, C. E. Johnson, J. Phys C Series 2, 1, p 179, 1968.

15. D. G. Chambaere, E. De Grave, J. Magn. Magn. Mats., 44, p 349, 1984.

16. A.S.T.M. Search Manual, Powder Diffraction File, Hanawatt Method Search Manual, Inorganic Compounds, 1977.

17. D. G. Chambaere, E. De Grave, Phys. Stat. Sol. (a) S3, p 93, 1984.

18. W. Meisel, Private Communication, 26th Meeting of the Mössbauer Discussion Group, University of East Anglia, Norwich, England, July 1985.

19. S. C. Thorpe, Report No 1, Department of Applied Physics, Sheffield City Polytechnic, 1983.

20. T. Misawa, K. Asami, K. Hashimoto, S. Shimodaira, Corrosion Science, 14, p 279, 1974.

21. C. E. Johnson, J Phys. C. Ser. 2, 2, p 1996, 1969.

22. E. Murad, U. Schwertmann, Mineralogical Magazine, 48, p 507, 1984.

23. O. C. Kistner, A. W. Sunyar, Phys. Rev. Lett., 4, p 412, 1960.

24. W. Kündig, H. Bömmel, G. Constabaris, R. H. Lindquist, Phys. Rev., 142, p 327, 1966.

25. R. J. Armstrong, A. H. Morrish, G. A. Sawatzky, Phys. Lett., 23, No 7, p 414, 1966.

26. K. Haneda, A. H. Morrish, Phys. Lett., 64A, p 259, 1977.

27. B. J. Evans, S. S. Hafner, J. Appl. Phys., 40, No 3, p 1411, 1969.

28. D. G. Chambaere, E. De Grave, R. L. Vanleerberghe, R. E. Vandenberghe, Hyperfine Interactions, 20, p 249, 1984.

29. L. H. Bowen, Mössbauer spectroscopy of ferric oxides and hydroxides in, Mössbauer Effect Data Journal, 2, p 76, 1979.

30. I. Dézsi, L. Keszthelyi, D. Kulgawczuk, B. Molnar, N. A. Eissa, Phys Stat. Solidi, 22, p 617, 1967.

MOSSBAUER PARAMETERS FOR SOME IRON OXIDES AND OXYHYDROXIDES

Absorber	T/K	δ(Fe)/mms^{-1}	Quadrupole Interaction /mms^{-1}	H_{INT}/kG	Reference
α-Fe_2O_3	298	0.38	- 0.12	515	23
	83	-	0.18	542	24
	0	-	-	544	2
γ-Fe_2O_3	RT	0.27) 0.42)	-	488) 499)	25
	77	-	-	508) 525)	26
Fe_3O_4	298 (A)	0.25	0.00	493	27
	(B)	0.65	0.00	460	
	4.2 (Fe^{2+})	0.42	- 0.02	516	
	(Fe^{3+})	0.99	- 0.22	510	
α-FeOOH	RT	0.35	0.15	384	14
	4.2	-	0.15	504	
β-FeOOH	RT	0.37) 0.38)	0.53) 0.93)	- -	28
	12	0.50) 0.48)	- 0.05 - 0.11	490) 478)	15
γ-FeOOH	RT	0.30	0.55	-	22
	4.2	-	< 0.1	460	
δ-FeOOH	RT	0.38	0.48	-	29
	80	-	- 0.1	505) 525)	30

CHAPTER 5 : SURFACE CORROSION STUDIES

5.1 Conversion X-ray Mössbauer Spectroscopy

5.2 Surface Enrichment

5.3 Diffusion of ^{57}Fe

5.4 Laboratory Corrosion Tests

5.5 Surface Monitoring of Some Mild Steel Substrates

5.6 Spectra

References

CHAPTER 5 : SURFACE CORROSION STUDIES

A technique has been developed to probe beneath a protective layer such as a paint, varnish, grease or oil layer without the need to remove such a layer, thus eliminating the possibility of any chemical changes or loss of corrosion products occurring as a result of the removal of such a layer.

5.1 Conversion X-ray Mossbauer Spectroscopy

When a 5% Argon-Methane gas mixture is used in a gas flow proportional counter, conversion x-rays are detected rather than conversion electrons (Section 3.4.2). The greater escape depth [1] of the conversion x-rays allows a surface with such an applied layer to be successfully monitored. A conversion x-ray Mössbauer spectrum (C.X.M.S) is typically observed in a few hours, the exact time is dependent on the thickness of the applied layer. If the protective layer is sufficiently thin, a large proportion of the x-rays detected will originate from deep within the substrate and the resultant spectrum will be representative of the bulk rather than the surface of the sample. To enhance the surface sensitivity of the C.X.M.S. technique, the near surface region must be enriched in the isotope ^{57}Fe. To achieve this, ^{57}Fe was vacuum evaporated onto the surface of substrates and subsequently diffused into the near surface region. This had to be achieved without oxidising the substrate. C.E.M.S. and C.X.M.S. techniques were used to monitor the surface of the enriched annealed samples.

5.2 Surface Enrichment

The deposition of a thin surface layer was achieved by vacuum evaporation of ^{57}Fe from a tungsten boat using an Edwards E306 vacuum coating unit. The instrumental operating conditions are summarised in Table 5.1.

Mass ^{57}Fe/kg	Boat Type : Dimensions/mm	Vac/Torr	Power 30V L.T.
1.785×10^{-5}	W : 25 x 15 x 0.025	$< 4 \times 10^{-7}$	Set 3 8 burns Set 4 2 burns

Table 5.1 : Operating Conditions for the Edwards E306 Vacuum Coating Unit

Because of the very high cost of ^{57}Fe ($\sim$ £9,000 per gram), as many samples as possible were held in position around the tungsten boat for a single coating. The substrates, 25 x 10 mm pieces of mild steel, were held in place on a hemispherical grid of radius 10 cm. The mass of ^{57}Fe in the boat and the boat to substrate distance determined the evaporated layer thickness according to the relationship [2]:

$$m = \frac{t\ 8\ \pi\ r^2\ \rho}{3\ \sin\ \alpha}$$

where m = mass

t = thickness

r = radius = 0.1 m

ρ = density = 7,870 kg m^{-3}

$\alpha = 90°$ $\sin\ \alpha = 1$

The parameters above resulted in a maximum thickness of 27 nm, the actual thickness being less than this because some alloying between the ^{57}Fe and the tungsten boat occurred. Attempts were made to overcome this problem by first coating the boat with an inert aluminapaste. Unfortunately this had two detrimental effects. Firstly, the paste outgassed and cracked as the boat was heated, allowing alloying to occur, and secondly the extra heating required to vaporise the ^{57}Fe caused the boat to fail. The final method used an uncoated tungsten boat containing the iron foil which was quickly heated, using the 30 volt low tension power supply of the Edwards E306 vacuum coating unit at setting 3, maintained for a few seconds and then allowed to cool. This sequence was repeated eight times at which stage the thickness monitor of the Edwards unit indicated ^{57}Fe was no longer evaporating. The power was then increased to setting 4 and the sequence repeated a further two times; at this stage the tungsten boat failed. This procedure reduced alloying to a minimum [3]. In practice only 1.322×10^{-5} kg of ^{57}Fe was vaporised. The thickness of the deposited ^{57}Fe layer was therefore estimated to be approximately 20 nm. In preliminary experiments using natural iron foil, the above method resulted in the deposition of a thin film of iron on to a glass slide held 0.1 metres from the iron containing tungsten boat. The presence of iron and the absence of tungsten on the glass slide was confirmed using the energy dispersive analysis of X-rays (EDAX) detection

system on a Philips 500 scanning electron microscope.

5.3 Diffusion of ^{57}Fe

The surface enriched samples were then annealed to allow the evaporated layer of ^{57}Fe to diffuse into the near surface region of the mild steel substrate (back diffusion of the substrate into the ^{57}Fe layer will also occur) and thus produce a mild steel substrate in which the near surface region is rich in the Mössbauer isotope ^{57}Fe. The surface sensitivity of the C.X.M.S. technique was thus increased and enabled surface corrosion products to be observed on substrates to which a protective coating of thickness 10-20 μm had been applied.

The use of fluorescent x-rays was necessary to penetrate the protective layer applied to the mild steel samples. Without surface enrichment, the C.X.M.S. technique would not have been sufficiently surface sensitive to detect the early stages of corrosion. The maximum escape depth of the conversion x-ray in mild steel is approximately 10 μm making them characteristic of the bulk rather than the surface under normal conditions.

By combining the effects of the absorption of the conversion x-ray in the applied protective layer with surface enrichment of ^{57}Fe, the surface sensitivity of the C.X.M.S. technique has been enhanced.

5.3.1 Diffusion Model

A simple diffusion model to enable the depth profile of the surface deposited ^{57}Fe to be modelled as a function of annealing conditions has been developed in the Department of Applied Physics, Sheffield City Polytechnic [4].

In the model it was assumed that a uniform layer of ^{57}Fe is deposited onto the mild steel substrate, and that under controlled conditions in an oxygen-free environment the ^{57}Fe is diffused into the bulk. Diffusion will also occur from the bulk into the deposited layer.

The diffusion equation [5] may be written as:

$$\nabla^2 F = \frac{1}{D} \frac{\partial F}{\partial t} \qquad (5.1)$$

where F is the fractional concentration of ^{57}Fe (F = 1 equivalent to 100% ^{57}Fe) and D the Diffusion Rate can normally be expressed as:

$$D = D_o \exp \left\{ - \frac{Q}{RT} \right\} \qquad (5.2)$$

where Q is the Activation Energy, R the Gas Constant and T the Absolute Temperature.

If we consider a one-dimensional model (5.1) can be rewritten as:

$$\frac{\partial^2 F}{\partial x^2} = \frac{1}{D} \frac{\partial F}{\partial t} \qquad (5.3)$$

This can be reduced to a dimensionless equation by the usual substitution.

$$x = ld \qquad [l < 1]$$

and $$\tau = \frac{Dt}{d^2} \tag{5.4}$$

The dimensions are defined in Figure 5.1.

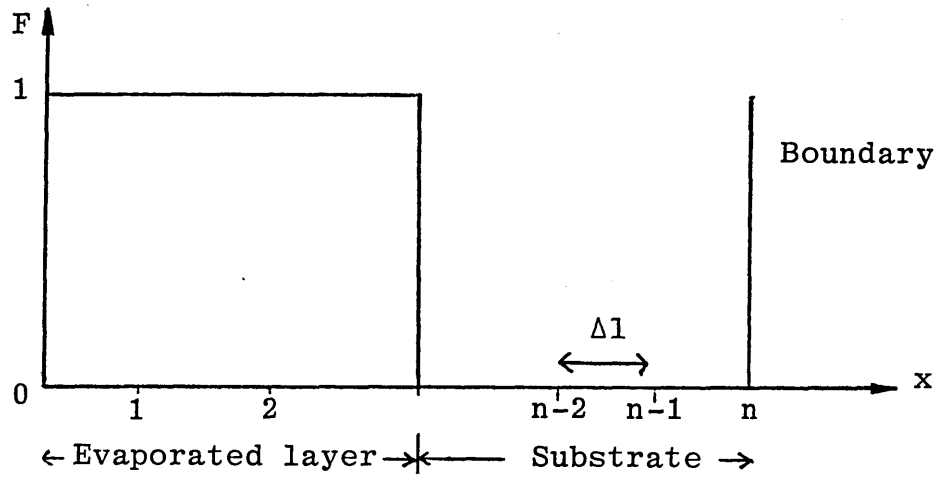

Figure 5.1 : Definition of the Dimensions Used in the Diffusion Model

Hence $$\frac{\partial^2 F}{\partial l^2} = \frac{\partial F}{\partial \tau} \tag{5.5}$$

This differential equation is solved by standard iterative net methods subject to boundary conditions. We define the concentration at time τ to be $F_o - F_n$, and evaluated the concentration at time $\tau + \Delta\tau$ $G_o - G_n$. The standard iterative net approach leads to

$$\frac{\partial^2 F}{\partial l^2} = \frac{F(i+1) - 2F(i) + F(i-1)}{\Delta l^2}$$

$$\frac{\partial F}{\partial \tau} = \frac{G(i) - F(i)}{\Delta \tau}$$

Thus $G(i) = \frac{\Delta\tau}{(\Delta l)^2} \left\{F(I+1) - 2F(i) + F(i-1) + F(i)\right\}$ (5.6)

This allows G_1 to G_{n-1} to be calculated subject to the Boundary Conditions for G_o and G_n. A computer program was written (Figure 5.2) for 51 net points (50 spaces).

For stability it is necessary for $\frac{\Delta\tau}{(\Delta l)^2} < \frac{1}{2}$

Selecting $\Delta\tau = 10^{-4}$ gives

$$\frac{\Delta\tau}{(\Delta l)^2} = R^2\Delta\tau = \frac{2,500}{10,000} = 0.25$$

which satisfies the stability condition.

5.3.2 Lattice Self Diffusion in Iron

The lattice self-diffusion in iron has been reviewed by Okawa [6]. Above the Curie Point, the diffusion rate can be written as

$$D = D_o \exp\left\{-\frac{Q}{RT}\right\}$$

with the following values:

$R = 8.31$ Joule mol^{-1} K^{-1}

bcc iron

$$D_o = 2.00 \begin{matrix} + 0.23 \\ - 0.21 \end{matrix} \times 10^{-4} \text{ m}^2 \text{ s}^{-1}$$

$$Q = 2.409 \pm 0.012 \times 10^5 \text{ Joule mol}^{-1}$$

for the temperature range $1809K < T < 1032K$

In the ferromagnetic region ($T < 1043K$)

$$D_{\alpha f} = D_{o\alpha p} \exp\left[-Q_{\alpha p}(1 + \alpha s)/RT\right]$$

```
LIST
  10DIMF(51)
  20DIMG(51)
  30INPUT K
  40FOR I=1 TO K
  50F(I)=1
  60NEXT I
  70FOR I=K+1 TO 50
  80F(I)=0
  90NEXT I
  100DELT=0
  110SUM=0
  120F(51)=0
  130FOR I=2 TO 50
  140G(I)=0.25*(F(I+1)-2*F(I)+F(I-1))+F(I)
  150SUM=SUM+G(I)
  160NEXT I
  170G(1)=K-SUM
  180DELT=DELT+0.0001
  190PRINT
  200@%=&40409
  210MODE7
  220CLS
  230PRINT "DELT=";DELT
  250PRINT"*******************************************
  260FOR L=1 TO 50
  270@%=&20208
  280PRINT G(L);
  290NEXT L
  300IF DELT>0.001 THEN 400
  310FOR I=1 TO 50
  320F(I)=G(I)
  330NEXT I
  350GOTO 110
  400 *FX5,2
  401 *FX8,4
  403 *FX6
  404 VDU2
  405 @%=40409
  406 PRINT"DELT=";DELT
  407 PRINT"G(I)"
  410 FORJ=0 TO 50
  420 PRINT G(J)
  430 NEXT J
  435 VDU3
  440 END
```

Figure 5.2 : Diffusion Model Computer Program Run on a BBCB Microcomputer

The parameters at 800K and 900K and the determined values of $D_{\alpha f}$ are shown in Table 5.2

T/K	α	s^2	$D_{\alpha f}/m^2\ s^{-1}$
800	0.22	0.63	2.8×10^{-22}
900	0.22	0.49	7.3×10^{-20}

Table 5.2 : Self-Diffusion in Iron; Evaluation of Diffusion Rate

The computer program evaluates the fractional concentration, F, at each net point per iteration of unit time $\Delta\tau$. This is related to real time by the expression

$$\Delta\tau = \frac{D\Delta t}{d^2}$$

If we assume a 20 nm layer of ^{57}Fe and equate this to 5 net points, then the total number of 50 net points define a thickness of 200 nm. This yields the real-time values shown in Table 5.3.

T/K	$D_{\alpha p}/m^2\ s^{-1}$	d/m	Δt/secs per iteration
800	2.8×10^{-22}	2×10^{-7}	1.4×10^{4}
900	7.3×10^{-20}	2×10^{-7}	55

Table 5.3 : Real Time per Iteration

Figure 5.3 shows the variation with depth of the fractional concentration after 10, 50 and 100 iterations. We see that after 100 iterations (of unit time Δt), the surface concentration has reduced to 0.5 while as a depth of 60 nm it has increased to approximately 0.1. This was felt to be an appropriate level of surface enrichment. At 800K 100 iterations would correspond to 397 hours, clearly not practical. At 900K it is approximately 1 minute per iteration and so a diffusion time of 100 minutes would be appropriate.

Ideal annealing conditions were therefore:

Temperature = 900K
Surface layer = 20 nm ^{57}Fe
Annealing time = 100 minutes

5.3.3 Experimental Annealing Conditions

The first attempt to anneal samples with a layer of ^{57}Fe evaporated onto the surface was in an argon atmosphere tube furnace at 900K. Argon at 2 $dm^3\ min^{-1}$ continuously flowed over the samples as they were annealed and as they were removed to a cool part of the tube furnace. When the cooled samples were removed from the furnace, it was apparent that the samples had oxidised as the previously bright lustre of the metal surface was now a dark matt brown colour. The C.E.M. and C.X.M. spectra of this sample were recorded. The C.E.M. spectrum is dominated by lines due to the common oxides of iron, haematite α-Fe_2O_3 and magnetite Fe_3O_4, (Spectrum 54E).

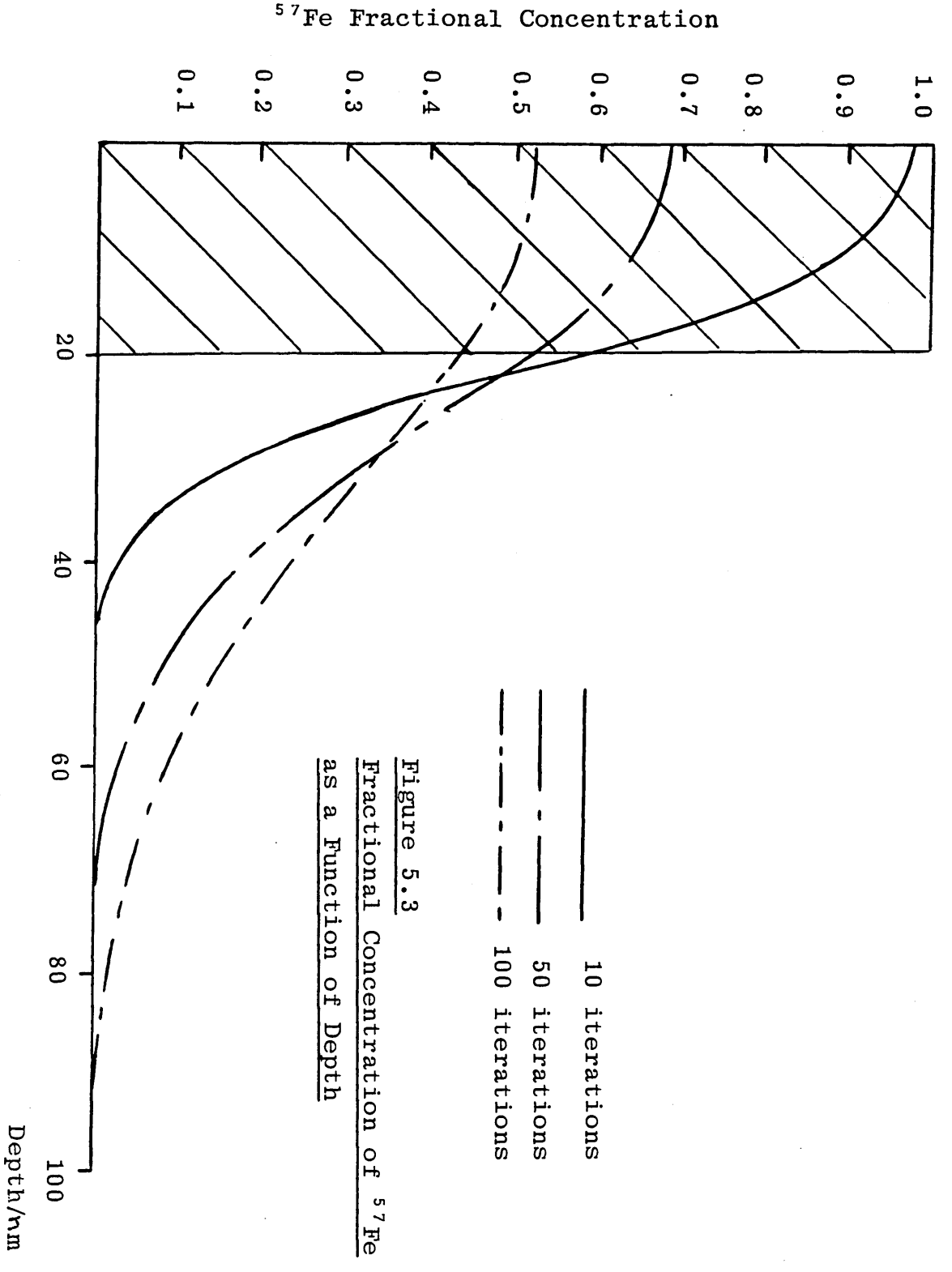

Figure 5.3
Fractional Concentration of ^{57}Fe as a Function of Depth

A contribution from the substrate is observed in regions where it is not swamped by the oxides. The C.X.M. spectrum is dominated by the 6 line pattern of the mild steel substrate (Spectrum 55X) with a small contribution from the oxides. Comparison of these two spectra gives an indication of the surface sensitivity of the C.E.M.S. technique.

Further samples were sealed in silica glass phials under vacuum and under 1 atm pressure of argon at ambient temperature. These samples were annealed at 900K for 100 minutes in a muffle furnace. Both samples had oxidised during the annealing process. The C.E.M. and C.X.M. spectra of the samples sealed under vacuum (Spectra 56E and 57X respectively) reveal a doublet typical of Fe^{3+} in addition to the substrate lines. Very similar spectra (58E and 59X) are obtained from the samples sealed under argon. The intensity of the doublet is reduced in this case. The data relating to the samples which oxidised during annealing are summarised in Table 5.4.

A successful annealing procedure was finally achieved. The underside of the substrate was recleaned (no ^{57}Fe enrichment on this side), the sample was then placed in a silica glass phial with a freshly polished piece of titanium metal which acted as an oxygen scavenger and preferentially oxidised. The phial was sealed under 1 atmosphere of argon at room temperature, Figure 5.4.

Spectrum*	Component	δ(Rh)/mms^{-1}	δ(Fe)/mms^{-1}	Quadrupole Interaction /mms^{-1}	H_{INT}/kG
54E	Fe	- 0.11	0.00	-	330
	α-Fe_2O_3	0.26	0.37	ε = 0.12	513
	Fe_3O_4	0.16(A)	0.27(A)	ε = 0.00	491(A)
		0.55(B)	0.66(B)	ε = 0.00	459(B)
55X	Fe	- 0.12	- 0.01	-	330
	α-Fe_2O_3	0.26	0.37	ε = 0.12	513
	Fe_3O_4	0.16(A)	0.27(A)	ε = 0.00	491(A)
		0.55(B)	0.66(B)	ε = 0.00	459(B)
56E	Fe	- 0.11	0.00	-	331
	Fe^{3+}	0.25	0.36	Δ = 0.73	-
57X	Fe	- 0.11	0.00	-	332
	Fe^{3+}	0.26	0.37	Δ = 0.73	-
58E	Fe	- 0.12	- 0.01	-	329
	Fe^{3+}	0.22	0.33	Δ = 0.67	-
59X	Fe	- 0.11	0.00	-	330
	Fe^{3+}	0.23	0.34	Δ = 0.70	-

Table 5.4 : Mössbauer Parameters for ^{57}Fe Enriched Mild Steels which Oxidised During Annealing

*The letters E and X refer to electron and x-ray spectra respectively.

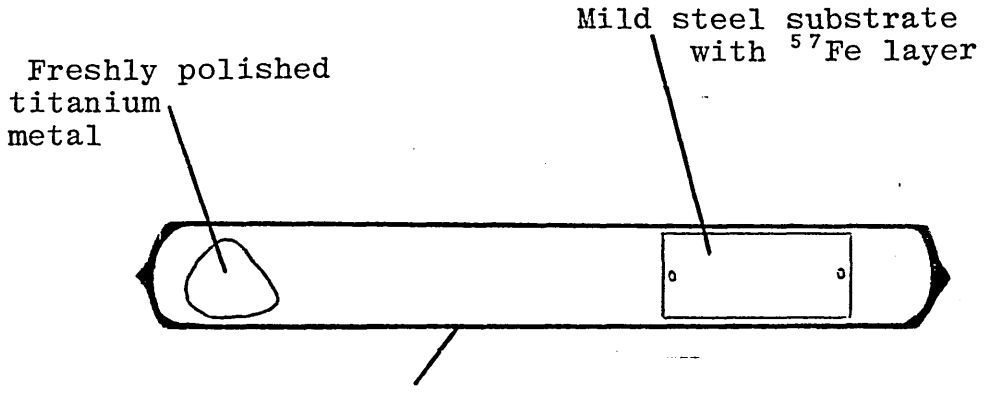

Figure 5.4 : Sealed Glass Phial Showing the Mild Steel Substrate and Titanium Oxygen Scavenger (Actual Size)

The phials were annealed in a muffle furnace as previously described. On cooling the mild steel surface remained bright, the titanium metal surface had a distinct blue colour suggesting some oxidation of the titanium had occurred. The C.E.M. and C.X.M. spectra of this sample were recorded (Spectra 60E and 61X respectively), both reveal the six line pattern of the substrate only. Similarly prepared samples were coated with a paint layer (Spectrum 62X) and a varnish layer (Spectra 63X) and the C.X.M. spectra recorded. Collection times for these spectra were approximately 90 hours. The data is summarised in Table 5.5. The rather poor quality of the spectrum obtained from the painted sample (Spectrum 62X) was due to the paint system containing a zinc chromate corrosion inhibitor which acted as a filter to the ^{57}Fe conversion X-ray. Further work therefore concentrated on

Spectrum	Coating	δ(Rh)/mms^{-1}	δ(Fe)/mms^{-1}	H_{INT}/kG
60E	None	- 0.11	0.00	330
61X	None	- 0.11	0.00	330
62X	Paint	- 0.12	- 0.01	329
63X	Varnish	- 0.12	- 0.01	331

Table 5.5 : Mössbauer Parameters for Successfully Annealed Surface Enriched Mild Steel

samples protected by applied varnish layers. The thickness of such a varnish layer was determined using a Rank Taylor-Hobson Talysurf 5 system [7]. The vertical magnification was x 1000. The varnish layer thickness was determined as approximately 10 μm. A typical Talysurf trace is given in Figure 5.5.

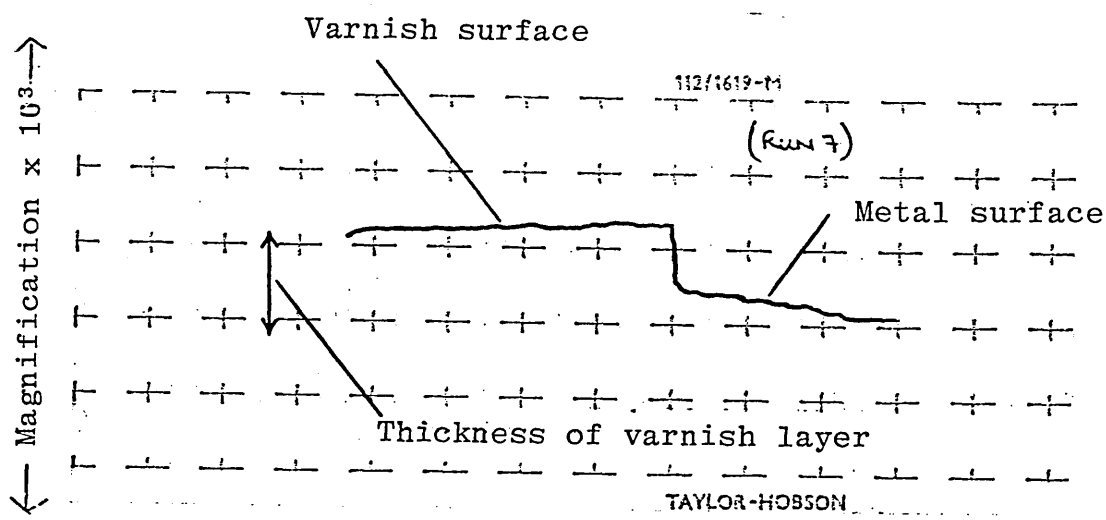

Figure 5.5 : A Typical Talysurf Trace as used to Determine the Thickness of an Applied Varnish Layer

5.4 Laboratory Corrosion Tests

Similarly coated samples were then prepared and subsequently exposed to two aggressive atmospheres:

(i) A continuous salt spray using a 3% sodium chloride solution at 21°C.

(ii) Suspended above a saturated solution of sulphur dioxide in water at 21°C.

After 72 hours exposure to the salt spray [8], a dull orange-brown corrosion product covering approximately 20% of the sample surface area was observed. In addition to the sextet attributable to the mild steel substrate, the C.X.M. spectrum (Spectrum 64X) contains additional lines. A computer fit of this data revealed a doublet with parameters $\delta(Fe) = 0.34$ mms^{-1}, $\Delta = 0.67$ mms^{-1}, characteristic of Fe^{3+} (typical parameters for Fe^{3+}; $\delta(Fe) = 0.1 - 0.7$ mms^{-1}; $\Delta = 0.0 - 1.0$ mms^{-1}). After 7 days exposure, the surface coverage had increased to approximately 30%, this was reflected by the more intense doublet in the C.X.M. spectrum (Spectrum 65X). In an attempt to enhance the doublet contribution to the spectrum, the uncorroded areas of the substrate were masked using a relatively thick plastic layer (Figure 5.6). The resultant rather noisy spectrum (Spectrum 66X) required a collection time of 90 hours.

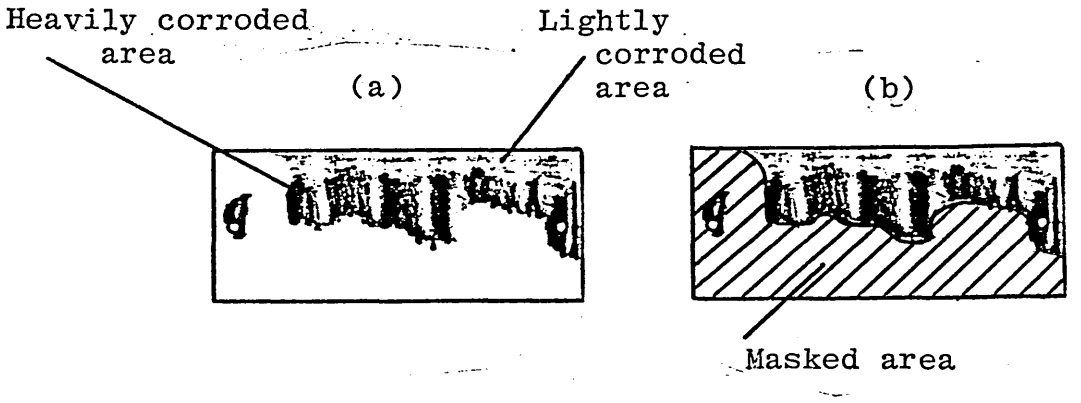

Figure 5.6 : Varnish Coated Mild Steel Samples After Exposure to a Salt Spray for 72 Hours a) unmasked, b) masked with a plastic layer (hatched area). Samples are 4 x actual size

The fitted data revealed identical parameters for spectra 64X, 65X and 66X. The data are summarised in Table 5.6.

Spectrum	Component	δ(Rh)/mms^{-1}	δ(Fe)/mms^{-1}	Δ/mms^{-1}	H_{INT}/kG
64X	Fe	- 0.11	0.00	-	330
	Fe^{3+}	0.23	0.34	0.67	-
65X	Fe	- 0.12	- 0.01	-	329
	Fe^{3+}	0.23	0.34	0.67	-
66X	Fe	- 0.11	0.00	-	331
	Fe^{3+}	0.24	0.35	0.68	-

Table 5.6 : Mössbauer Parameters for an Enriched Annealed Mild Steel Substrate, Subsequently Protected by a Varnish Layer and Exposed to a Standard Salt Spray Test

After 3 hours exposure to a sulphur dioxide atmosphere, a black corrosion product covering approximately 30% of the sample surface area was observed. After 18 hours exposure surface coverage had increased to approximately 70%. The C.X.M. spectrum recorded after 3 hours exposure (Spectrum 67X) revealed four new lines. After 18 hours exposure (Spectrum 68X), the new lines were more pronounced.

The fitted data reveal two doublets with parameters characteristic of Fe^{2+} and Fe^{3+} (typical parameters for Fe^{2+}; $\delta(Fe) = 0.7 - 1.6$ mms^{-1}; $\Delta = 1.5 - 3.7$ mms^{-1}). The data are summarised in Table 5.7.

Spectrum	Component	δ(Rh)mms^{-1}	δ(Fe)/mms^{-1}	Δ/mms^{-1}	H_{INT}/kG
67X	Fe	- 0.12	- 0.01	-	331
	Fe^{3+}	0.10	0.21	0.89	-
	Fe^{2+}	1.14	1.25	1.76	-
68X	Fe	- 0.12	- 0.01	-	331
	Fe^{3+}	0.13	0.24	0.89	-
	Fe^{2+}	1.12	1.23	1.75	-

Table 5.7 : Mössbauer Parameters for an Enriched Annealed Mild Steel Substrate, Subsequently Protected by a Varnish Layer and Exposed to a Sulphur Dioxide Atmosphere

In conclusion, although the enriched annealed samples enable spectra to be recorded when a protective layer has been applied to the surface, only the presence of Fe^{2+} and Fe^{3+} ions can be deduced from the data so far obtained. To uniquely identify the corrosion products as for example, iron oxides, hydroxides, oxyhydroxides, chlorides, oxychlorides or sulphur containing species, more work is required. Indeed a variable temperature backscatter technique capable of detecting the conversion X-ray may have to be developed.

Although poor quality spectra were sometimes obtained, and care must be taken regarding the thickness and composition of protective layers, it should be possible to improve the situation in many ways using, for example, (i) larger samples, (ii) stronger Mössbauer sources, (iii) longer collection times, (iv) the use of overlayers to reduce the contribution to the spectrum of the bulk sample, (v) γ scattering through thicker layers and in situations were potential X-ray filters are necessarily employed, (vi) computer models to subtract the substrate contribution to the spectrum - indeed this last suggestion may enable natural samples, ie not enriched in the isotope ^{57}Fe to be used. The Mössbauer spectra are given in Section 5.6.

5.5 Surface Monitoring of some Mild Steel Substrates

Three mild steel substrates have been investigated. Sample 1 was an ordinary mild steel which had received no further treatment; sample 2 was an ordinary mild steel with a 20 nm vacuum evaporated surface layer of ^{57}Fe (Section 5.2); sample 3 was as sample 2 and subsequently annealed (Section 5.3.3).

The surface of the samples were monitored using the C.E.M. and C.X.M. techniques. The signal to background ratio, S/B, determined as:

$$\frac{\text{No. of counts at peak 1}}{\text{Average no. of counts at baseline}}$$

demonstrates the effect of the surface treatment. The deposition of a 20 nm layer of ^{57}Fe increased the S/B ratio in both the electron and X-ray spectra. Subsequent annealing had the effect of reducing the S/B ratio in the electron spectrum and further increasing its value in the X-ray spectrum. Remembering the escape depths of each type of radiation, this is entirely consistent with the diffusion of a pure ^{57}Fe surface film of 20 nm to produce a near surface region rich in ^{57}Fe to a depth of approximately 90 nm (Figure 5.3). The data are summarised in Table 5.8

Spectrum \ Sample	1	2	3
Electron	1.073	1.590	1.419
X-ray	1.021	1.073	1.078

Table 5.8 : Signal to Background Ratio for Three Mild Steel Substrates Detecting Either the Conversion Electron or the Conversion X-Ray

The surface of similar samples were monitored using the secondary ion mass spectrometer (SIMS) facility of a VG 500 Microlab (SIMS spectra 1-3). The SIMS technique [9] uses a beam of low energy argon ions to bombard the sample surface. Surface atoms are sputtered from the sample, some of these sputtered particles being in an ionised state. A quadrupole mass spectrometer is used to analyse these sputtered ions as a function of their mass/charge ratio.

The SIMS spectrum of sample 1 revealed a large ^{56}Fe peak plus a small ^{57}Fe peak reflecting the natural isotopic abundance of these species (SIMS spectrum 1). The SIMS spectrum of sample 2 is dominated by a ^{57}Fe peak due to the vacuum evaporated layer of ^{57}Fe onto the surface of the substrate (SIMS spectrum 2). After annealing to produce sample 3, the SIMS spectrum was similar to the

spectrum of the untreated mild steel substrate but shows an increased contribution from ^{57}Fe as would be expected for such a sample (SIMS spectrum 3). The peak at mass/charge ratio = 55 in this spectrum is due to elemental manganese, small occlusions were observed in a similar sample using a Philips 500 scanning electron microscope (Figure 5.7).

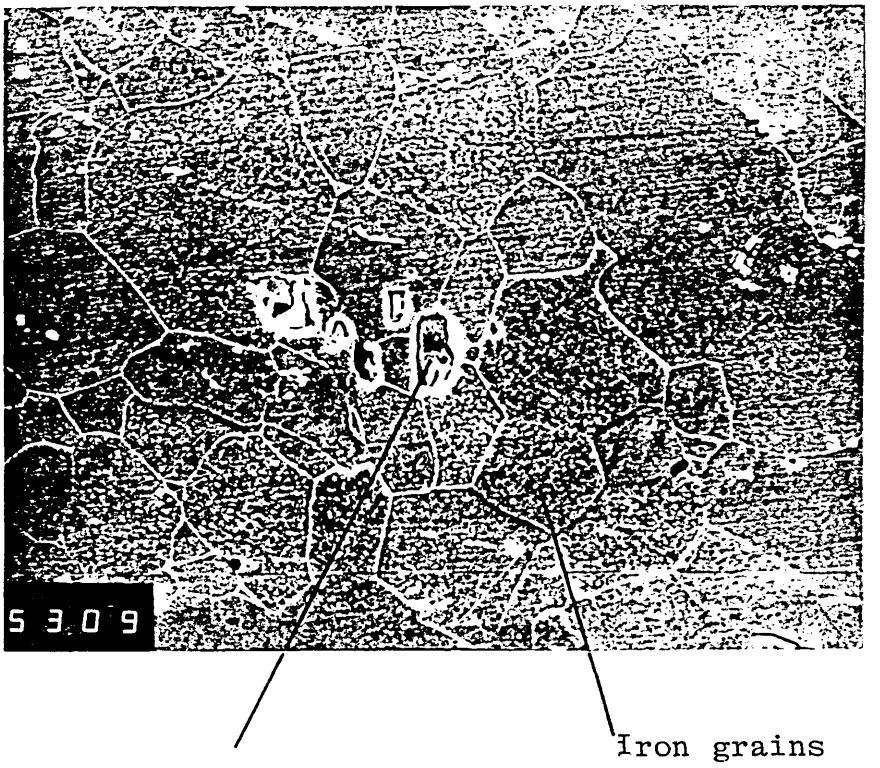

Figure 5.7 : Philips 500 Scanning Electron Microscope Photograph of Mild Steel Surface (x 800 Magnification)

The energy dispersive analysis of X-rays (EDAX) detection system of the same microscope was used to identify the occlusions as manganese (Figure 5.8). Manganese is often added to steels to combine with sulphur and thereby remove the detrimental effects on some properties which elemental sulphur imparts on certain steels. No sulphur was observed in this sample and it is therefore suggested that manganese is present as an impurity - possibly as a remnant in the furnace, for example, from a previous production run.

BULK ANALYSIS

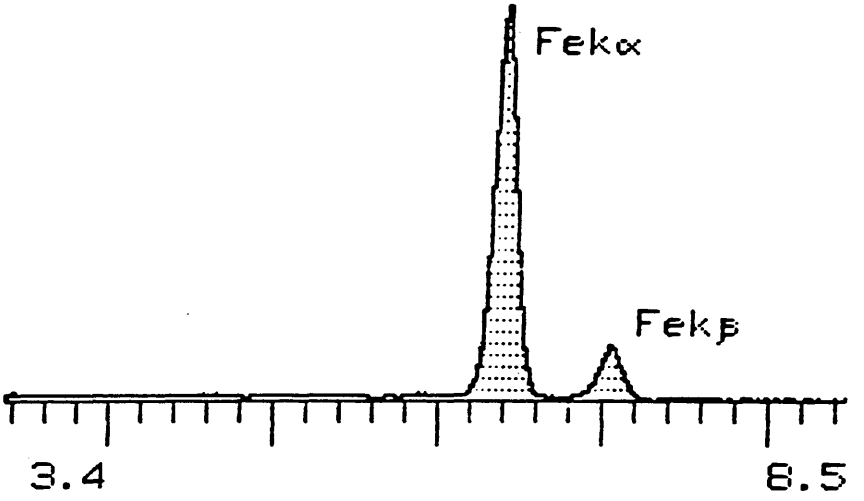

SPOT ANALYSIS
Mn PRECIPITATE

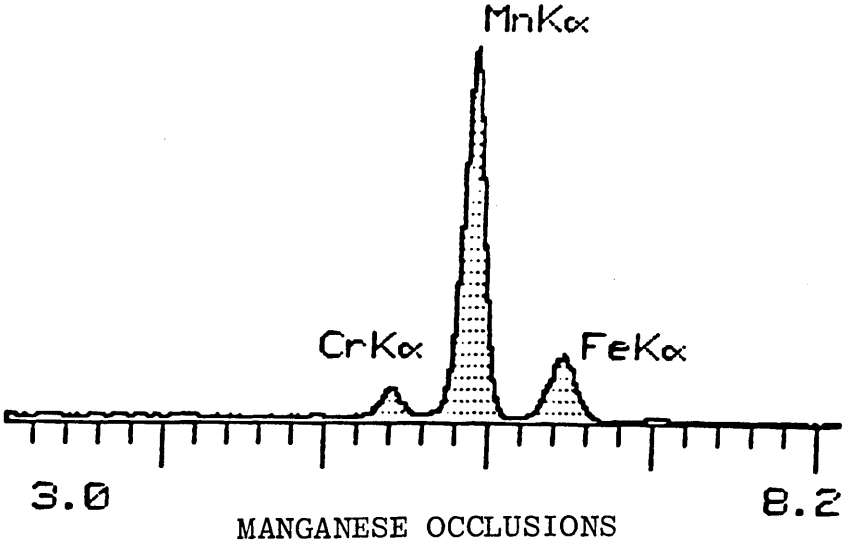

Figure 5.8 : X-ray Energy Spectrum Obtained by the EDAX System of Bulk Iron and Small Manganese Occlusions in a Mild Steel Sample

SIMS SPECTRUM 1 : SAMPLE 1 VG SCIENTIFIC

Positive SIMS. Target Bias 53.0 V Max Count Rate = 39935
Step Size = 0.025 AMU Time = 52.00 secs x 3 Scans

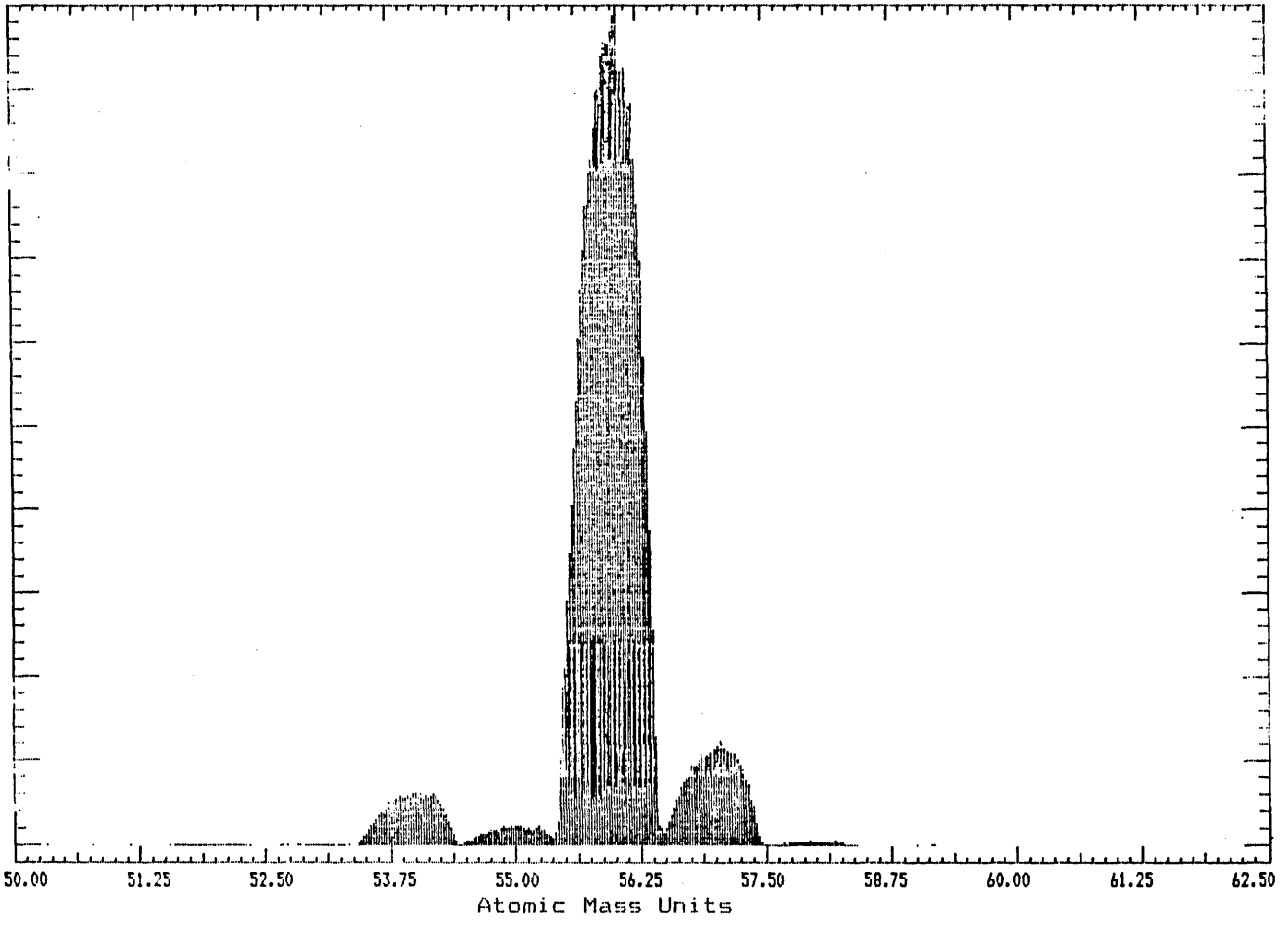

SIMS SPECTRUM 2 : SAMPLE 2

VG SCIENTIFIC

Positive SIMS. Target Bias 56.0 V Max Count Rate = 109220
Step Size = 0.025 AMU Time = 20.00 secs x 3 Scans

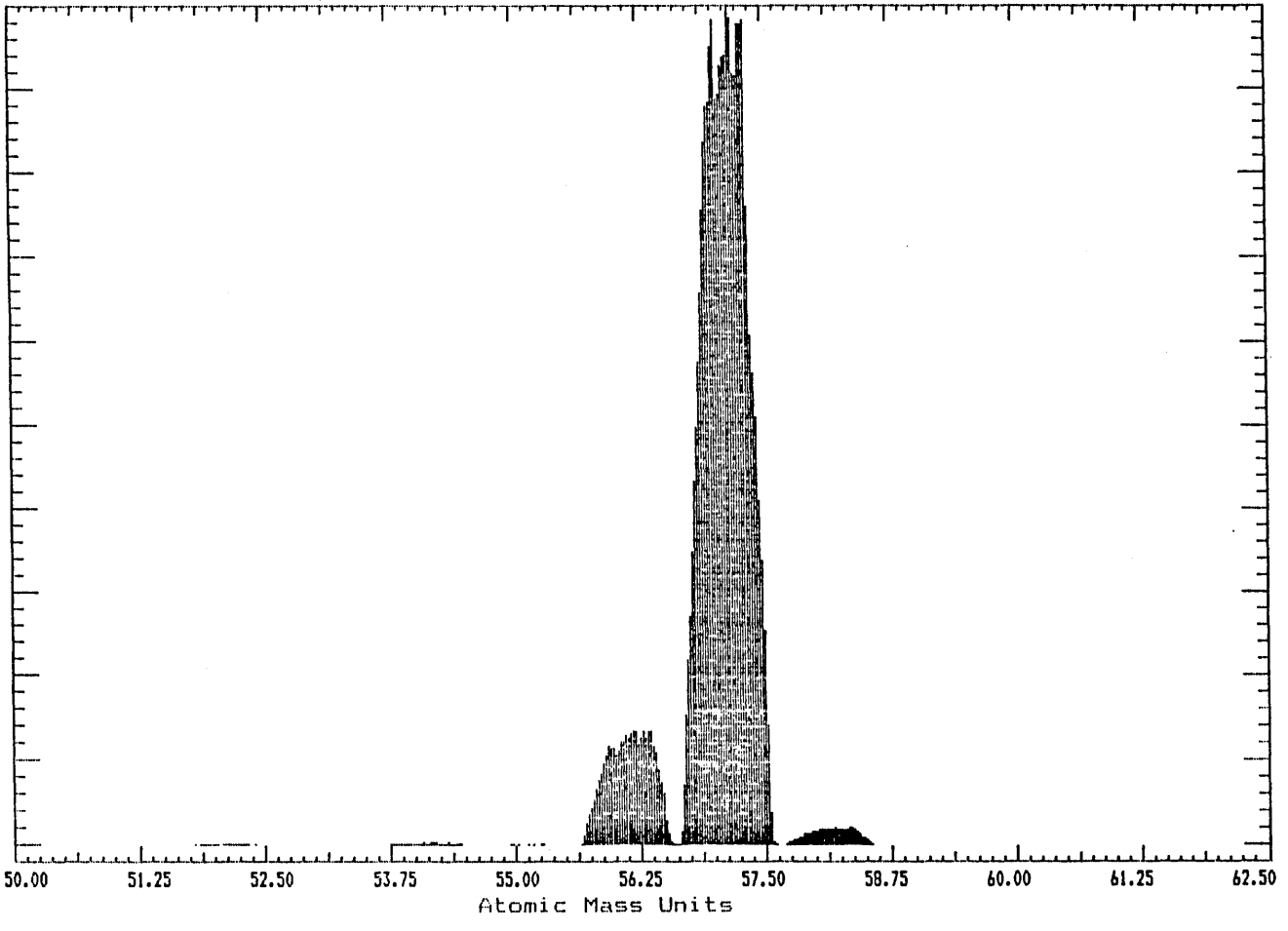

SIMS SPECTRUM 3 : SAMPLE 3

VG SCIENTIFIC

Positive SIMS. Target Bias 53.0 V Max Count Rate = 37912
Step Size = 0.025 AMU Time = 52.00 secs x 3 Scans

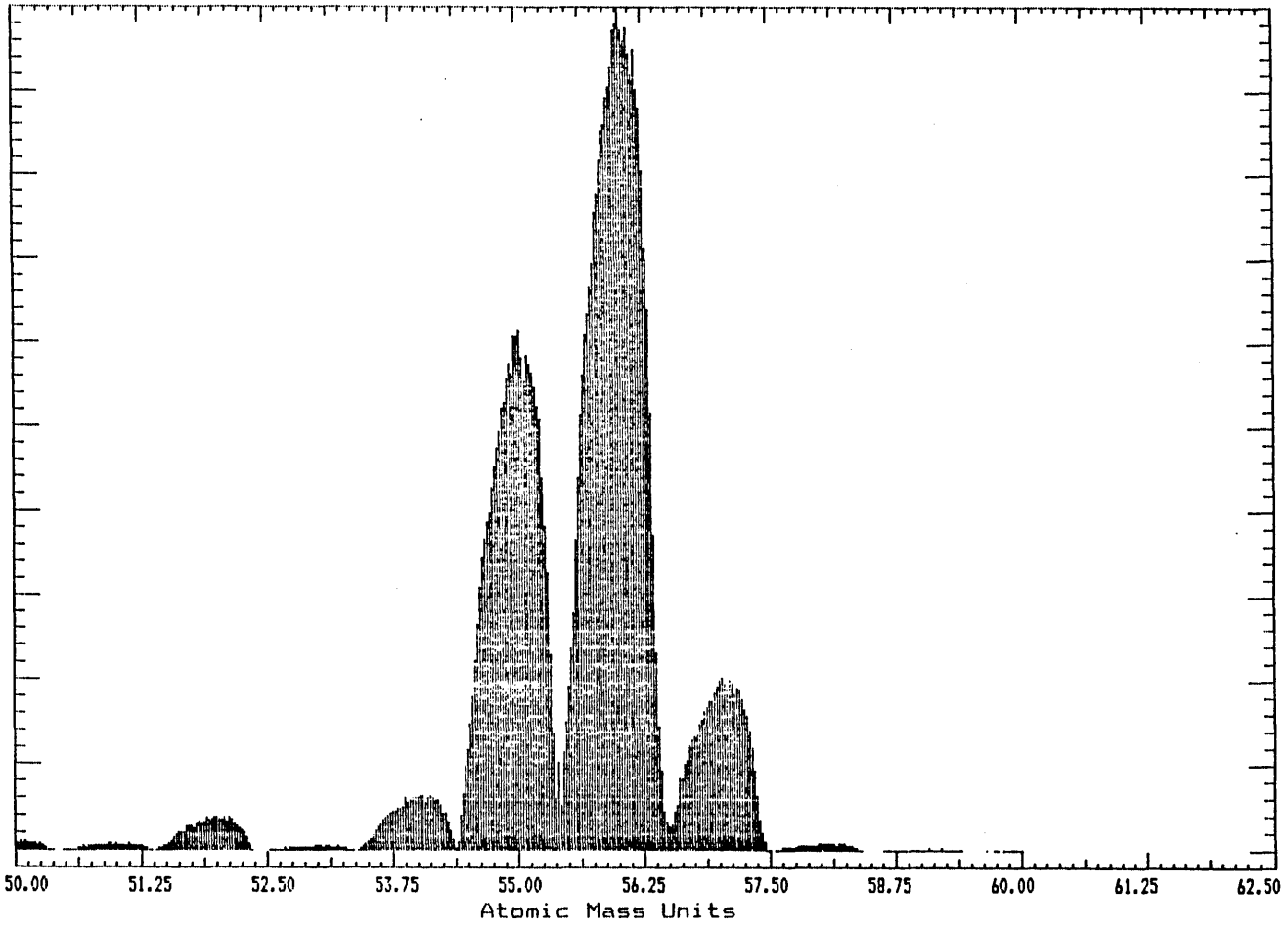

FAILED SAMPLE ANNEALED 900K, 100 MINS

ARGON TUBE FURNACE

SPECTRUM 54E

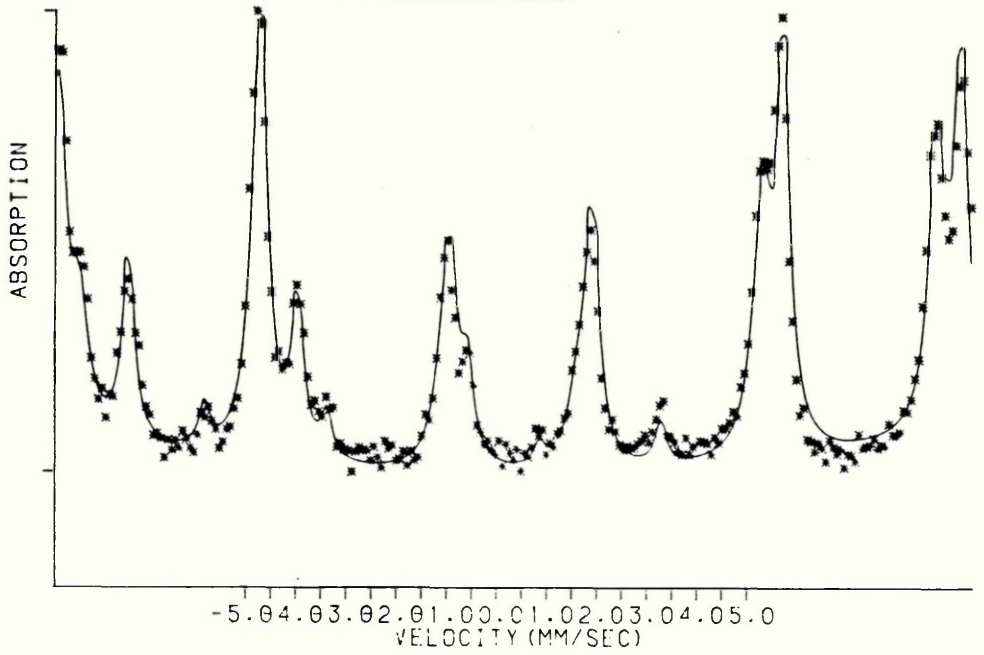

SPECTRUM 55X

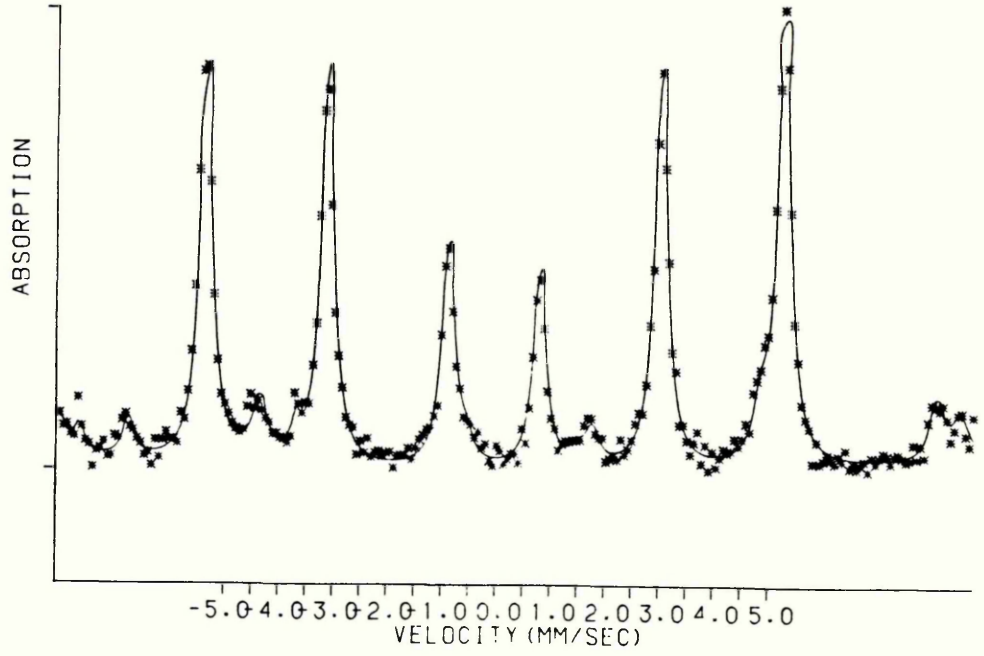

FAILED SAMPLE ANNEALED 900K, 100 MINS

SILICA GLASS PHIAL UNDER VACUUM

SPECTRUM 56E

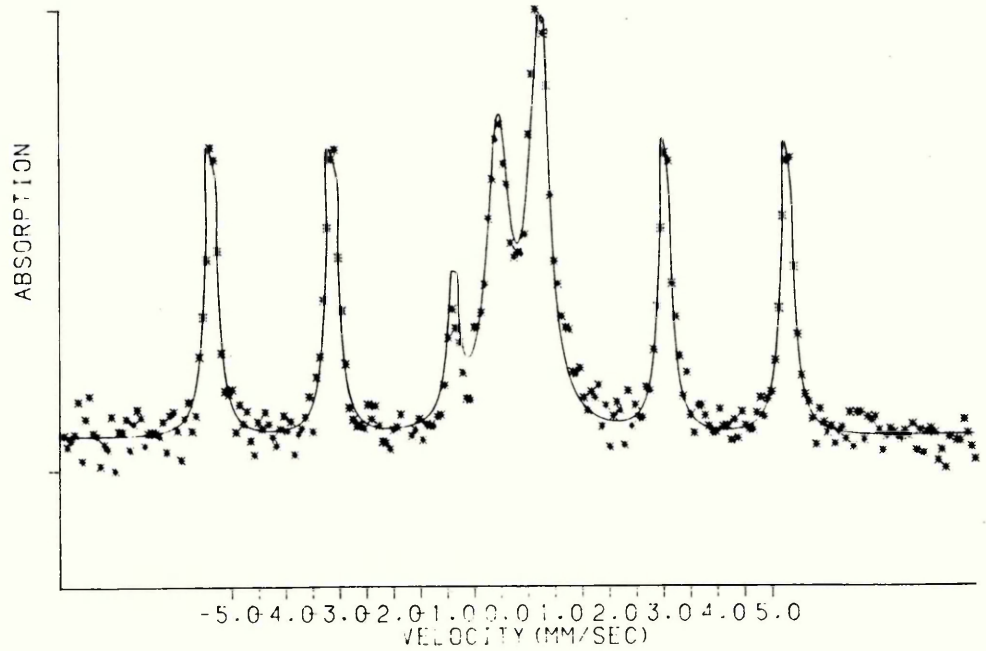

SPECTRUM 57X

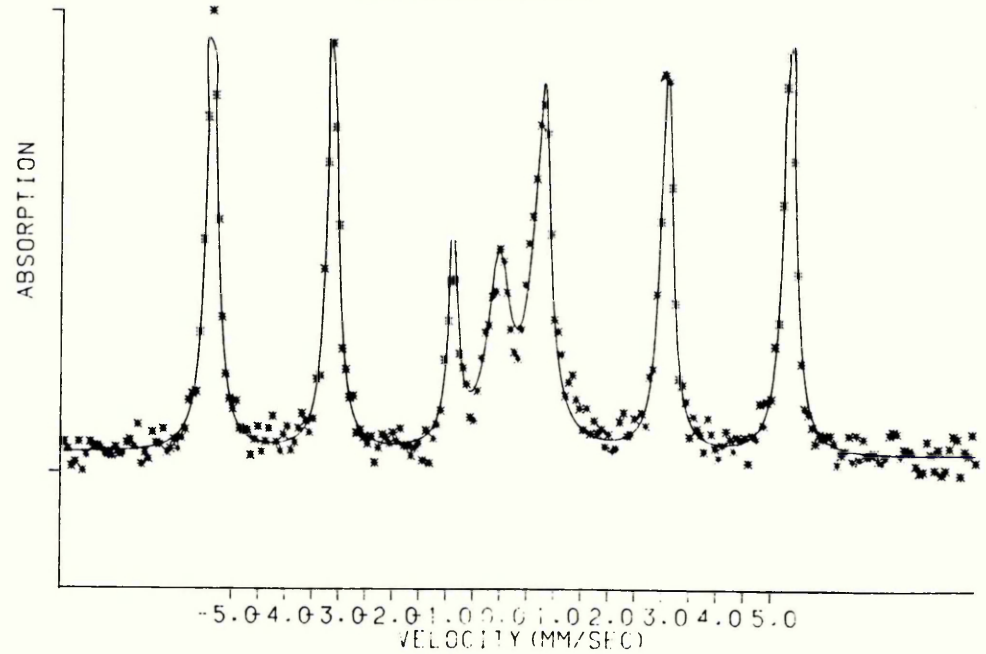

FAILED SAMPLE ANNEALED 900K, 100 MINS

SILICA GLASS PHIAL UNDER ARGON

SPECTRUM 58E

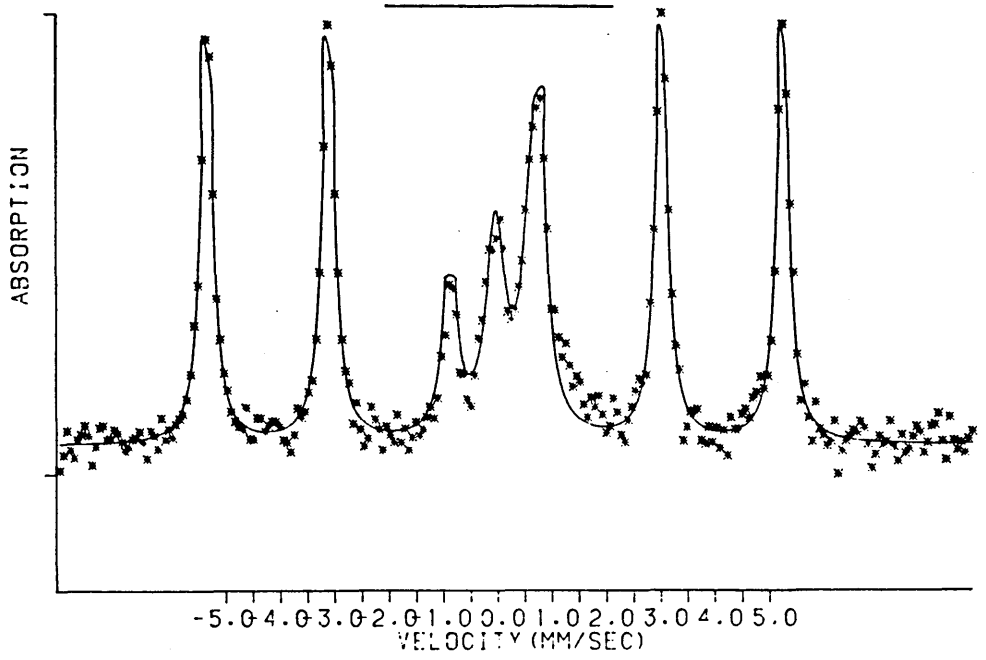

SPECTRUM 59X

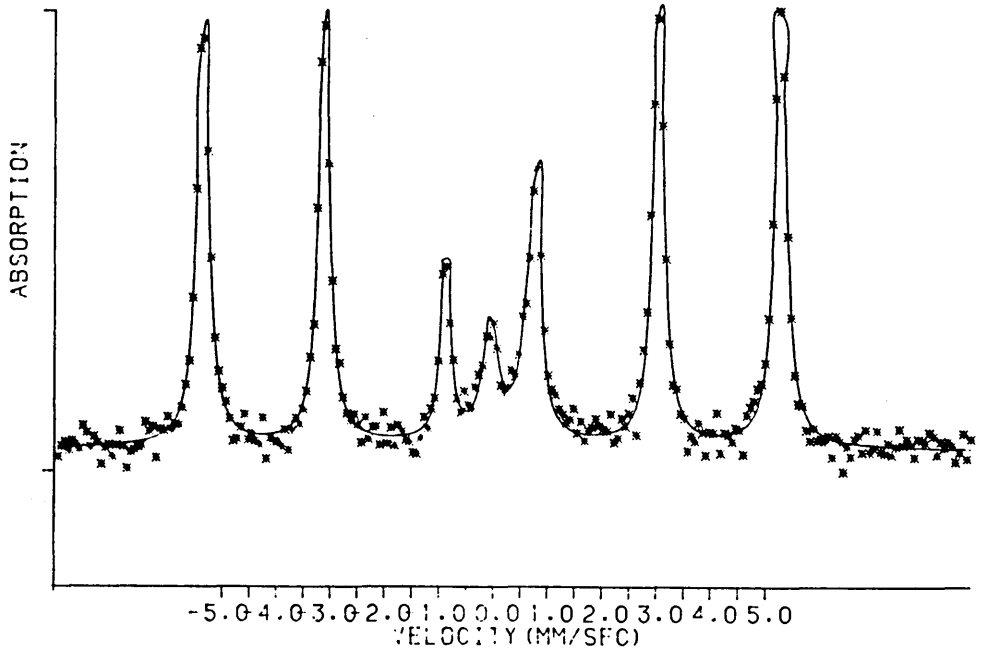

SUCCESSFULLY ANNEALED SAMPLE 900K, 100 MINS

SILICA GLASS PHIAL UNDER ARGON WITH TUNGSTEN SCAVENGER

SPECTRUM 60E

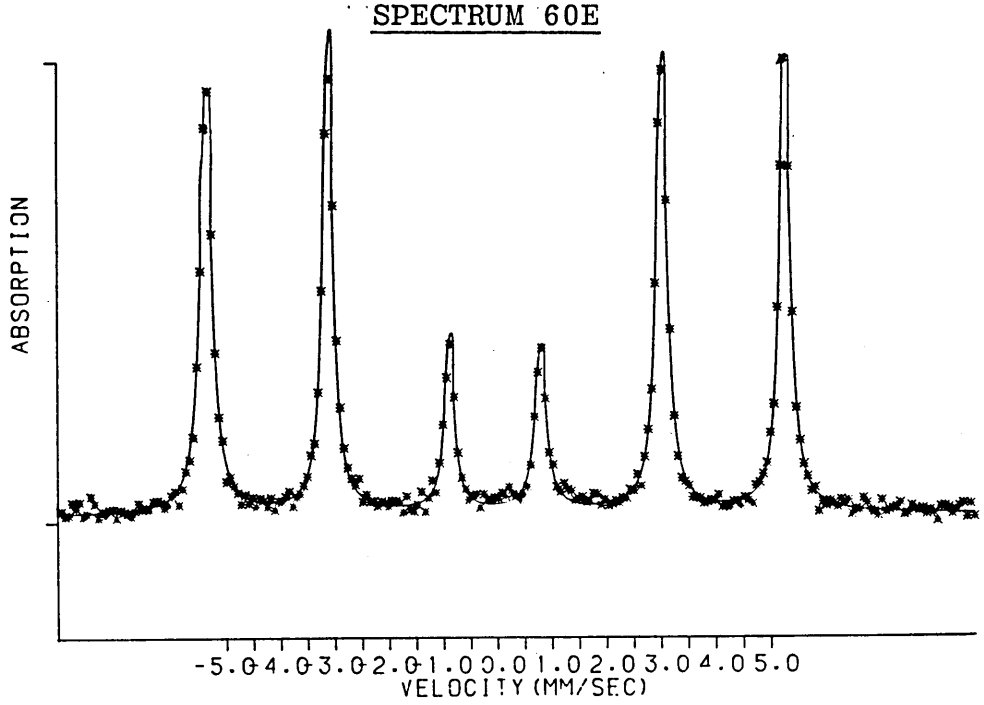

SPECTRUM 61X

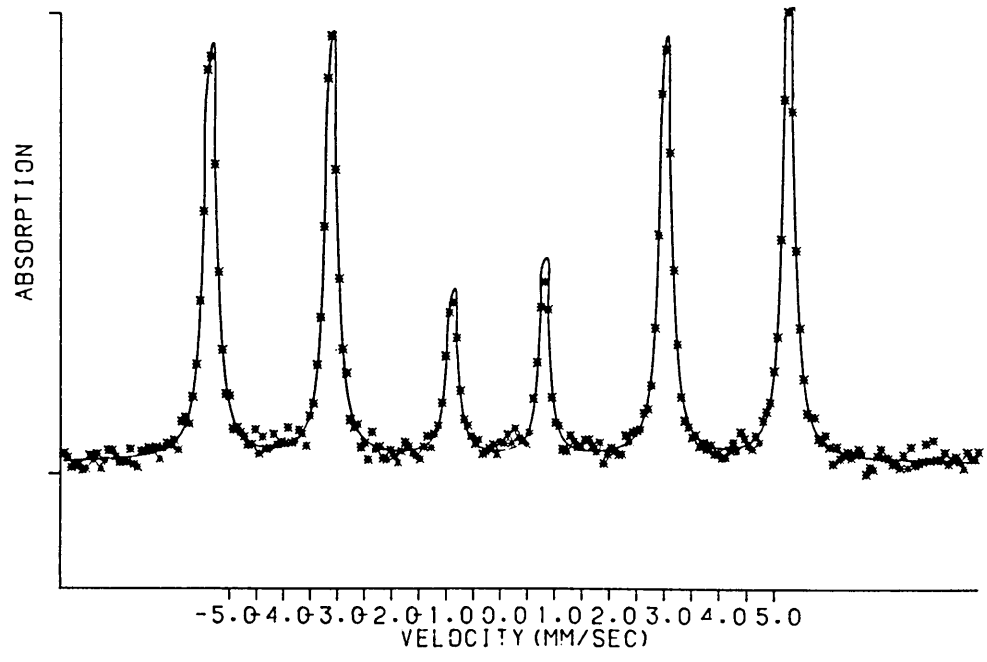

SUCCESSFULLY ANNEALED SAMPLE

APPLIED PAINT LAYER

SPECTRUM 62X

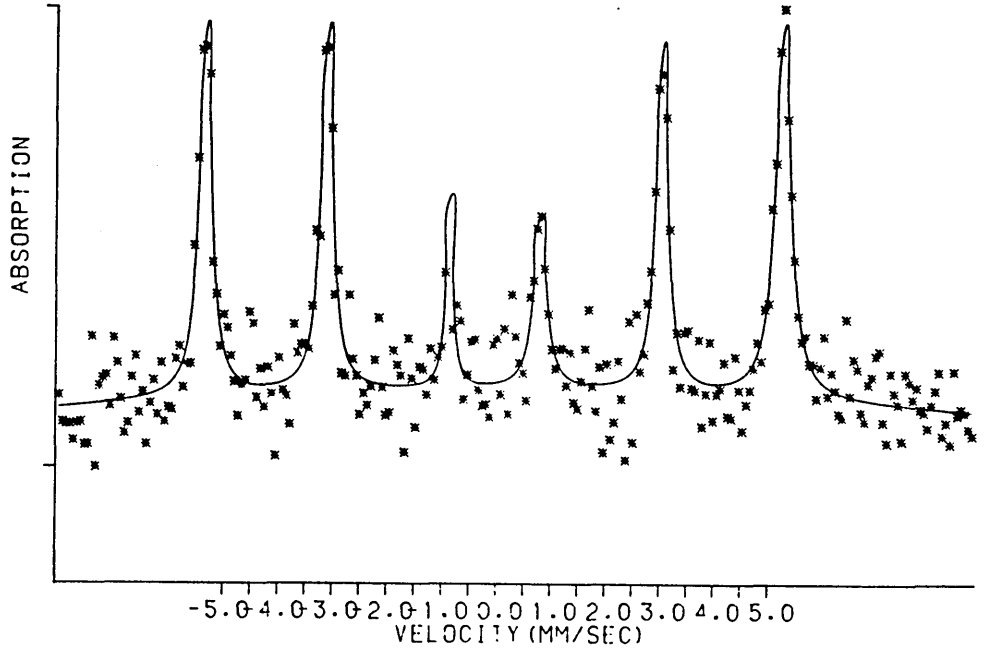

APPLIED VARNISH LAYER

SPECTRUM 63X

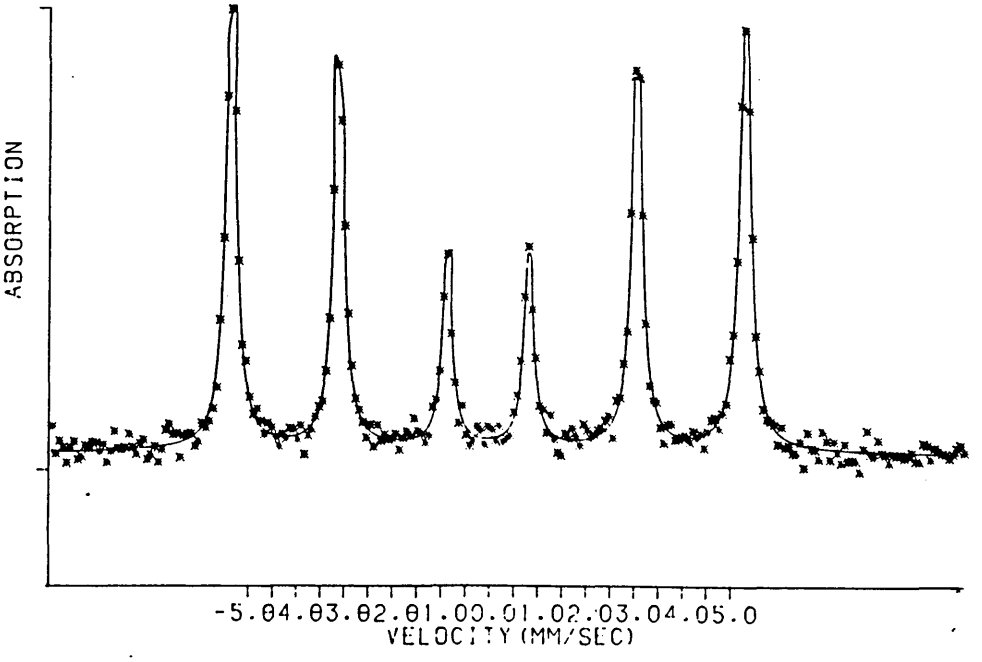

APPLIED VARNISH LAYER

72 HOUR EXPOSURE TO SALT SPRAY

SPECTRUM 64X

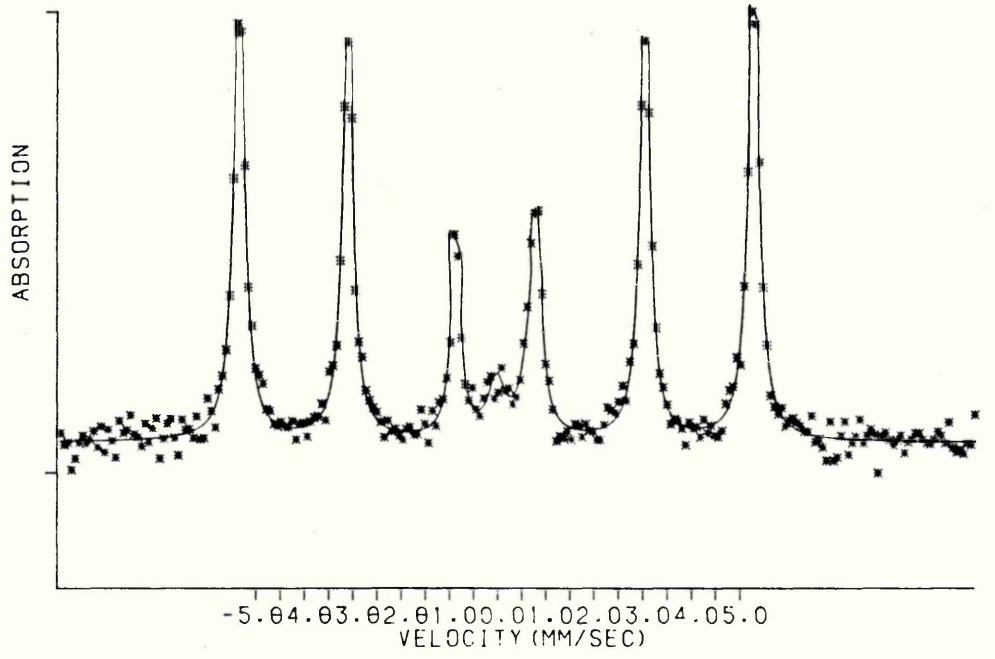

7 DAY EXPOSURE TO SALT SPRAY

SPECTRUM 65X

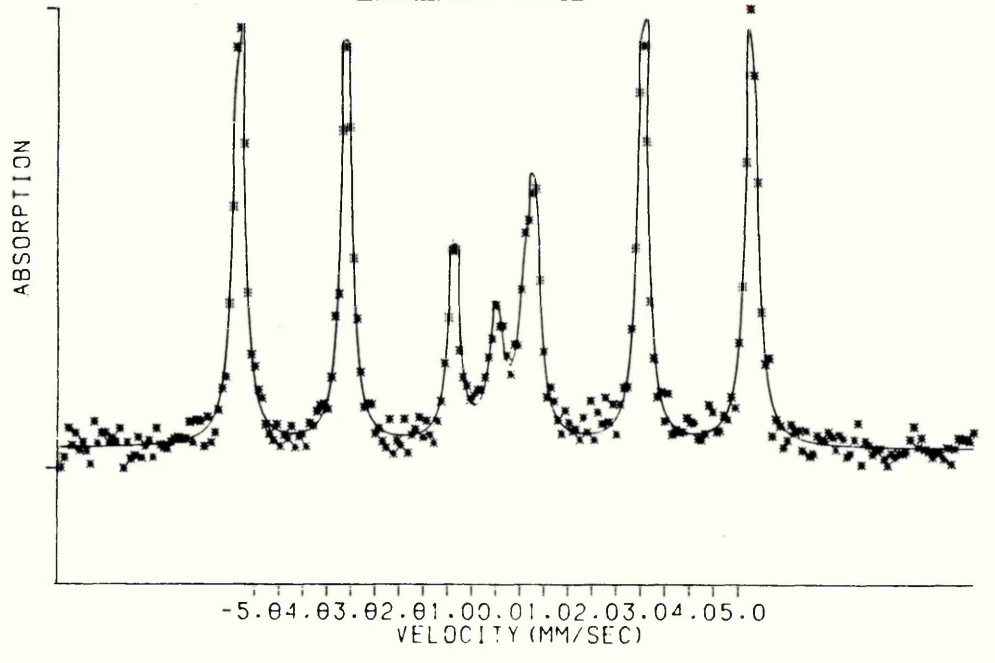

7 DAY EXPOSURE TO SALT SPRAY, MASKED SUBSTRATE

SPECTRUM 66X

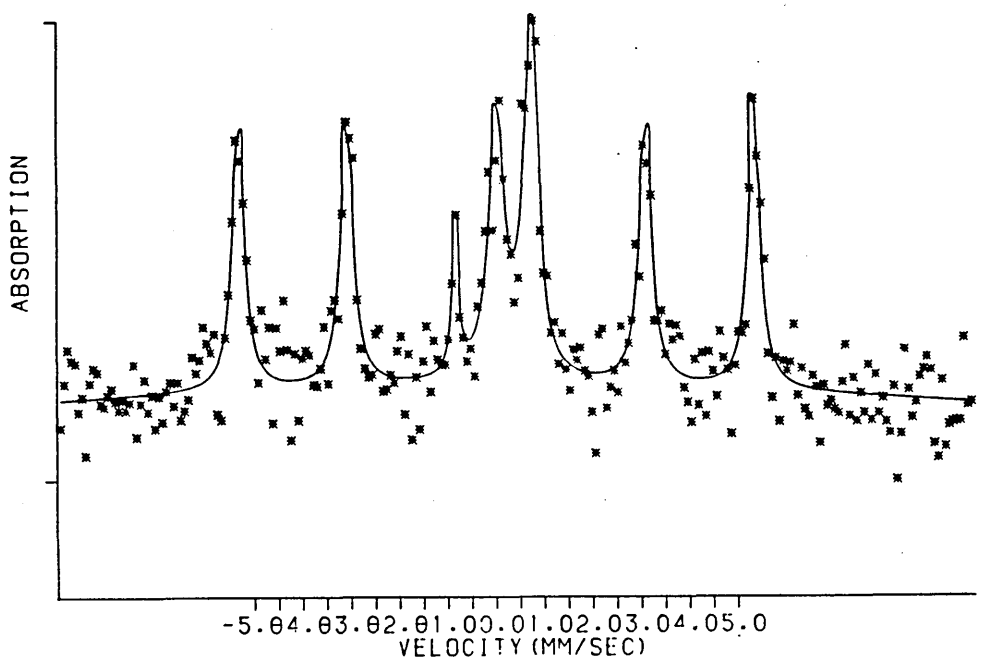

3 HOUR EXPOSURE TO SO_2 ATMOSPHERE

SPECTRUM 67X

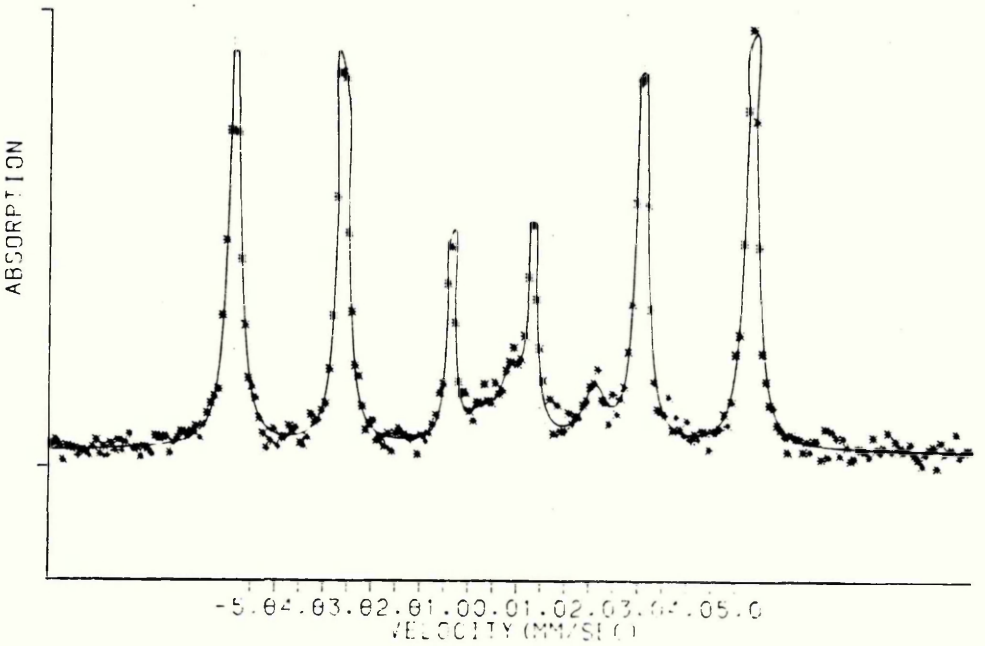

18 HOUR EXPOSURE TO SO_2 ATMOSPHERE

SPECTRUM 68X

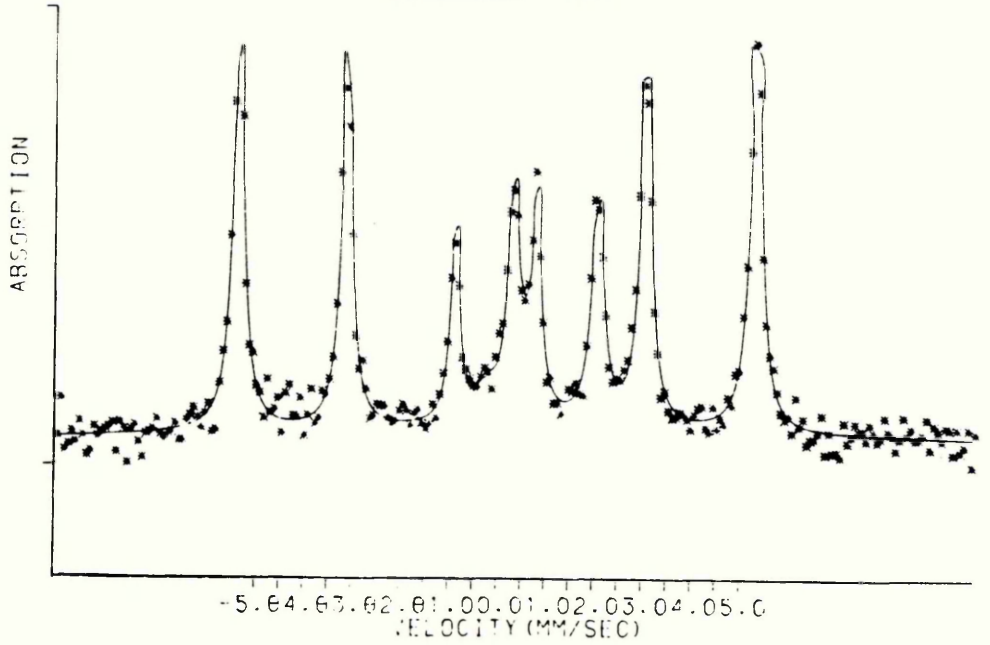

REFERENCES

1. K. R. Swanson, J. J. Spijkermann, J. Appl. Phys., 41, No. 7, p. 3155, 1970.

2. Practical Methods in Electron Microscopy, Vol 1, edited by A. M. Glauert, Part 1, Specimen Preparation in Materials Science by P. J. Goodhew, 1972.

3. Mr. L Bint, U.K.A.E.A. Harwell, England. Private Communication, September 1984.

4. D. M. Allen-Booth, J. S. Brooks, Department of Applied Physics, Sheffield City Polytechnic, Sheffield, England. Private Communication, March 1985.

5. Smithells Metal Reference Book, 6th Edition, edited by E. A. Brandes, Section 13, Diffusion in Metals, p. 1-14.

6. H. Oikawa, Lattice Self Diffusion in Solid Iron: A Critical Review, Technology Reports, Tohoku Univ, 47, 1, p. 67, 1982.

7. Instrument Handbook Part 50, Rank Taylor-Hobson Talysurf 5 System, Rank Taylor-Hobson, PO Box 36, New Star Road, Leicester LE4 7JQ.

8. BS3900 British Standard Methods of Test for Paints Part F4. Resistance to Continuous Salt Spray 1968.

9. E. Zinner, Scanning 3, p. 57, 1980.

CHAPTER 6 : CONCLUSIONS AND SUGGESTIONS FOR FUTURE WORK

6.1 Conclusions

6.2 Future Work

6.1 Conclusions

The aims of this project have been to investigate the use of ^{57}Fe Mössbauer spectroscopy to observe and characterise corrosion in iron systems. To achieve these aims, a preliminary study of two standard iron oxides was undertaken. Real environmental corrosion products were then investigated and an unambiguous interpretation necessitated the use of a variable temperature facility.

A variable temperature transmission Mössbauer spectroscopy facility has been successfully developed and the problem of vibration at the sample low temperature stage has been overcome. The facility enabled characteristic spectra to be recorded over a wide temperature range from room temperature down to a base temperature of approximately 10 Kelvin with temperature control of ± 0.5 Kelvin without the requirements of a liquid helium facility.

The differences in observed spectra between a sample which exhibits only bulk properties and one in which the particle size distribution within the sample is such that relaxation phenomena becomes important have been clearly demonstrated.

In this way, variable temperature data yields a great deal of information on the nature of iron components

within a sample, and low temperature measurements allow the utilization of the full potential of the Mössbauer technique. The non-destructive nature of the method enables the use of complementary techniques to confirm any interpretation made from the Mössbauer data.

If information about surface properties of solids is sought, then backscattering techniques based on the detection of conversion electrons (CEMS) or conversion x-rays (CXMS) emitted from the surface following the resonant absorption of a γ-ray are required. Conversion electrons are attenuated very rapidly and therefore CEM spectra will be of most value in the study of thin surface layers such as those produced in the early stages of oxidation or corrosion, the greater escape depth of the conversion x-ray allows deeper layers to be probed, complementary use of the two methods is of course possible. Both CEMS and CXMS techniques have been successfully developed and are now routinely available in our laboratory.

It has also been demonstrated that the greater penetration of the conversion x-ray can be utilized in recording the Mössbauer spectra of samples to which a protective coating, such as a varnish or paint layer, has been applied. The CXM spectra are recorded without the need to remove such an applied layer, thus eliminating the possibility of any chemical changes or the loss of

corrosion products occurring as a result of the removal of such a layer.

However, if only room temperature spectra are recorded, then difficulties are encountered in the assignment of spectra that contain only quadrupole doublets. Only the presence of ferrous and/or ferric ions can be deduced. To uniquely identify the corrosion products as for example iron oxides, hydroxides, oxyhydroxides, chlorides, oxychlorides or sulphur containing species, a great deal more work is required. Indeed, a variable temperature backscatter technique capable of detecting the conversion x-ray would have to be developed.

6.2 Future Work

Other areas of future work might include a great deal of routine work on phase analysis and phase transformations. The investigation of corrosion products formed in different aggressive media, with particular reference to the influence of particle size distributions within the sample on the observed spectra. The combination of the backscatter Mössbauer techniques with other surface techniques for example x-ray photoelectron spectroscopy, Auger electron spectroscopy, secondary ion mass spectrometry.

Development of computer techniques to allow the deconvolution of the complex spectra sometimes obtained from mixtures or iron corrosion products will continue;

similar techniques could also be used to enable the subtraction of any substrate contribution to a back-scatter spectrum. This will effectively make the technique more surface sensitive and may allow the use of natural substrates, ie substrates not surface enriched in the Mössbauer isotope ^{57}Fe, longer collection times may, however, be necessary before a useful effect is observed.

ACKNOWLEDGEMENTS

The author extends his sincere gratitude to Supervisors Dr J S Brooks, Dr D W Allen and Dr E Jackson for their guidance, encouragement and optimism during the work compiled in this thesis.

The author would also like to thank the Material Quality Assurance Directorate for the funding of this project and in particular Dr W Trott of the said establishment for useful discussions and the supply of materials.

Finally, the author wishes to express his sincere thanks to all the staff in the Faculty of Technology who have shown an interest and given help during the period of this research, in particular technicians Mr R Smith and Mrs G Sidda and typist Miss A Hughes.

COURSES AND CONFERENCES ATTENDED

1. Introduction to Mössbauer Spectroscopy, 10 x 2 hour lectures, Sheffield City Polytechnic, October 1982.

2. Basic Computing, 8 x 2 hour lectures, Sheffield City Polytechnic, October 1982.

3. Royal Society of Chemistry (Birmingham and West Midlands Section) Third Dalton Meeting. A Symposium on the Applications of Mössbauer Spectroscopy. University of Birmingham, 29 March 1983.

4. Royal Society of Chemistry Mössbauer Discussion Group Meetings:

   (i) University of Manchester Institute of Science and Technology, 11-13 July 1983.

   (ii) Wadham College, University of Oxford, 2-4 July 1984.

   (iii) University of East Anglia, 8-10 July 1985.

5. Modern Methods of Surface Analysis, Loughborough University of Technology, 8 February 1984.